# Measurements of the exclusive production of a real photon with the ZEUS detector at HERA II

Dissertation

zur Erlangung des Doktorgrades

des Fachbereichs Physik

der Universität Hamburg

vorgelegt von

Raquel Santamarta Martínez

aus León (España)

Hamburg

2007

"Todo arde si le aplicas
la chispa adecuada. . ."
*Enrique Bumbury*

# Abstract

The study of exclusive processes is one of the most promising tools to obtain information on the nucleon via generalized parton distributions. The simplest of these reactions is the Deeply Virtual Compton Scattering process in which a real photon is produced via diffractive exchange. Using the interference term between Deeply Virtual Compton Scattering and the Bethe-Heitler processes it is possible to extract the generalized parton distributions.

The measurement presented in this thesis is a study of Deeply Virtual Compton Scattering and Bethe-Heitler processes recorder with the ZEUS detector. The data analyzed were taken with HERA II in the years 2003 to 2005, corresponding to an integrated luminosity of 41 pb$^{-1}$ for $e^+p$ and 136 pb$^{-1}$ for $e^-p$ scattering data.

The cross section of the elastic Bethe-Heitler process measured in the kinematic region $230 < W < 310$ GeV, $20 < Q^2 < 1000$ GeV$^2$ and $|t| < 1$ GeV$^2$ is presented. The feasibility of measurement of the Deeply Virtual Compton Scattering process is also reported.

# Kurzfassung

Die Untersuchung exklusiver Prozesse ist eine der vielversprechensten Methoden um Informationen über das Nukleon in Form von generalisierte Partonen Verteilungen zu erhalten. Die einfachste dieser Reaktionen ist die tief virtuelle Compton Streuung (Deeply Virtual Compton Scattering), in welcher ein reales Photon durch diffraktiven Austausch erzeugt wird. Durch die Interferenz zwischen der tief virtuellen Compton Streuung und dem Bethe-Heitler Prozess ist es möglich, generalisierte Partonen Verteilungen zu bestimmen.

Die, in dieser Arbeit vorgestellte, Analyse behandelt eine Messung tief virtueller Compton Streuung und Bethe-Heitler Prozesse mit dem ZEUS Detector unter Verwendung von HERA II Daten. Die Daten wurden in den Jahren 2003-2005 genommen und entsprechen einer integrierten Luminosität von 41 pb$^{-1}$ ($e^+p$ ) und 136 pb$^{-1}$ ($e^-p$ ).

Es wird die Messung des Wirkungsquerschnittes des elastischen Bethe-Heitler Prozesses präsentiert. Der gemessene Wirkungsquerschnitt bezieht sich auf den kinematischen Bereich von $230 < W < 310$ GeV, $20 < Q^2 < 1000$ GeV$^2$ und $|t| < 1$ GeV$^2$. Auserdem wird die Machbarkeit der Messung des DVCS Prozesses gezeigt.

# Contents

# Introduction

The HERA collider has been used since 1992 as an important laboratory to probe the structure of the proton. The fundamental particles that form the internal structure of protons are known to be quarks and gluons and the interactions between them are described by the theory of Quantum Chromodynamics (QCD).

In the last decades, the exploration of deep inelastic scattering at HERA has delivered a rich variety of measurements which has lead to a much deeper understanding of QCD and on the structure of the proton in terms of the parton density functions. However a complete picture of the proton is not yet achieved, i.e, the parton density functions do not contain information about the transverse distribution of the constituents of the proton.

The HERA II running period with the high luminosities that are currently being reached, the available polarization for the lepton beams and the new instrumentation installed in the experiments, has opened an exciting time for new phenomena and new and more precise measurements.

Exclusive processes, in which real photons, mesons or lepton pairs are produced, can be described in terms of generalized partons distributions. These phenomenological functions encode information which, among other things, could deliver the three-dimensional picture of the proton.

The most simple of these reactions is the diffractive production of a real photon, also known as Deeply Virtual Compton Scattering (DVCS). In this process a virtual photon is scattered off a proton via diffractive exchange, $\gamma^\star p \to \gamma p'$. In deep inelastic scattering, DVCS is studied by means of the reaction

$$e \; p \; \to \; e' \; \gamma \; p'$$

which delivers an experimental signature given by the scattered electron and proton and the real photon. The other important contribution with the same final state is the Bethe-Heitler (BH) process in which the real photon is emitted from the lepton line. The interference between DVCS and BH, which can in

principle be obtained by asymmetry measurements, will provide direct access to the generalized parton distributions. Beam-spin and beam-charge asymmetry measurements [3, 4] have been reported to be sensitive to discriminate between different parametrization of the generalized parton distributions.

The previous measurements of the DVCS cross sections [1, 2] have shown the characteristic features expected for the hard processes and, in general, a good agreement with the predictions of QCD models.

This thesis presents measurements of the Deeply Virtual Compton Scattering performed with the ZEUS detector using data collected during the HERA II running period. The data analyzed correspond to the $e^+p$ (41 pb$^{-1}$) and $e^-p$ (136 pb$^{-1}$) collisions taken during 2003-04 and 2004-05, respectively. The aim of this work is to study the feasibility of the measurements of DVCS at HERA II which will allow, in future, to increase the precision of the current results and also, due to the availability of polarized beams, to extract asymmetries. The thesis also reports measurements of the elastic Bethe-Heitler cross sections based on the $e^-p$ data sample.

The thesis is organized as follows: chapter 1 gives an overview of the theoretical framework for the analysis, reporting also previous measurements on DVCS. Chapter 2 reviews the ZEUS detector at HERA. In chapter 3 the bases of simulation in high-energy physics are introduced followed by a description of the specific programs used in the analysis. Chapter 4 is dedicated to the different steps for the reconstruction procedure which delivers the main quantities used for the selection of events. In chapter 5 the analysis strategy to obtain the signal and control samples is described. Moreover a detailed description of the event selection is given. Chapter 6 is dedicated to the analysis of DVCS events. Chapter 7 presents the studies concerning the Bethe-Heitler sample used for the cross section measurements. The extraction of cross sections and the determination of the corresponding uncertanties are explained in chapter 8. Finally the summary and conclusions.

# Theoretical overview

## 1.1 The Standard Model

The Standard Model (SM) [5] is the theoretical framework which describes the elementary particles and how they interact. It was introduced in the 1970's and since then it has successfully passed very precise tests.

In the SM, the elementary particles are divided in two classes: fermions with spin=$\frac{1}{2}$ and bosons. Fermions are the constituents of matter. They are classified as leptons and quarks (six of each and their corresponding partners, the antiparticles [1]) and grouped in three generations as listed in table 1.1. The bosons are the intermediate interaction particles. The four forces that govern our world are known to be mediated by the exchange of bosons. The different exchanged bosons and interaction are summarized in table 1.2. At the moment, for the gravitational force, there is not a satisfactory theory describing the interaction via boson exchange.

|  | Generations | | | Electric charge | Interactions |
|---|---|---|---|---|---|
| **Quarks** | $u$ | $c$ | $t$ | $+2/3$ | electromagnetic, weak, strong |
|  | $d$ | $s$ | $b$ | $-1/3$ | electromagnetic, weak, strong |
| **Leptons** | $\nu_e$ | $\nu_\mu$ | $\nu_\tau$ | $0$ | weak |
|  | $e$ | $\mu$ | $\tau$ | $-1$ | electromagnetic, weak |

**Table 1.1:** Generations of quarks and leptons and how they interact. The electric charge is given in units of the elementary charge $e$.

The Standard Model is built as a quantum field theory based on the gauge symmetry group $SU(3)_C \times SU(2)_L \times U(1)_Y$. The strong interaction is described by the Quantum Chromodynamics which is based on the non-abelian gauge symmetry group $SU(3)_C$. The 8 gluons are the gauge bosons associated with this

---

[1]Antiparticles have opposite charge w.r.t. their partners.

| Boson | Mass(GeV) | Interactions |
|:---:|:---:|:---:|
| photon($\gamma$) | 0 | electromagnetic |
| $W^{\pm}$ | 80 | weak |
| $Z^0$ | 91 | weak |
| 8 gluons | 0 | strong |

**Table 1.2:** Exchanged bosons and interactions in the Standard Model.

symmetry. They are massless and carry color quantum numbers. This last property allows the interaction of gluons with themselves. The self coupling of the gluons has a very singular consequence: the increase of the coupling of the strong interaction, $\alpha_S$, with the distance, which explains the confinement of quarks in bound states denominated hadrons and their behavior as free particles within the hadrons.

The electromagnetic and weak interactions appear unified in the SM via the electroweak interactions (EW) [6] which are described by the group $SU(2)_L \times U(1)_Y$. The $W^{\pm}$ and $Z^0$ are both massive particles and self-interacting; the $W^{\pm}$ are charged with $Q = \pm 1$ respectively and the $Z^0$ is electrically neutral; the $\gamma$ is a massless, chargeless particle and does not interact with itself. The fact that the weak bosons are massive indicates the Spontaneous Symmetry Breaking which is implemented in the SM as the so-called Higgs mechanism. This mechanism provides the mass to the weak bosons and to the fermions and leaves as a consequence a new particle, the Higgs boson. The Higgs boson remains undetected. The Large Hadron Collider (LHC), which is being built in Geneva(Switzerland) and will start operation in 2007 is bound to find the Higgs if it exists.

## 1.2   Deep Inelastic Scattering

The study of Deep Inelastic Scattering (DIS) processes is an essential tool to understand the structure of hadrons in terms of quarks and gluons.

In the DIS process, the incoming electron[2] interacts with the incoming proton by the exchange of a gauge boson. A generic electron-proton collision is depicted in figure 1.1. Depending on the exchanged boson, the interactions are classified as neutral current (NC) and charged current (CC). In NC , the interaction is mediated by a photon or a $Z^0$ boson. For the CC interactions the exchanged boson is a $W^{\pm}$.

---

[2]Electron and $e$ denote both electrons and positrons, unless stated otherwise.
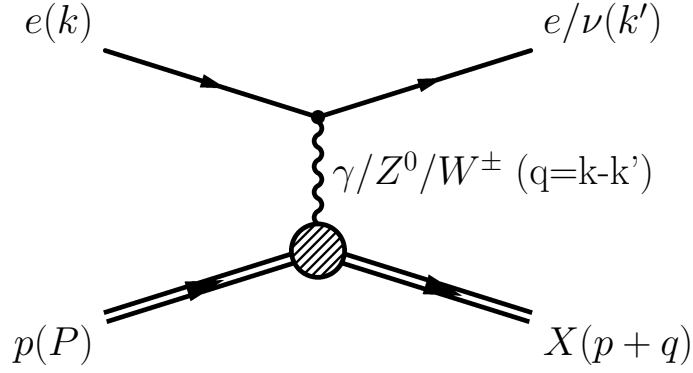
**Figure 1.1:** Electron-proton scattering.

Assuming that $k$ and $k'$ are the 4-momenta of the initial and final leptons and $P$ and $P'$ are the 4-momenta of the incoming proton and the final hadronic state respectively, the Lorentz invariant variables that describe the event kinematics are:

- the negative square of the 4-momentum of the exchanged boson

$$Q^2 = -q^2 = -(k - k')^2, \tag{1.1}$$

- the center-of-mass energy squared of the electron-proton system

$$s = (k + P)^2, \tag{1.2}$$

- the center-of-mass energy squared of the photon-proton system

$$W^2 = (q + P)^2 \approx \frac{Q^2}{x}(1 - x), \tag{1.3}$$

- the Bjorken scaling variable

$$x = \frac{Q^2}{2P \cdot q} \qquad 0 \leq x \leq 1, \tag{1.4}$$

- the inelasticity

$$y = \frac{q \cdot P}{k \cdot P} \qquad 0 \leq y \leq 1, \tag{1.5}$$

If the masses of the particles are neglected, the variables $Q^2$, $x$, $y$ and $s$ are related by $Q^2 = xys$.

The meaning of these variables becomes more clear when the interaction is viewed from the perspective of the Quark Parton Model (QPM). In the QPM,

the proton consists of point-like free constituents (partons)- which are identified as quarks and gluons. In this model, DIS is described as the interaction of an incoming electron with one of the partons of the proton by the exchange of the boson. From this point of view, $Q^2$ (also called virtuality) determines the resolving power of the interaction. In the DIS regime, in which $Q^2 \gg 1$ GeV$^2$ , the structure of the proton is probed down to $10^{-16}$cm. The Bjorken scaling variable $x$ corresponds to the fraction of the proton momentum carried by the struck parton and the inelasticity $y$ represents the fraction of the energy of the electron that is transferred to the interaction, measured in the proton rest frame.

## 1.2.1    Cross section and structure functions

The general form for the inclusive DIS cross section can be written as [5] :

$$d\sigma \sim L_{\mu\nu}W^{\mu\nu}, \tag{1.6}$$

where $L_{\mu\nu}$ and $W^{\mu\nu}$ are the leptonic and hadronic tensors. The leptonic tensor is calculable using Quantum Electrodymamics (QED). The hadronic tensor parametrizes the proton structure and it can be expressed in terms of the structure functions, $F_i(x, Q^2)$. The structure functions are process dependent and they can be determined experimentally. In this way, for unpolarized beams, the NC cross section is written as:

$$\frac{d^2\sigma^{NC}}{dxdQ^2} = \frac{4\pi\alpha_{EM}^2}{xQ^4}\left[(Y_+ F_2^{NC}(x, Q^2) - y^2 F_L^{NC}(x, Q^2) \mp Y_- xF_3^{NC}(x, Q^2)\right] , \tag{1.7}$$

where $\alpha_{EM}$ is the electromagnetic fine structure constant, $Y_\pm = 1 \pm (1 - y)^2$. $F_2$ is the major contribution to the NC cross section. $F_L(=F_2 - 2xF_1)$ is the contribution from the absorption of a longitudinally polarized photon and $F_3$ is the parity-violating contribution which is non-zero only for weak interactions.

Figure 1.2 shows a compilation of $F_2^{em}$ measurements[3] as a function of $Q^2$ for fixed values of $x$. For values of $x \sim 0.1$, $F_2^{em}$ is independent of $Q^2$ : this behavior is known as *scale invariance*. It was originally proposed by Bjorken [7] and observed for the first time at SLAC [8]. For the region of high and low $x$, a dependence of $F_2^{em}$ with $Q^2$ is observed, behavior referred to as *scaling violation*.

The *scale invariance* is the expected behavior of the structure functions in the frame of the QPM since the model assumes that the proton consists of non-interacting partons. However, the existence of *scaling violation* shows that the

---

[3]$F_2^{em}$ is the purely electromagnetic part of the $F_2^{NC}$ structure function.
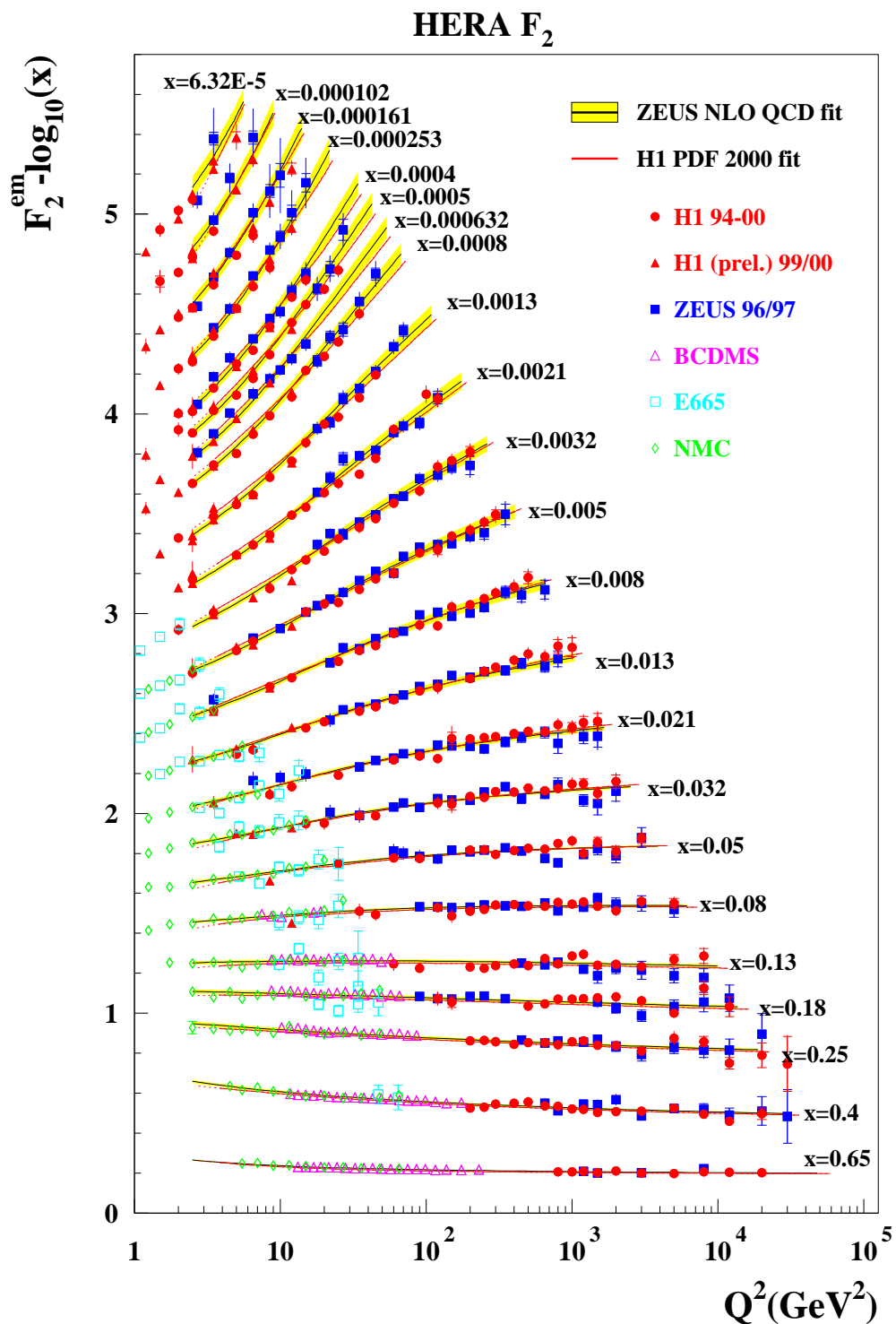
**Figure 1.2:** The structure function $F_2^{em}$ measured by different experiments as a function of $Q^2$ in different bins of $x$.

naive picture of the QPM has to be modified. Scaling violations originate from the coupling of quarks to gluons as predicted by QCD. The quarks can radiate gluons, which in turn can split into $q\bar{q}$-pairs. With increasing $Q^2$ more of these fluctuations can be resolved as illustrated in figure 1.3.



proton            proton substructure            QCD Compton            BGF

increasing resolving power $Q^2$
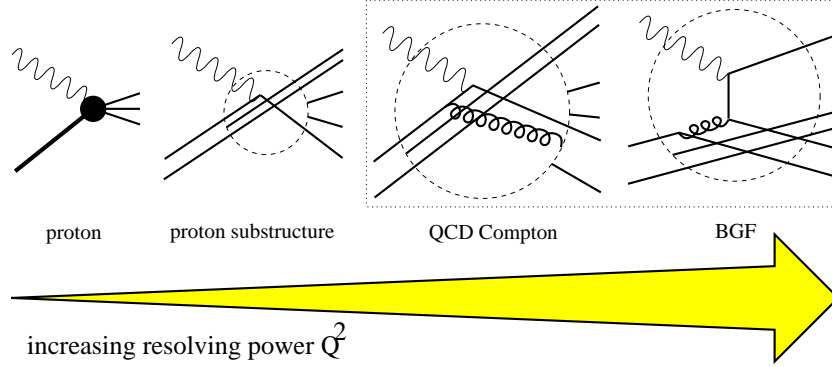
**Figure 1.3:** Schematic diagram of the scaling violations. Processes as gluon radiation or $q\bar{q}$ splitting can be resolved with large $Q^2$ .

## 1.2.2   The parton density functions

The parton density functions (PDFs), $f_{i/p}(x, \mu_F^2)$, denote the probability of finding a parton $i$, with momentum $x$ at a given value of $Q^2$. These distributions cannot be calculated from first principles in QCD. However, the QCD factorization theorem [9], symbolically represented in figure 1.4, allows to write the inclusive DIS cross sections as a convolution of two different parts:

$$\sigma_{ep}(x, Q^2) = \sum_{i \in partons} f_{i/p}(x, \mu_F^2) \otimes \sigma_{ei}(x, Q^2, \mu_F^2) . \tag{1.8}$$

$\sigma_{ei}$ denotes the cross section of the short distance interaction, i.e. the interaction between the electron and the parton $i$, which is calculable in perturbative QCD (pQCD). $f_{i/p}$ , the so-called long distance contribution, correspond to the PDF. The factorization scale, $\mu_F^2$, defines the scale at which the non-perturbative (gluon radiation) effects are absorbed in the definition of the PDFs.

Knowing the parton density functions at a particular value of $Q^2$ , the evolution equations make possible the determination of $f_{i/p}(x, Q^2)$ for any values of $Q^2$ within the range of applicability of pQCD. There are different evolution equation schemes like DGLAP [10], BFKL [11] or CCFM [12], which are used depending on the considered range of $x$ and $Q^2$ .
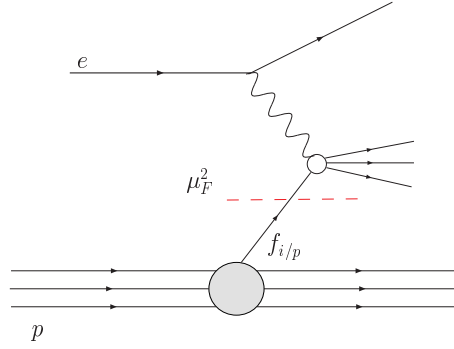
**Figure 1.4:** Symbolic representation of the QCD factorization theorem. $\mu_F^2$ corresponds to the factorization scale.

PDFs can be extracted from fits to the measured data with the help of the evolution equations. The factorization theorem states that the parton densities are process independent. Thus, the PDFs determined for a given process can be used to make predictions for other processes.

Figure 1.5 shows the PDFs extracted from ZEUS and H1 next to leading order (NLO) QCD analysis of DIS data. The $u$- and $d$-quark densities dominate at large values of $x \gtrsim 0.3$, while sea quarks and gluons become relevant at lower values of $x$.

### 1.2.3   Radiative $ep$ scattering

Higher order QED effects, such as emission of real photons and loop corrections, contribute to the Born level $ep$ cross section. Among these processes, only the real photon emission can be experimentally detected. The lowest order Feynman diagrams for the emission of a real photon from the lepton side are depicted in figure 1.6. The amplitudes of both diagrams and the interference between them contribute to the $ep \to e\gamma X$ cross section, therefore there is no possibility to determine whether a particular event corresponds to the left or right diagram in figure 1.6.

For both Feynman diagrams in figure 1.6, the corresponding amplitude contains in the denominator the following terms:

$$(q'^2 - m_e^2)q^2 \quad \text{for the left diagram and}$$
$$(q''^2 - m_e^2)q^2 \quad \text{for the right diagram,}$$

where $q'$, $q''$ and $q$ are the particle 4-momenta as depicted in figure 1.6. The dominant contributions appear when these terms tend to zero and according with this the following classification [13] is given:
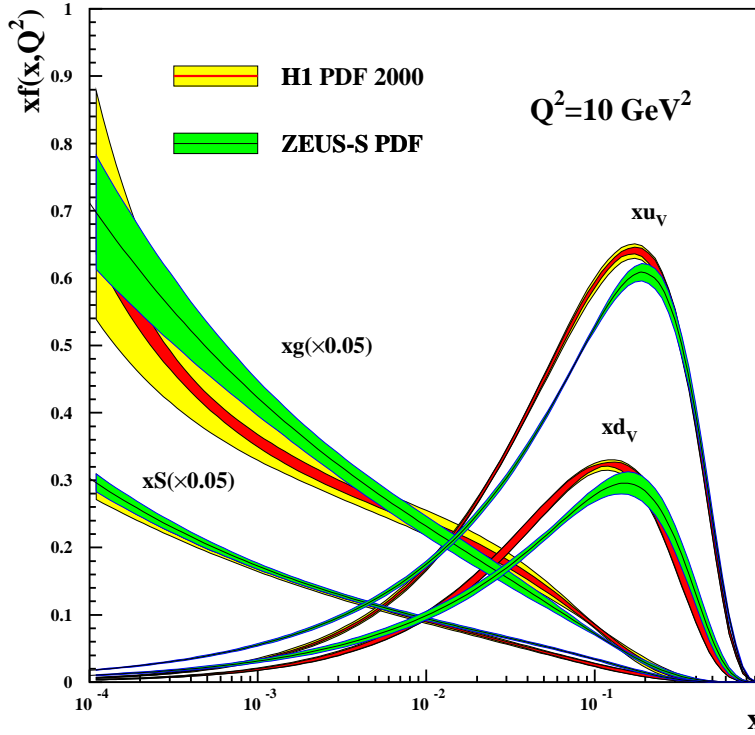
**Figure 1.5:** Proton PDFs extracted from ZEUS and H1 NLO QCD fits at $Q^2 = 10$ GeV$^2$ .

- $q'^2 \simeq 0$ (or $q''^2 \simeq 0$) and $q^2 \simeq 0$. This configuration corresponds to the so-called bremsstrahlung process. The electron and the photon scatter a very small polar angles. This process has a high cross section and it is used to measure the luminosity in the ZEUS experiment (see section 2.2.6).

- $q^2$ is finite and either $q'^2 \simeq 0$ or $q''^2 \simeq 0$. In this configuration the photons are emitted collinear either with the initial or final electron. The first case is called Initial State Radiation (ISR) and its cross section is dominated by the left diagram in figure 1.6. This process can be interpreted as a DIS event with a reduced center of mass. The second possibility is referred to as Final State Radiation (FSR). These events usually can not be distinguished from a normal DIS event. The small angles at which the photon is emitted w.r.t the electron direction makes the experimental separation between the two is not possible.

- $q^2 \simeq 0$ and either $q'^2$ or $q''^2$ are finite. This configuration corresponds to the case in which the electron and the photon are detected at large polar angles and their total transverse momentum is close to zero. This configuration is called QED Compton Scattering[4] since it involves the scattering of a

---

[4]In the context of the analysis of the DVCS process, this configuration is referred to as
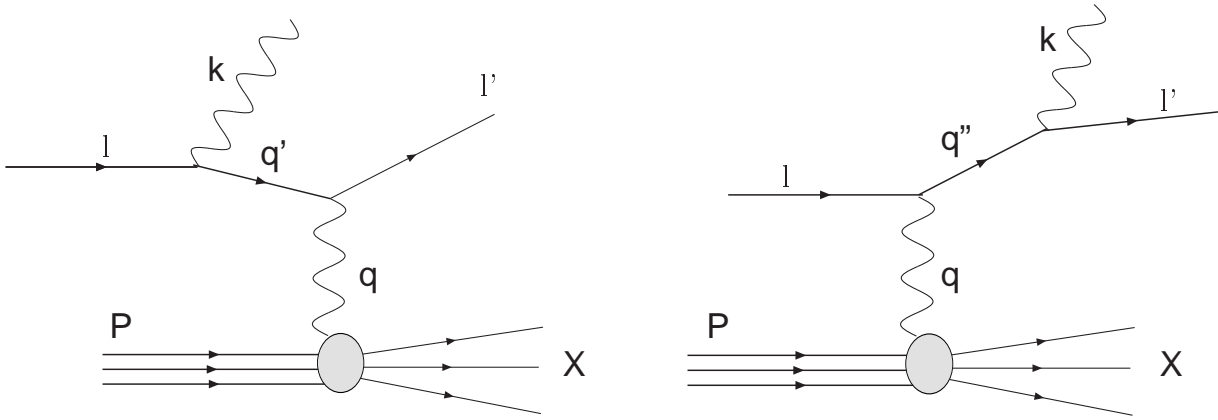
**Figure 1.6:** Lowest order Feynman diagrams for the emission of a real photon from the electron line.

quasi-real photon on an electron.

## 1.3   Diffraction

Reactions in which no quantum numbers are exchanged between the high energy collinding particles are attributed to diffractive interactions. They are characterized by the presence of a large rapidity[5] gap in the final state.

These interactions were first observed in hadron-hadron scattering. In the 1960s, a phenomenological model was developed in order to describe the soft hadron-hadron scattering: the Regge theory [14]. In this theory, the interactions are viewed as exchanges of the so-called "Regge trajectories" which are classified according to their quantum numbers.

The Regge model has been very successful in describing the total cross section for hadron-hadron collisions as well as other properties of the elastic and diffractive production in hadron-hadron interactions. The total cross section firstly decreases with increasing center-of-mass energy but then it starts to rise again: the description of this rise required the introduction of a new trajectory with the quantum numbers of the vacuum, the Pomeron ($\mathbb{P}$) trajectory [15], which is the trajectory exchanged in diffractive interactions.

In figure 1.7, the differential cross section for elastic proton-proton scattering is plotted as a function of $|t|$, where $t$ is the squared 4-momentum transfer between

---

Bethe-Heitler process. In this thesis this notation has been followed.

[5]The rapidity is defined as $y = \frac{1}{2} ln\frac{E+p_{||}}{E-p_{||}}$, where E is the energy and $p_{||}$ is the longitudinal momentum of a particle.

the two protons. The shape shows a large peak followed by minima and maxima. In classical optics, this kind of pattern is associated with the diffraction of light on a disk of radius $R$ with the intensity, $I$, being expressed by

$$\frac{I}{I_0} \simeq 1 - \frac{R^2}{4}(k\theta)^2, \tag{1.9}$$

where $\theta$ is the scattering angle and $k$ denotes the wave number. For small values of $|t|$, the cross section for elastic proton-proton scattering can be approximated by the expression

$$\frac{\frac{d\sigma}{dt}}{\frac{d\sigma}{dt}(t = 0)} \simeq e^{-b|t|} \simeq 1 - b|t|, \tag{1.10}$$

where the $t$-slope $b$ can be written as $b = R^2/4$ and, in analogy with the optical case, $b$ is related to the target size, where R represents the transverse radius of the interaction. This behavior was found for other diffractive reactions, so the term diffraction was adopted for all the processes.

## 1.3.1   Diffraction in DIS

The study of the diffractive events found at HERA [16] has led to a significant progress in understanding the diffractive exchange. Following the idea by Ingelmann and Schlein [17], the presence of a hard scale in the interaction could help to understand the nature of the Pomeron. Furthermore, it was tried to described in QCD the Pomeron as two-gluon exchange and this approach can be tested with diffractive events in DIS.

A diffractive process in DIS (see figure 1.8) has a general form

$$e(k) + P(p) \rightarrow e'(k') + P'(p') + X, \tag{1.11}$$

where $X$ represents the final state originating from the proton and $P'$ is the final state proton. For the complete description of the events it is necessary to introduce new variables in addition to the usual DIS variables described in section 1.2:

$$t = (p - p')^2, \tag{1.12}$$

$$x_{\mathbb{P}} = \frac{q \cdot (p - p')}{q \cdot p} \simeq \frac{M_X^2 + Q^2}{W^2 + Q^2}, \tag{1.13}$$

$$\beta = \frac{Q^2}{2q \cdot (p - p')} = \frac{x}{x_{\mathbb{P}}} \simeq \frac{Q^2}{W^2 + Q^2}, \tag{1.14}$$
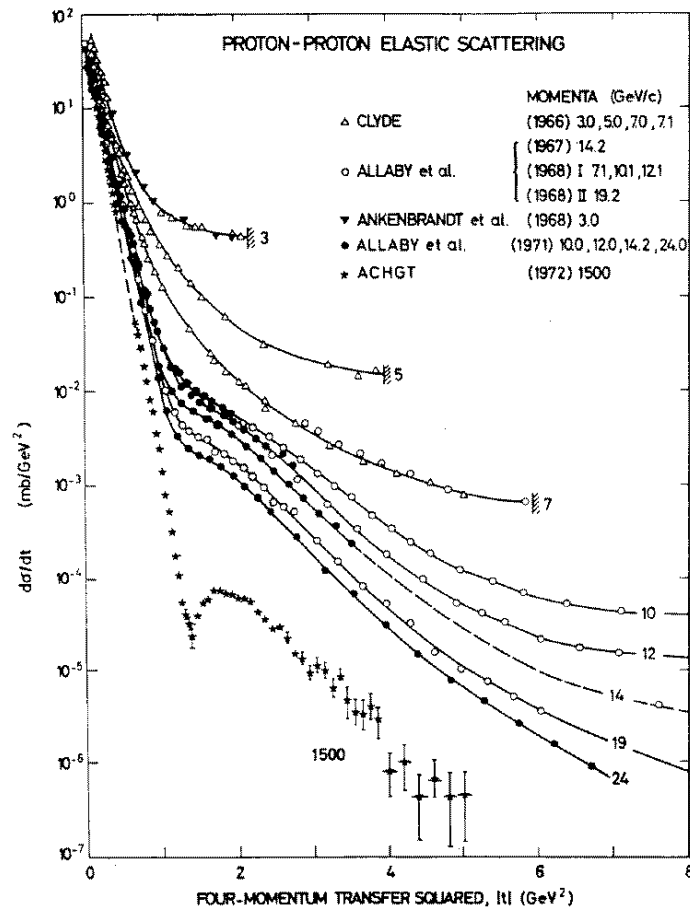
**Figure 1.7:** Measurements of the differential cross section for elastic $pp$ scattering as a function of $|t|$ for different values of the center-of-mass energy.
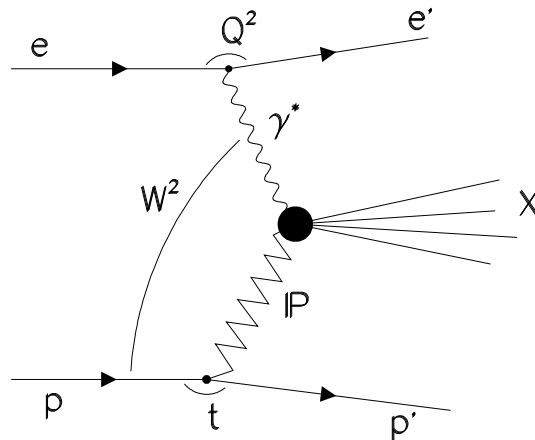


**Figure 1.8:** Schematic diagram of a diffractive event in DIS.

13

where $x_{\mathbb{P}}$ is the fractional proton momentum which participates in the interaction, $\beta$ is equivalent to the Bjorken $x$ but relative to the momentum $(p - p')$ and $M_X$ corresponds to the invariant mass of the hadronic finale state.

The cross section for the inclusive diffractive scattering can be expressed in terms of the diffractive structure functions $F_2^D$ and $F_L^D$

$$\frac{d^4\sigma^D}{d\beta dQ^2 dx_{\mathbb{P}} dt} = \frac{4\pi\alpha_{EM}^2}{\beta Q^2}\left[(1 - y + \frac{y^2}{2}F_2^D(\beta, Q^2, x_{\mathbb{P}}, t) - \frac{y^2}{2}F_L^D(\beta, Q^2, x_{\mathbb{P}}, t)\right]$$
$$(1.15)$$

Figure 1.9 shows the measurement of the $F_2^D$ at $x_{\mathbb{P}} = 0.01$ as a function of $Q^2$ in different bins of $\beta$. $F_2^D$ increases with $Q^2$ . This positive scaling suggests that the partons probed in the diffractive processes are mainly gluons. The factorization theorem was proven for diffraction [18], leading to the definition of the diffractive PDFs (DPDFs). Like in the case of the usual PDFs, the diffractive PDFs have been extracted from fits to $F_2^D$ measurements and have been used to predict the cross section for different diffractive processes. However, the use of the diffractive PDFs obtained at HERA is limited. Big discrepancies have been found when describing diffractive events produced in $p\bar{p}$ at TEVATRON because factorization in hadron-hadron collisions does not hold due to the soft interactions between the spectator partons [18, 19].

The study of exclusive diffractive events, like vector meson production, $ep \rightarrow e'Vp'$, has also improved the understanding of diffraction. Figure 1.10 shows the cross section for the production of different vector mesons as a function of W. The measurements were done in the photoproduction $(Q^2 \sim 0)$ regime. The rise of the cross section for the light vector mesons is compatible with the predictions of Regge theory. For the heavy vector mesons, where a hard scale is given by the vector meson mass, the rise is steeper than the Regge prediction. These kind of processes are calculable within pQCD. The rapid increase of the cross section with W reflects the rise of the gluon density at low x.

## 1.4   The generalized parton distributions

The study of the parton density functions has played an important role in understanding the structure of hadrons. However, these phenomenological functions are not the only way to parametrize the structure of hadrons. In recent years, generalized parton distributions (GPDs) have become a powerful tool to continue the study of the composition of hadrons. The GPDs encode information about
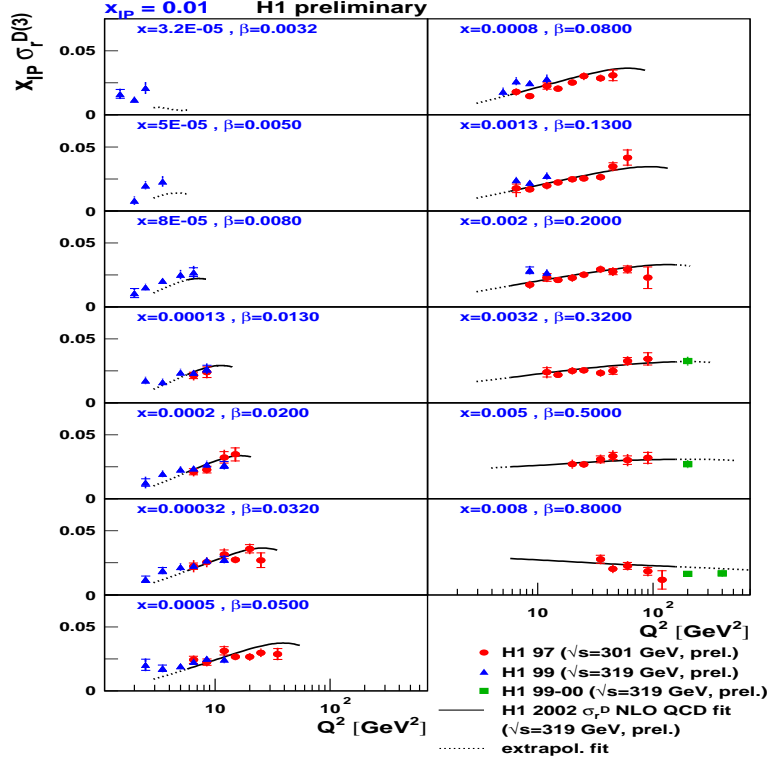
**Figure 1.9:** Measurements of the diffractive structure function $F_2^D$ as a function of $Q^2$. Plot taken from [20].

the three-dimensional spatial structure of the nucleon, parton correlations and direct measurements of the orbital angular momentum of the quarks. Recent reviews on the GPDs can be found in [22].

The factorization theorem is applicable not only for inclusive processes, as explained in section 1.2.2, but also for exclusive reactions in which there is a finite momentum transfer to the target. For these kind of reactions, the separation between short- and long-distance parts is possible and the long-distance terms are parametrized by GPDs. Processes as Deeply Virtual Compton Scattering, which is the subject of this thesis, as well as the production of vector mesons (VM) can be described inside this framework. In figure 1.11, the leading diagrams for DVCS and VM production are shown.

The GPDs depend on the longitudinal momentum fractions $x$ and $\xi$[6] and on the Mandelstam variable $t = (p - p')^2$. The term longitudinal refers to the direction of the initial and final state proton in a frame where both move fast. In the Bjorken limit, i.e. for $Q^2 \to \infty$ and $x_B$[7] being fixed, the skewedness is

---

[6]Usually known as *skewedness* parameter.

[7]Bjorken scaling variable, as defined in the equation 1.4.
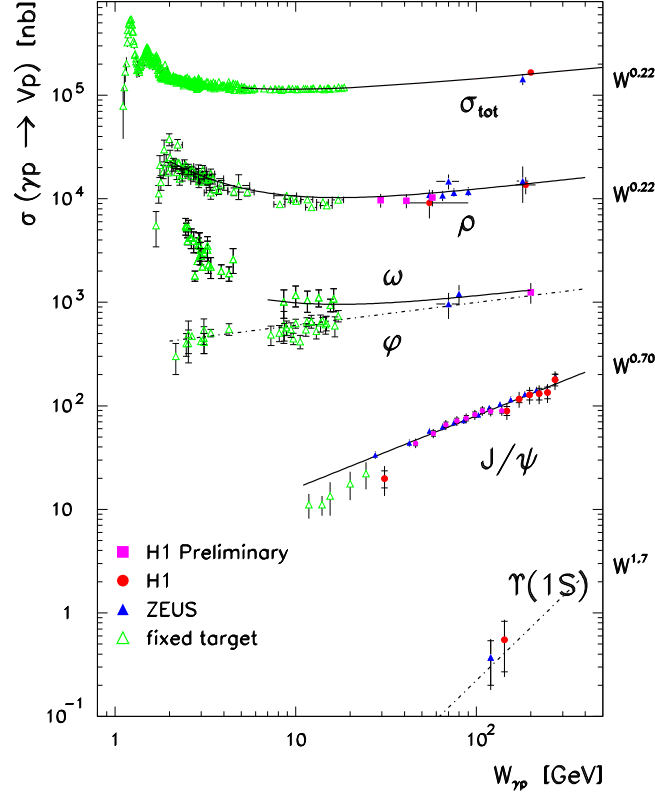
**Figure 1.10:** Measurement of the cross section for the production of different vector mesons in photoproduction as a function of W. The lines illustrate different power-law energy dependencies. Plot taken from [21].
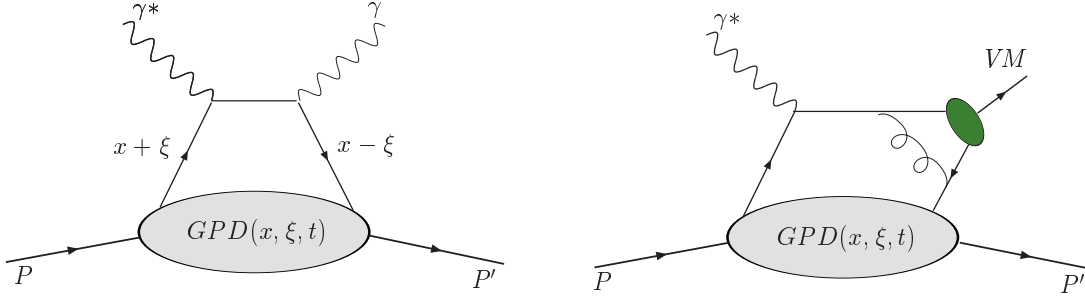


**Figure 1.11:** QCD leading diagrams of DVCS and VM production.

written as

$$\xi \approx \frac{x_B}{2 - x_B}. \tag{1.16}$$

As seen in figure 1.11 left, the parton and proton momenta are not the same in the left- and right-hand sides of the diagrams, therefore the GPDs represent the interference between amplitudes describing different states of the nucleon. In

this way, the GPDs enter in the calculation of scattering amplitudes which are further squared in order to obtain the cross section, unlike the PDFs, which are defined on the cross section level.

Using QCD evolution equations it is possible to determine the $Q^2$ dependence of GPDs. There are two different regimes, the DGLAP region which corresponds to $|x| > \xi$ and the ERBL region, valid for $|x| < \xi$. The evolution has been calculated in leading [23–26] and next-to-leading [27] order in $\alpha_s$.

### 1.4.1  Definition of the GPDs

The generalized parton distributions can be defined by the Fourier transforms of the hadronic matrix elements:

$$\int \frac{d\lambda}{2\pi} e^{i\lambda x} \langle P' \mid \overline{\psi}_q(-\lambda n/2) \gamma^\mu \psi_q(\lambda n/2) \mid P \rangle =$$

$$H^q(x,\xi,t)\overline{U}(P')\gamma^\mu U(P) + E^q(x,\xi,t)\overline{U}(P')\frac{i\sigma^{\nu\mu}\Delta_\nu}{2M}U(P) + \cdots ,$$

$$\int \frac{d\lambda}{2\pi} e^{i\lambda x} \langle P' \mid \overline{\psi}_q(-\lambda n/2) \gamma^\mu \gamma_5 \psi_q(\lambda n/2) \mid P \rangle =$$

$$\tilde{H}^q(x,\xi,t)\overline{U}(P')\gamma^\mu \gamma_5 U(P) + \tilde{E}^q(x,\xi,t)\overline{U}(P')\frac{\gamma_5 \Delta^\mu}{2M}U(P) + \cdots , \quad (1.17)$$

where $|P\rangle$ and $\langle P'|$ represent the quantum number of the incoming and outgoing proton, respectively. $\overline{\psi}_q(-\lambda n/2)\gamma^\mu \gamma_5 \psi_q$ and $\overline{\psi}_q(-\lambda n/2)\gamma^\mu \psi_q(\lambda n/2)$ represent a set of quark operators. $U(P)$ and $\overline{U}(P')$ are the Dirac spinors of the proton and $\Delta^\mu$ is defined as $\Delta^\mu = P'^\mu - P^\mu$. The ellipses denote the higher-twist distributions.

In total there are eight GPDs for each quark flavor $q$. Four of them, $H^q, \tilde{H}^q, E^q$ and $\tilde{E}^q$, conserve the parton helicity. Another four are defined in the case of parton helicity flip $H_T^q, \tilde{H}_T^q, E_T^q$ and $\tilde{E}_T^q$. Also the pairs $(H^q, E^q)$ and $(\tilde{H}^q, \tilde{E}^q)$ are known as unpolarized and polarized GPDs respectively. Analogous definitions can be made for the gluons.

Figure 1.12 shows the measurement done by the HERMES collaboration of the cross section for exclusive $\pi^+$ production. This reaction is sensitive to the polarized GPDs. Hence the data are compared with GPD model calculations [28].

### 1.4.2  Basic properties of the GPDs

The generalized parton distributions satisfy a set of constraints which lead to a partial knowledge of them in specific kinematic regions.
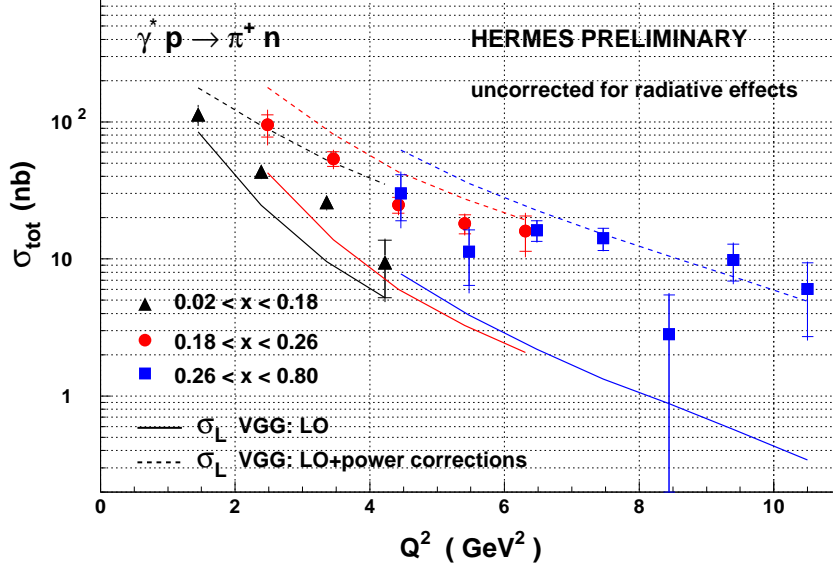
**Figure 1.12:** Exclusive $\pi^+$ production cross section as a function of $Q^2$ for different $x_B$ range measured by the HERMES collaboration. The lines correspond to a GPD model calculations.

In the forward limit, $t \to 0$ and equal helicities for initial and final state proton, $H^q$ and $\tilde{H}^q$ reduce to the ordinary spin-dependent and spin-independent quark distributions:

$$H^q(x,0,0) = q(x) \qquad \tilde{H}^q(x,0,0) = \Delta q(x), \qquad (1.18)$$

note that when $t$ goes to zero also $\xi \to 0$. For gluons, the relations read as

$$H^g(x,0,0) = xg(x) \qquad \tilde{H}^g(x,0,0) = x\Delta g(x). \qquad (1.19)$$

The distributions that do not conserve the helicity of the proton, E and $\tilde{E}$ for quark and gluons, are not accessible in the forward limit and thus no relations to the usual PDFs exists. Among the helicity flip distributions, only the $H_T^q$ can be measured in the forward limit and it is equivalent to the quark transversity distribution usually denoted by $\delta q(x)$.

The first moments of the quark GPDs are equal to the corresponding quark form factors in the nucleon:

$$\int_{-1}^{1} dx H^q(x,\xi,t) = F_1^q(t), \qquad \int_{-1}^{1} dx E^q(x,\xi,t) = F_2^q(t),$$

$$\int_{-1}^{1} dx \tilde{H}^q(x,\xi,t) = G_A^q(t), \qquad \int_{-1}^{1} dx \tilde{E}^q(x,\xi,t) = G_P^q(t), \qquad (1.20)$$

where $F_1^q(t)$ and $F_2^q(t)$ are the Dirac and Pauli form factors and $G_A^q(t)$ and $G_P^q(t)$ are the axial and pseudoscalar form factors.

The Ji's sum rules [29] are related with the second moments of the GPDs:

$$
\begin{aligned}
\int_{-1}^{1} dx\ x[H^q(x,\xi,t) + E^q(x,\xi,t)] &= A_q(t) + B_q(t), \\
\int_{0}^{1} dx\ x[H^g(x,\xi,t) + E^g(x,\xi,t)] &= A_g(t) + B_g(t),
\end{aligned}
\tag{1.21}
$$

where $A$ and $B$ are the form factors that appear in the polynomial decomposition[8] of the GPDs. The importance of these expressions above arise from their relation with the spin of the nucleon. The spin of the nucleon is given by the gauge invariant sum

$$
\frac{1}{2} = J^Q + J^G = \frac{1}{2}\Delta\Sigma + L^Q + J^G,
\tag{1.22}
$$

where $\Delta\Sigma$ and $L^Q$ are the quark spin and orbital angular momentum contribution and $J^G$ is the total angular momentum of the gluons. In the limit $t \to 0$

$$
J^{Q,G} = \frac{1}{2}[A_{q,g}(0) + B_{q,g}(0)].
\tag{1.23}
$$

Introducing the above expression in the equations 1.21 it can be obtained

$$
J^Q = \frac{1}{2}\int_{-1}^{1} dx\ x[H^q(x,\xi,t) + E^q(x,\xi,t)],
\tag{1.24}
$$

where the $\xi$ dependence disappears in the forward limit. Analogous expressions are found for the gluons.

From the relations above is clear the importance of the GPDs to solve the puzzle of the spin of the nucleon; in particular, the $L^Q$ contribution can be derived since there is information about $\Delta\Sigma$ which comes from measurements of inclusive and seminclusive polarized DIS. The total angular momentum of the gluons can also be obtained.

## 1.5  Deeply Virtual Compton Scattering

The exclusive lepton-nucleon[9] processes have revealed to be a very useful tool in order to study the hadron structure in terms of GPDs. Among all, Deeply Virtual

---

[8]The $x$-integral of $x^n H^q$ and of $x^n E^q$ are polynomials in $\xi$ of order $n+1$.

[9]i.e. the photoproduction of lepton pairs, $\gamma N \to l^+ l^- N'$, or the neutrino production of a real photon, $\nu_l N \to l N' \gamma$, are other processes used for GPDs studies [30, 31].

Compton Scattering (DVCS), $\gamma^\star p \rightarrow \gamma p'$ , which is defined as the diffractive production of a real photon, is the most promising.

The usual way to depict the DVCS process is with the 'handbag' diagrams, which are shown in figure 1.13, for leading order (LO) and next-to-leading order (NLO). For both cases, the real photon is originating from the quark line. In NLO, unlike in the LO case, the virtual photon interacts with two gluons via a quark loop. The initial photon in the reaction is virtual and the outgoing photon
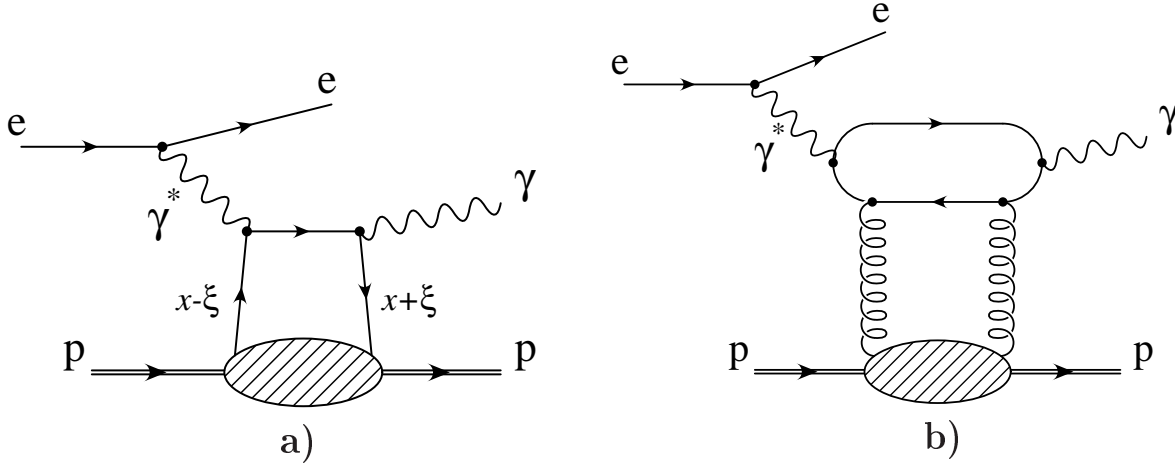


**Figure 1.13:** QCD diagrams for DVCS: a) LO diagram, where $\xi$ is the *skewedness* parameter. b) NLO diagram showing the interaction of the photon with two glouns from the proton.

is real which means that the momentum fraction carried by the quarks is, in general, unequal, as shown in the diagram (a) in figure 1.13. This illustrates the concept of GPDs as functions that describe two parton correlations in the proton since one is looking at what happens when a parton is removed from the proton and later replaced with different momentum.

One of the reasons why DVCS is the preferred process to study the GPDs is that its treatment, from the theoretical point of view, is well controlled. In contrast with the exclusive vector meson production [32], DVCS does not suffer from uncertainties associated to the description of the final state, since this is a real $\gamma$. Also the effects of NLO [33–35] and sub-leading twist [10] [37–39] have been studied.

As mentioned before (see section 1.4), according to the QCD factorization theorem, in the region of $Q^2$ large and small $t$, exclusive processes can be expressed

---

[10]The term *twist* stands for the order in $M/Q$ in which an operator matrix element contributes; effects labelled with *twist-h* enter in the hard process with a suppression higher than $(M/Q)^{h-2}$ [36].

by a convolution of the computable short-distance cross sections and the GPDs. Specifically, the DVCS amplitudes can be written as a function of the Compton Form Factors (CFFs) [39],

$$\mathcal{F} = \sum_q \int_{-1}^{1} dx C_q^{\mp}(x, \xi) F^q(x, \xi, t), \tag{1.25}$$

which are the sum over the flavor $q$ of the convolution of the perturbatively calculable coefficient functions $C_q^{\mp}$ and the generalized parton distributions $F^q = H^q, E^q, \tilde{H}^q, \tilde{E}^q$ [11]. The sign $-(+)$ in the coefficient $C$ applies to the CFFs $\mathcal{F} = \mathcal{H}, \mathcal{E}(\tilde{\mathcal{H}}, \tilde{\mathcal{E}})$ corresponding to the GPDs $F^q = H^q, E^q, (\tilde{H}^q, \tilde{E}^q)$.

## 1.5.1   DVCS and Bethe-Heitler

Another feature that makes DVCS a unique process to extract information on GPDs is its interference with the Bethe-Heitler (BH) process. In BH, the photon is radiated from the initial or final lepton (see figure 1.14).
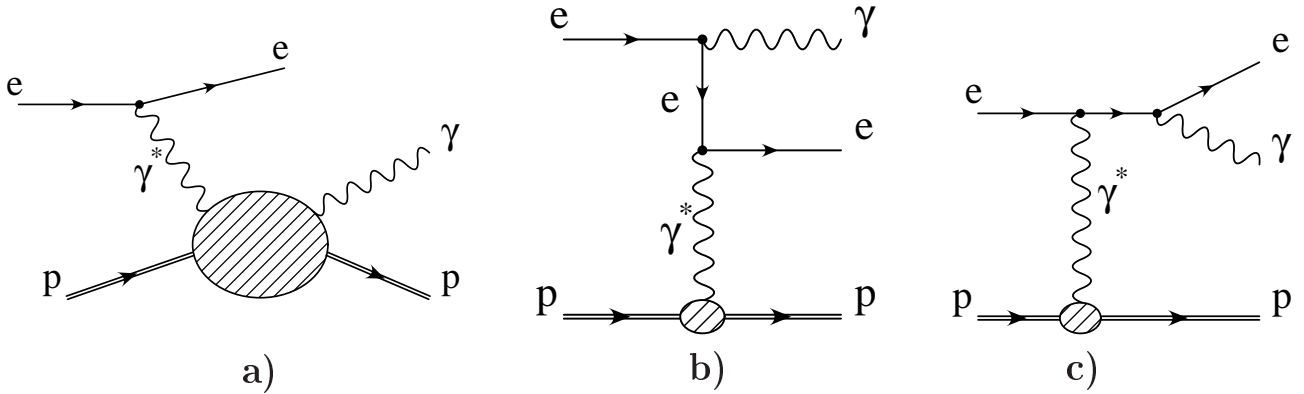


**Figure 1.14:** Diagrams illustrating the DVCS (a) and the BH (b) and (c) processes.

DVCS is studied in $ep$ collisions trough the reaction

$$e(k) + p(P) \rightarrow e'(k') + \gamma + p'(P'), \tag{1.26}$$

where the proton can either remain intact (elastic case), be excited into a resonance state (quasi-elastic case) or break up (inelastic case). Since BH has the same final state as DVCS, both mechanism contribute to the cross section and have to be added on the amplitude level, hence

$$\frac{d\sigma^{ep \rightarrow e'\gamma p'}}{dx_B dQ^2 d|t| d\phi} \propto |\mathcal{T}_{DVCS}|^2 + |\mathcal{T}_{BH}|^2 + \underbrace{(\mathcal{T}_{DVCS}^{\star} \mathcal{T}_{BH} + \mathcal{T}_{DVCS} \mathcal{T}_{BH}^{\star})}_{\mathcal{I}} \tag{1.27}$$

---

[11]$H^q, E^q, \tilde{H}^q, \tilde{E}^q$ are the GPDs introduced in section 1.4.1.

**21**

where $\mathcal{I}$ represents the interference term and $\phi$ is the azimuthal angle between the lepton plane, defined by the initial and final lepton trajectories, and the hadronic plane which is defined by the virtual and the real photon directions.

The three terms in (1.27) can be expressed as Fourier series in $\phi$ [39]. The coefficients of the expansion are functions of the CFFs and thus, related with the GPDs. For unpolarized[12] target the expansions read

$$|\mathcal{T}_{DVCS}|^2 = \frac{e^6}{y^2 Q^2}\left\{c_0^{DVCS} + \sum_{n=1}^{2} c_n^{DVCS}\cos(n\phi) + \lambda s_1^{DVCS}\sin(n\phi)\right\}, \qquad (1.28)$$

$$|\mathcal{T}_{BH}|^2 = \frac{e^6}{K^2(1+\epsilon^2)^2\mathcal{P}_1(\phi)\mathcal{P}_2(\phi)}\left\{c_0^{BH} + \sum_{n=1}^{2} c_n^{BH}\ cos(n\phi)\right\}, \qquad (1.29)$$

$$\mathcal{I} = \frac{\pm e^6}{Kyt\mathcal{P}_1(\phi)\mathcal{P}_2(\phi)}\left\{c_0^{\mathcal{I}} + \sum_{n=1}^{3} c_n^{\mathcal{I}}\cos(n\phi) + \sum_{n=1}^{2}\lambda s_n^{\mathcal{I}}\sin(n\phi)\right\}, \qquad (1.30)$$

where $K \equiv x_B yt$ and $\epsilon \equiv 2x_B M/Q$. The sign + (-) in the interference term corresponds to positively (negatively) charged lepton beams. The symbol $\lambda$ stands for the polarization of the lepton beams, i.e. $\lambda = +1$ for longitudinal polarization. The lepton BH propagators, $\mathcal{P}_{1,2}$, introduce an additional dependence on $\phi$ in the interference and pure BH terms, however this contribution is kinematically suppressed by at least $1/Q$. Exact expressions of the Fourier coefficients for pure DVCS , pure BH and $\mathcal{I}$ contributions can be found in [39], here we only discuss some general features:

- Pure BH terms: $c_n^{BH}$
  The coefficients are expressed only as a function of the known Dirac and Pauli form factors, $F_1(t)$ and $F_2(t)$.

- Pure DVCS terms: $c_n^{DVCS}$, $s_1^{DVCS}$
  The coefficients are bilinear in the CFFs. While $c_0^{DVCS}$ arise at twist-2 the rest, $c_1^{DVCS}$ and $s_1^{DVCS}$, are twist-3 contributions and therefore suppressed. The coefficient $c_2^{DVCS}$ is related to the twist-2 helicity-flip gluonic GPDs but is suppressed by $\alpha_s$-power corrections.

- $\mathcal{I}$ terms: $c_n^{\mathcal{I}}$, $s_n^{\mathcal{I}}$
  A combination of CFFs appear linearly in the expressions of the coefficients. The twist-2 contributions are given by $c_0^{\mathcal{I}}, c_1^{\mathcal{I}}, s_1^{\mathcal{I}}$. $c_3^{\mathcal{I}}$ is related to helicity-flip gluonic GPDs and therefore suppressed. The rest, $c_2^{\mathcal{I}}$ and $s_2^{\mathcal{I}}$ are twist-3 contribution and are suppressed.

---

[12]The expansions for the cases of longitudinal or transverse polarized target can be found in [39].

The access to the GPDs can be done with the help of observables that disentangle the different contribution in the coefficients.

Measurement of the total cross section (see equation 1.27) integrated over the angle $\phi$ allow the extraction of the pure DVCS cross section, $\sigma(\gamma^\star p \rightarrow \gamma p')$, since the contribution of the interference term $(c_0^\mathcal{I})$ is kinematically suppressed at leading-twist. A simple subtraction of the BH cross section from the total leads to the DVCS cross sections. Indirect insights on the GPDs, which help to their modelling, can be achieved with the cross section measurements.

Using the interference term it is possible to obtain information about the real and imaginary parts of the $\mathcal{T}_{DVCS}$ (see section 1.5.4) and, since the CFFs enter linearly in the coefficients they are more easily accessible. Direct measurements of the GPDs are therefore possible. The observables that allow to extract information from the $\mathcal{I}$ are different asymmetries, e.g. the beam-spin or beam-charge asymmetry.

Measurements, concerning cross section as well as asymmetries, performed until now together with the relevant physics results are going to be reviewed in sections 1.5.3 and 1.5.4.

## 1.5.2 Theoretical models for DVCS

**GPD-based model**

Predictions for DVCS cross section have been calculated by Frankfurt, Freund and Strikman within pQCD [40]. This theoretical prediction will be referred to as FFS model.

The two ingredients to calculate the amplitude of the DVCS process are the hard and the soft contributions. The value of the amplitude at the normalization point $Q_0^2$ is not known since it is given by the soft contributions (non-perturbative effects). The FFS model uses the aligned jet model (AJM) [41] to describe the soft contribution. The hard contribution is calculated based on the diagram shown in figure 1.13b.

The imaginary part of the DVCS amplitude was computed with the AJM and compared with the imaginary part of the DIS amplitude

$$R = \frac{\Im m \mathcal{T}_{DIS}}{\Im m \mathcal{T}_{DVCS}} \simeq 0.5 \tag{1.31}$$

for typical AJM $Q_0^2$ of 1-3 GeV$^2$ . The AJM provides a reasonable description of the structure function $F_2$, the comparison above enables the normalization of the

DVCS amplitude at the input scale using $F_2$ data. The factor $R$ is directly related to the ratio GPDs to PDFs [42]. The imaginary part of the DVCS amplitude was then calculated at LO using the QCD evolution equation framework.

The real part of the DVCS amplitude was obtained using a dispersion relation

$$\eta = \frac{\Re e \mathcal{T}_{DVCS}}{\Im m \mathcal{T}_{DVCS}} = \frac{\pi}{2} \frac{d \ln(\Im m \mathcal{T}_{DIS})}{d \ln(1/x)} \tag{1.32}$$

where $\Im m \mathcal{T}_{DVCS}$ was connected via optical theorem with the DIS cross section and therefore with the structure function $F_2$.

The complete formulae for the cross section is given by

$$\frac{d\sigma^{DVCS}}{dxdydtd\phi} = \frac{\pi\alpha^3 s}{4R^2 Q^6}(1 + (1-y)^2)e^{-b|t|}F_2^2(x,Q^2)(1+\eta^2), \tag{1.33}$$

$$\frac{d\sigma^{BH}}{dxdydtd\phi} = \frac{\alpha^3 s y^2(1+(1-y)^2)}{\pi Q^4 |t|(1-y)}\left[\frac{G_E(t) + \frac{|t|}{4m_p^2}G_M(t)}{1 + \frac{|t|}{4m_p^2}}\right], \tag{1.34}$$

$$\frac{d\sigma^{\mathcal{I}}}{dxdydtd\phi} = \pm\frac{\eta\alpha^3 s y(1+(1-y)^2)}{2RQ^5\sqrt{|t|(1+y)}}e^{-b|t|/2}F_2(x,Q^2)$$
$$\times\left[\frac{G_E(t) + \frac{|t|}{4m_p^2}G_M(t)}{1 + \frac{|t|}{4m_p^2}}\right]\cos(\phi), \tag{1.35}$$

where $b$ is the slope of the exponential $t$-dependence, $m_p$ is the mass of the proton and $G_E(t)$ and $G_M(t)$ are the electric and magnetic form factors, respectively.

Further developments of this model can be found in [43]. The main differences are that the GPDs are evolved rather than the imaginary part of the DVCS amplitude and both part of $\mathcal{T}_{DVCS}$, imaginary and real, are computed directly.

**Color-Dipole based model**

The Color-Dipole model (CDM) [44] explains the diffractive processes from a perspective different to the one adopted until now. It has successfully described inclusive diffraction and exclusive processes. The DVCS cross section has been calculated also using this model.

The CDM assumes a factorization of the reaction in three subprocesses (see figure 1.15), which are well separated in time:

1. The virtual photon fluctuates into a $q\bar{q}$ pair (color dipole).

2. The color-dipole interacts with the proton.

3. The scattered pair annihilates to form the final state, in our case the real photon.

The time-scale in which the dipole interacts with the proton are much shorter than the life-time of the fluctuations and the time required for the formation of the final state. Therefore is a good approximation to consider that the interaction itself is independent of the two other processes. This assumption together with the fact that the dipole is frozen [13] during the interaction leads to the concept of the dipole cross section, $\sigma_d$, which describes the scattering probability of a dipole in a given configuration.
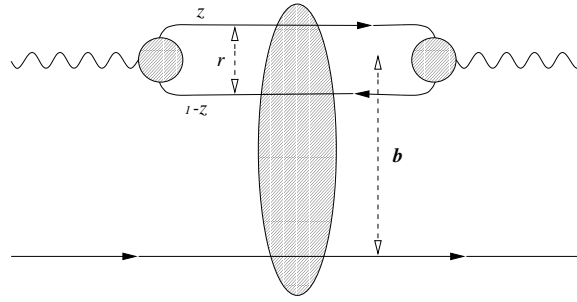


**Figure 1.15:** View of the interaction of the virtual photon with the proton in the Color-Dipole model.

In the CDM, the amplitude for the DVCS process can be written as

$$\mathcal{T}(\gamma^\star p \to \gamma p') = \int_{z,R} \psi_{\gamma^\star}^{IN} \sigma_d \psi_\gamma^{OUT} \qquad (1.36)$$

where $\psi_{\gamma^\star}^{IN}$ and $\psi_\gamma^{OUT}$ represent the wave functions for the incoming virtual photon and outgoing real photon, respectively. The wave functions are known from QED. The expression is integrated over all transverse sizes of the dipole $R$ and all the longitudinal momenta $z$ of the quark in the pair.

There are several approaches to calculate the dipole cross section since this has not been calculated from first principles. The different predictions assume different compositions of $\sigma_d$ in terms of hard and soft contributions. Some of these approaches for DVCS are summarized here:

- Donanchie and Dosch model [45]: in this model the concept of hard and soft Pomeron is used. Small size dipoles predominantly interact via hard

---

[13]At the small x typical of HERA ($x \lesssim 0.01$).

$\mathbb{P}$ whereas large dipoles interact via soft $\mathbb{P}$. The $\sigma_d$ is calculated in a non-perturbative model and has two free parameters determined by fits to $pp$ and $p\bar{p}$ data.

- Forshaw, Kerley and Shaw [46, 47] calculations for $\sigma_d$ neglected the $z$ dependence for $\sigma_d$ since this has revealed to be small [48]. The only important dependences are on $W^2$ and $R$. The dipole cross section is parametrized in a hard and a soft contributions and fit to diffractive structure function and the total photon-proton cross section data.

- McDermott, Frankfurt, Guzey and Strikman [47, 49] propose a model in which the dependence is not only on $W^2$ and $R$ but also on $Q^2$. The $\sigma_d$ is divided in three terms depending on the size $R$. For small $R$ the cross section is related to the LO gluon distribution. The region of large $R$ is related with the total pion-proton cross section. For medium values of $R$ the cross section is interpolated linearly.

- Favart and Machado [50] have based their approach on the saturation model which interpolates successfully between small and large size configurations. The parameters of the model are obtained from the small $x$ HERA data.

### 1.5.3   DVCS cross section measurements

Measurements of the DVCS cross section are important to model the GPDs and also to help to understand diffraction in QCD. The HERA collider experiments, H1 and ZEUS, have performed the first measurements of the DVCS cross section [1, 2].

The dependence of the DVCS cross section, $\sigma^{(\gamma^\star p \rightarrow \gamma p')}$, on $W$ and $Q^2$ are shown in figure 1.16. The measurements are compared with a GPD-based model [43] and a color-dipole based model [44]. The data sets are in agreement with both descriptions. The $W$ dependence of the cross section shows the steep rise which is typically of hard processes. A fit to the form $W^\delta$ has been performed resulting in $\delta = 0.75 \pm 0.15^{+0.08}_{-0.06}$ ($\delta = 0.77 \pm 0.23 \pm 0.19$) for ZEUS (H1). These $\delta$ values are compatible with the value determined for the $J/\psi$ electroproduction [53]. Also the dependence on $Q^2$ has been studied performing a fit to the form $1/Q^{2n}$. Results obtained by ZEUS are shown in figure 1.17. One of the main uncertainties in the theoretical predictions is the slope $b$ of the $t$-dependence. Measurements of the $t$-dependence have been performed by H1 (see figure 1.17).
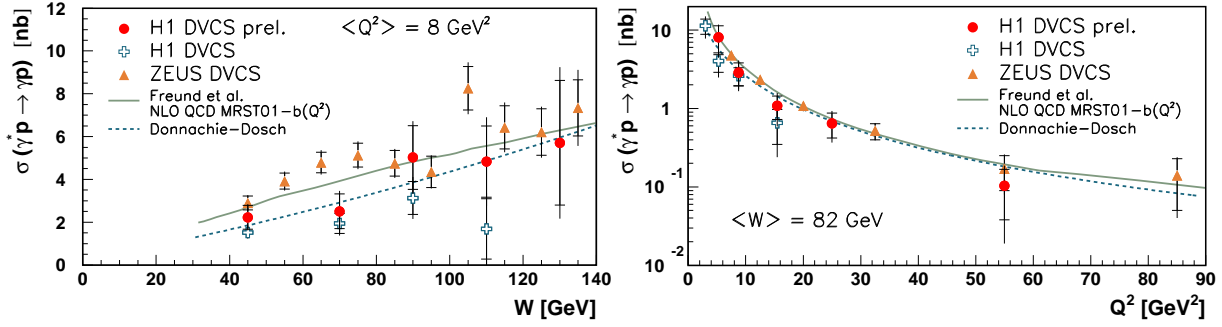
**Figure 1.16:** DVCS cross section as a function of $W$ for $< Q^2 >= 8$ GeV$^2$ (left) and as a function of $Q^2$ for $< W >= 82$ GeV (right) as measured by H1 and ZEUS . Predictions from GPD-based models and color-dipole models are shown.
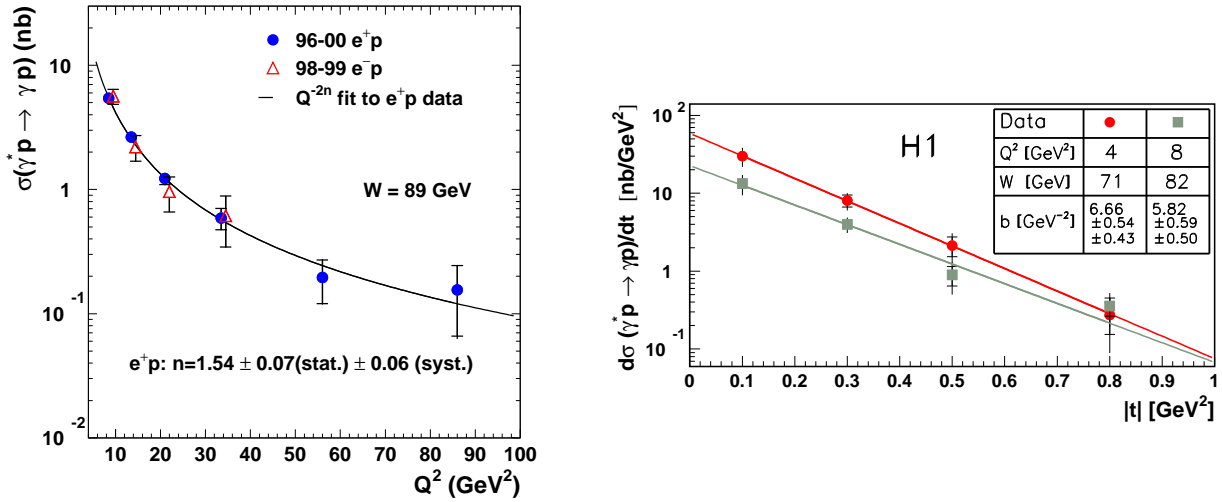


**Figure 1.17:** DVCS cross section as a function of $Q^2$ as measured by ZEUS (left), the solid line is the result of the fit $1/Q^{2n}$. Measurement of the t-dependence of the DVCS cross section by H1 (right). The measured values of $b$ slope are shown.

## 1.5.4   DVCS asymmetry measurements

The definition of different asymmetries allows to exploit all the information contained in the interference term of BH and DVCS processes and hence, a direct access to the GPDs. This section is focussed on the asymmetries defined for unpolarized targets. Definition and characteristics of asymmetries related to polarized targets can be found in [39, 43, 52].

The beam-spin asymmetry $(A_{SL})$ is defined as

$$A_{SL} = \frac{\int_0^\pi d\phi \Delta_{SL}\sigma - \int_\pi^{2\pi} d\phi \Delta_{SL}\sigma}{\int_0^{2\pi} d\phi (d\sigma^\uparrow + d\sigma^\downarrow)}, \qquad (1.37)$$

where $\Delta_{SL}\sigma = d\sigma^{\uparrow} - d\sigma^{\downarrow}$ and $\uparrow$ and $\downarrow$ mean that the lepton is longitudinally polarized along or against its direction.

The beam-charge asymmetry $(A_C)$ is defined as

$$A_C = \frac{\int_{-\pi/2}^{\pi/2} d\phi \Delta_C \sigma - \int_{\pi/2}^{3\pi/2} d\phi \Delta_C \sigma}{\int_0^{2\pi} d\phi (d\sigma^+ + d\sigma^-)}, \tag{1.38}$$

where $\Delta_C \sigma = d\sigma^+ - d\sigma^-$ and the sign $+(-)$ correspond to the cross section for positron (electron) beam.

The azimuthal angle asymmetry (AAA) is defined

$$AAA = \frac{\int_{-\pi/2}^{\pi/2} d\phi (d\sigma - d\sigma^{BH}) - \int_{\pi/2}^{3\pi/2} d\phi (d\sigma - d\sigma^{BH})}{\int_0^{2\pi} d\phi d\sigma}, \tag{1.39}$$

where the $d\sigma^{BH}$ refers to the pure BH contribution. This contribution has to be subtracted since it does not vanish after the $\phi$-integration due to a term $\propto 1/\mathcal{P}_1\mathcal{P}_2$ [43].

Using the equations $1.28 - 30$ to evaluate the asymmetries defined above, only $\sin \phi$ and $\cos \phi$ dependencies remain, hence

$$A_{SL} \propto \frac{1}{c_0^{BH}} s_1^{\mathcal{I}} \sin \phi \propto \sin \phi \, \Im m(M) \tag{1.40}$$

$$A_C \propto \frac{1}{c_0^{BH}} c_1^{\mathcal{I}} \cos \phi \propto \cos \phi \, \Re e(M) \tag{1.41}$$

$$AAA \propto \frac{1}{c_0^{BH}} c_1^{\mathcal{I}} \cos \phi \propto \cos \phi \, \Re e(M) \tag{1.42}$$

where $M$ represent a combination of DVCS amplitudes. As we can see, using the beam-spin and the beam-charge asymmetries, it is possible to have access to the complete DVCS amplitude, real and imaginary part. The $AAA$ and $A_C$ show the same dependence on $\phi$, therefore measurements of these two quantities provide a valuable cross check. The term $M$ corresponds to the following CCF combination

$$M = F_1 \mathcal{H} + \frac{x_B}{2 - x_B}(F_1 + F_2)\tilde{\mathcal{H}} - \frac{t}{4m^2}F_2 \mathcal{E}, \tag{1.43}$$

the dominant term corresponds to the unpolarized CFF $\mathcal{H}$, since $\tilde{\mathcal{H}}$ and $\mathcal{E}$ are suppressed for the typical small values of $x$ and $t$ at HERA. For proton scattering, the GPD $H^u$ gives the main contribution due to the u-quark dominance. The asymmetries explained in this section have predicted to be sizeable in the HERA

kinematic domain. The theoretical predictions for these observables can be found in [43].

The first measurements of DVCS asymmetries have been published by the HERMES [55] and CLAS [3] collaborations at HERA and Jefferson Laboratory, respectively. In figure 1.18 the HERMES results are shown. The left plot shows the measurement of $A_{SL}$[14] as a function of the angle $\phi$ [4]. The pre-
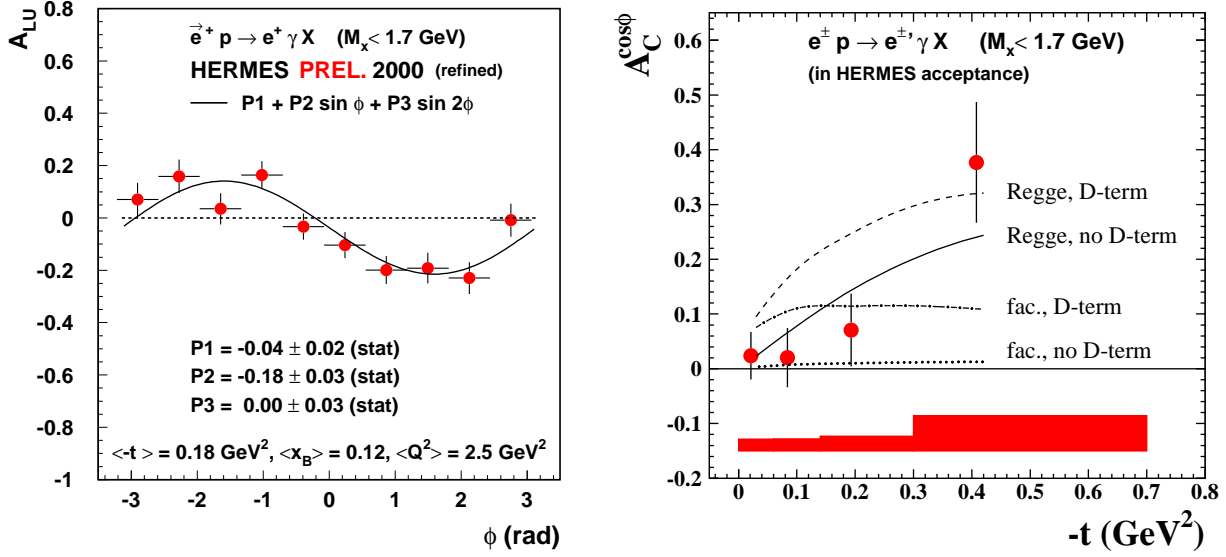


**Figure 1.18:** DVCS asymmetry measurements. Beam-spin asymmetry (left) as a function of $\phi$ shows the expected sinusoidal dependence. Beam-charge asymmetry (right) as a funtion of $-t$ is compared with different theoretical models for the GPDs. Both measurements were performed by HERMES collaboration.

dicted sinusoidal dependence (see 1.40) is clearly seen in the plot. The right plot shows the dependence of the bean charge asymmetry as a function of $-t$ [56]. The experimental data are compared with different theoretical predictions for the GPDs. The GPD models shown use either a factorized t-dependence with (dashed-dotted) or without (dotted) the D-term contribution[15], or a Regge inspired t-dependence with (dashed) or without (solid) the D-term contribution. The data seem to favor to the Regge model and demonstrate the importance of the asymmetry measurements to distinguish between the different GPDs models. A review of other asymmetry measurements can be found [58].

---

[14]Note the different notation for $A_{SL}$ which is labeled in the plot as $A_{LU}$.

[15]This term was added to satisfy the polynomiality condition of the parametrization of the GPDs done by the Double Distribution formalism [57].

# The ZEUS detector at HERA

This chapter provides a brief overview of the HERA accelerator and the ZEUS detector. The components of the detector relevant for this analysis are reviewed in more detail.

## 2.1 The HERA accelerator



**Figure 2.1:** Aerial view of the DESY laboratory in Hamburg. The location of the HERA and PETRA accelerators is indicated by dashed lines.

HERA [59] is the only accelerator in the world which collides electrons or positrons with protons. It is located at the Deutsches Elektronen Synchroton (DESY) laboratory in Hamburg, Germany (see figure 2.1). HERA started to be built in 1984 and is operating since 1992. The HERA tunnel is situated 10-25 meters underground and has a circumference of 6.3 km. Two storage rings, one for the electrons or positrons and one for the protons are situated inside the tunnel.

31

In the electron ring, normal conducting cavities are used in order to accelerate the beam, whereas superconducting cavities are used for the proton beam. The two particle beams are brought to collision in two points along the circumference where the experiments ZEUS and H1 are placed (figure 2.2).
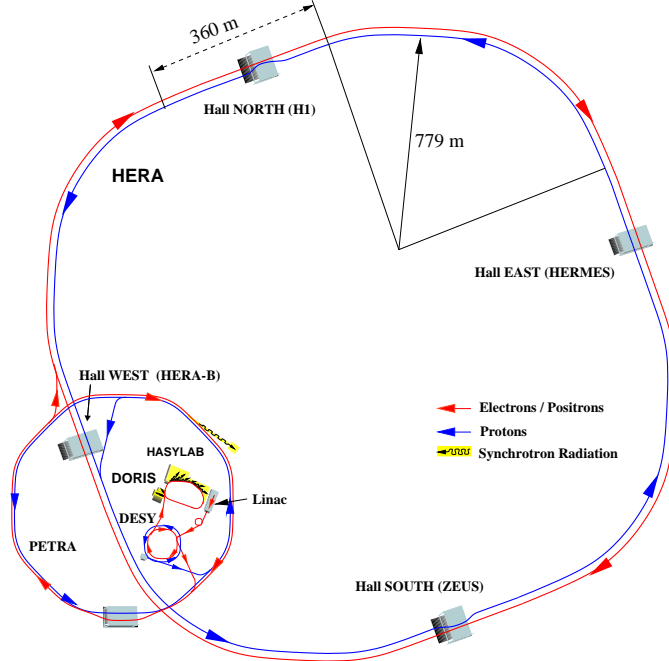


**Figure 2.2:** Schematic view of HERA accelerator.

Two more experiments are using the beams provided by HERA, HERMES and HERA-B, which are fixed-target experiments. HERMES is located in the east area and uses the electron beam to study the spin structure of the nucleon by scattering longitudinally-polarized electrons off polarized gas targets. HERA-B, located in the west area was designed to measure $\mathcal{CP}$-violation in the $B^0\overline{B^0}$-system. The $B$-mesons were produced by means of collisions of the proton beam halo with a wire target. HERA-B stopped taking data in 2003.

HERA started operation accelerating positrons to 27.5 GeV and protons to 820 GeV. The initial configuration changed in 1998 when the positrons were replaced by electrons and the energy of the proton was increased to 920 GeV. One year later, HERA switched back to positron-proton collisions and continued this way until 2000. During this data-taking period, the total luminosity delivered by HERA was 193.24 pb$^{-1}$, including 25.2 pb$^{-1}$ of the electron-proton running period.

At the end of 2000, HERA was shut down for an upgrade [60]. The goals of the upgrade were to achieve a higher specific luminosity and to incorporate the spin rotators that provide longitudinally polarized lepton beams at the interaction points of the H1 and ZEUS experiments. In 2002, HERA started operation again with positron-proton collisions and at the end of 2004 switched to electron-proton collisions and back to positron collisions middle of 2006. The luminosities delivered for the different running periods are shown in figure 2.3.
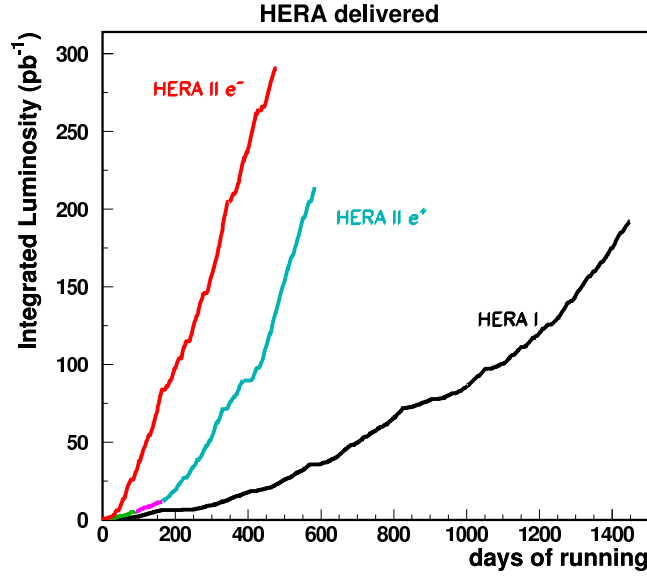


**Figure 2.3:** Luminosities delivered by HERA during 1993-2000 (HERA I) and 2003-2006 (HERA II) [61].

## 2.1.1   Polarized lepton beams

In HERA, the lepton beam becomes naturally transversely polarized through the Solokov-Ternov effect [62]. Electrons moving inside a magnetic field $\vec{B}$ radiate. A small fraction of this emitted radiation causes the spins to flip from parallel to antiparallel to $\vec{B}$ and vice versa. The two spin flip probabilities are slightly different and, therefore, after some time, the beam becomes polarized along the field. The time evolution of the polarization is given by

$$P(t) = P_{ST}(1 - e^{-\frac{t}{\tau}}), \tag{2.1}$$

where $P_{ST}$ is the asymptotic polarization and $\tau$ is the build-up time. These parameters are given by the accelerator design[1].

---

[1]For HERA, $P_{ST} = 0.924$ and $\tau \approx 40$ minutes.

Spin rotators convert the transversely polarized beam to a longitudinally polarized beam. In the actual configuration, there are three pairs of spin rotators installed in HERA, one pair around HERMES and the other two around the H1 and the ZEUS experiment (see figure 2.4).
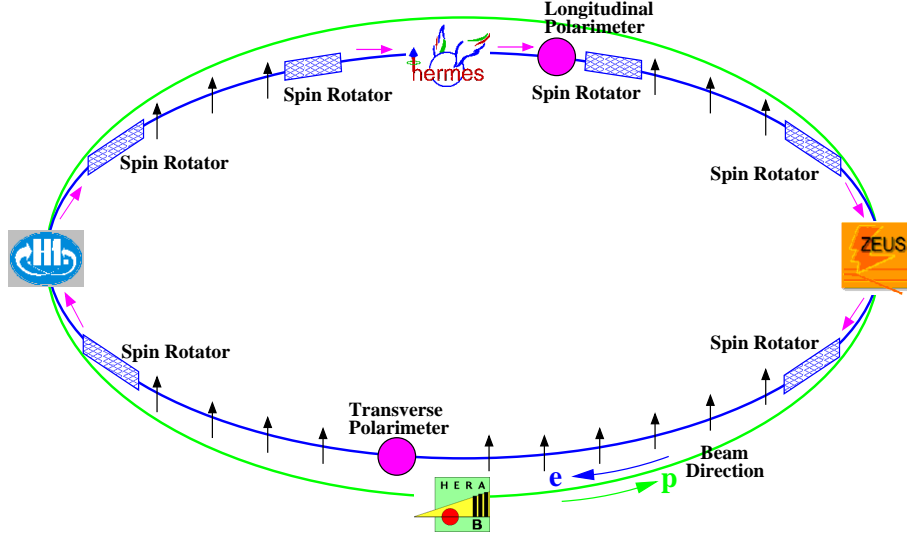


**Figure 2.4:**  Schematic view of the HERA. The location of the spin rotators and polarimeters is shown.

The polarization of the beam is measured using the spin-dependent cross section for Compton scattering of circularly polarized photons off electrons [63]. Two independent polarimeters are used to perform the measurement: the transverse polarimeter (TPOL) [63] and the longitudinal polarimeter (LPOL) [64]. Basically, the polarimeters consist of a laser to produce a linearly polarized photon beam, a Pockels cells to turn this linear light into circularly polarized light which collides with the lepton beam from the accelerator and the backscattered photons are detected by calorimeters. In the TPOL, the transverse polarization is obtained measuring the difference in the mean vertical positions of the scattered photons for left and right circularly polarized light. For the longitudinal polarization measurement, the LPOL uses the asymmetry in the energy of the photons under reversal the laser photon helicities. The uncertainty in the polarization measurement, $\delta P/P$, is 1.6 % using the LPOL and 3.5 % using the TPOL [65].

## 2.2    The ZEUS detector

The ZEUS detector is a general purpose magnetic detector with an almost hermetic coverage designed to study the different processes of lepton-proton scat-

tering at HERA. With a size of $12 \times 11 \times 20$ m$^3$ and a weight 3600 tons, it has been built and operated by a collaboration of more than 400 physicists from 51 institutes in 12 different countries. Since 1992, when ZEUS started operations, several detector upgrades have been carried out as a consequence of the physics and the technical understanding gained during the first years of data taking.

The ZEUS coordinate system is shown in figure 2.5. It is a right-handed orthogonal system with the origin at the nominal interaction point (IP), the $z$-axis pointing in the proton beam direction (defining the forward direction), the $y$-axis pointing up-wards and the $x$-axis pointing horizontally toward the center of HERA. The polar angle of the proton(electron) beam, $\theta$, measured with respect to the $z$-axis, is 0°(180°). The azimuthal angle $\phi$ is measured with respect to the $x$-axis.
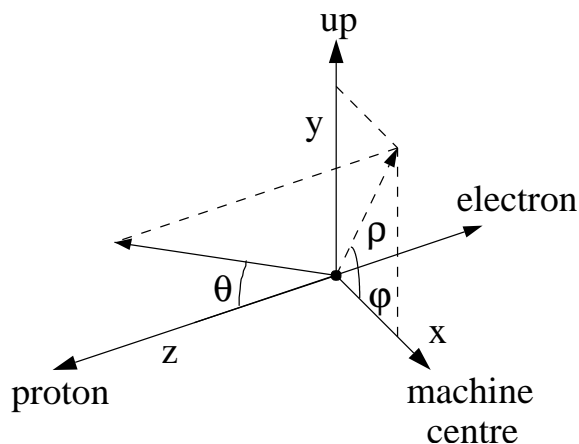


**Figure 2.5:** The ZEUS coordinate system.

Figures 2.6 and 2.7 show the cross section of the ZEUS detector along and perpendicularly to the beam axis, respectively. A brief overview is given below followed by a more detailed description of the detector components relevant for this analysis. For a complete description refer to [66].

In the ZEUS detector, the interaction point is surrounded by the tracking system. The innermost detector is a silicon-strip Micro Vertex Detector (MVD, see section 2.2.5), which was installed during the shutdown of 2001 (until 1996-95 the vertex detector (VTX) was located in its place). The Central Tracking Detector (CTD, see section 2.2.4), a cylindrical proportional wire drift chamber, encloses the beam pipe at the interaction point. It is surrounded by a super-conducting solenoidal magnet providing a field of 1.43 T for the determination
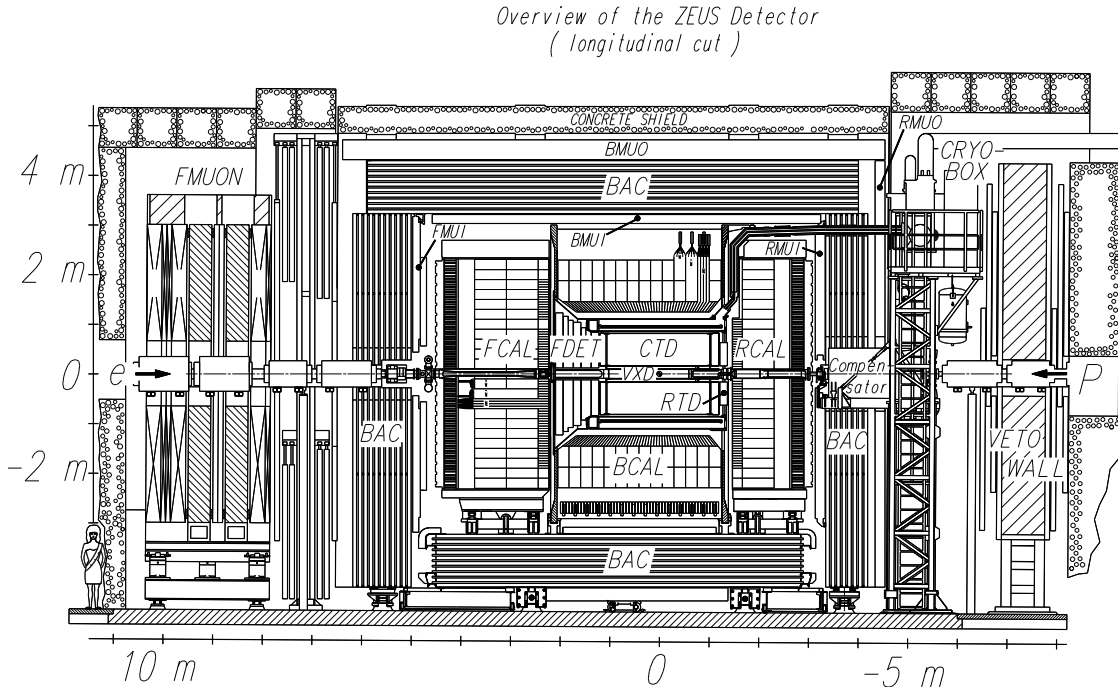
**Figure 2.6:** Cross section of the ZEUS detector along the beam axis.

of the charge and the momentum of charged particles. In the forward and rear directions additional tracking information is provided by the FTD/STT (labeled as FDET in figure 2.6) and RTD chambers respectively. The FTD consists of three sets of planar drift chambers. The STT, which consists of two modules built of straw tube layers, fills the gaps between the three chambers of the FTD. The STT is the replacement of a transition radiation detector system (TRD) which was removed in 2001. The RTD is made of one planar drift chamber with three layers.

Surrounding the tracking system, a compensating high resolution Uranium Calorimeter (CAL, see section 2.2.1) is installed. The calorimeter is the main device to perform energy measurements. It is divided into forward (FCAL), barrel (BCAL) and rear (RCAL) sections. Attached to the front face of the RCAL, the Small-angle Rear Tracking Detector (SRTD, see section 2.2.2) is located. Presampler detectors (FPRES, BPRES, RPRES) are mounted on the front of the calorimeter. These detectors are used to estimate the energy loss by the particles due to interactions with inactive material located in front of the calorimeter. The Hadron-Electron Separator (HES, see section 2.2.3) is installed after three radiation lengths inside the forward and the rear section of the calorimeter. The CAL is surrounded by an iron yoke, which provides a return path for the magnetic field flux and serves as absorber for the Backing Calorimeter (BAC). The BAC
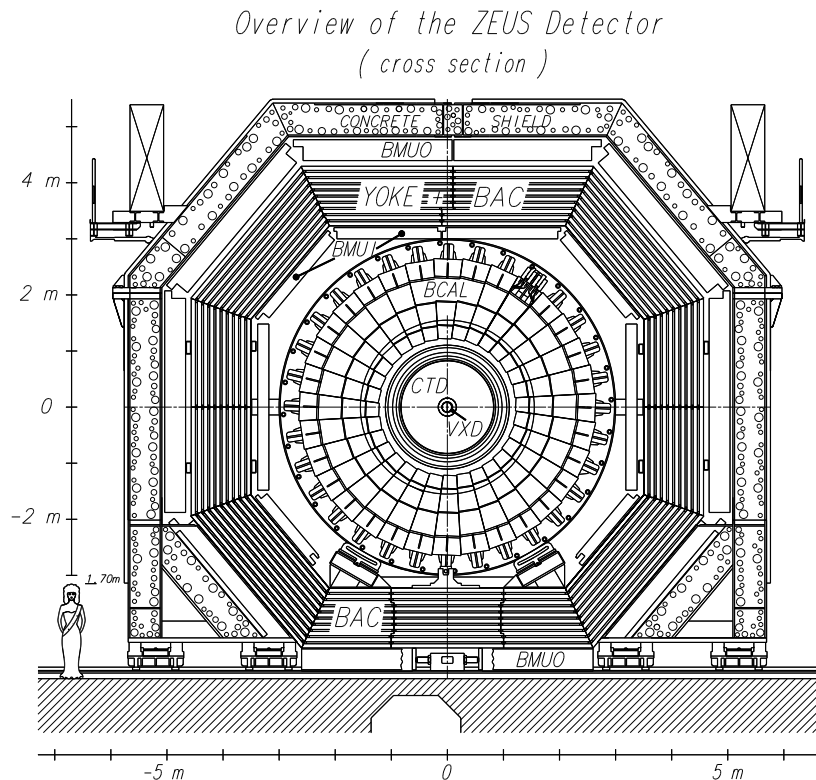
**Figure 2.7:** Cross section of the ZEUS detector perpendicular to the beam axis.

measures the energy leakage from the main calorimeter and acts as a tracking calorimeter for muons. The muon detector systems are placed inside (FMUI, BMUI, RMUI) and outside (FMUON, BMUON, RMUON) the iron yoke.

The VETO wall is a iron-scintillator detector located in the rear part and it is used to reject background from the proton beam-gas interactions. The timing information provided by the VETO wall together with the one given by the C5 counter is also used to reject proton beam-gas events. The C5 counter is placed at the rear end of the calorimeter.

Down the beam pipe, in the rear direction, the luminosity measurement is performed by the Luminosity Monitor (LUMI) and the Spectrometer (SPEC) systems (see section 2.2.6).

## 2.2.1   The Calorimeter (CAL)

The ZEUS calorimeter [67–70] is a high resolution Uranium-Scintillator Calorimeter. It is one of the most essential detectors for the reconstruction of the *ep* scat-

tering final state. The calorimeters are devices which measure the particle energy using the energy of the shower produced by the interaction of the particles with the detector mass.
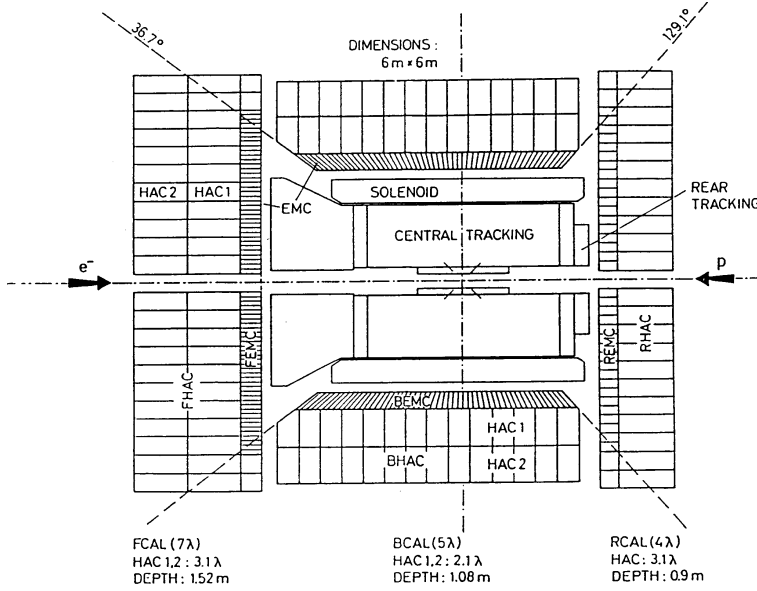


**Figure 2.8:** Schematic view of the CAL.

The CAL is a sampling calorimeter consisting of alternating layers of depleted uranium[2] as absorber medium and organic scintillator as active material. The thickness of the layers is 3.3 mm and 2.6 mm for the uranium and the scintillating material, respectively. These values have been optimized to obtain the same response to electromagnetic and hadronic interacting particles of equal energy. This property, called compensation, was achieved with a factor of $e/h = 1.00 \pm 0.05$.

The energy resolutions of the CAL measured under test beam conditions are, for electrons

$$\frac{\sigma_e}{E} = \frac{18\,\%}{\sqrt{E}} \oplus 2\,\% \tag{2.2}$$

and for hadrons

$$\frac{\sigma_{\mathrm{had}}}{E} = \frac{35\,\%}{\sqrt{E}} \oplus 1\,\% \, . \tag{2.3}$$

with $E$ in GeV.

The calorimeter consists of three parts FCAL, BCAL and RCAL, with different polar-angle coverage as shown in figure 2.8. Also the sections have different

---

[2] $(98.1\,\% \text{ U}^{238}, 1.7\,\% \text{ Nb}, 0.2\,\% \text{ U}^{235})$

|                       | FCAL                      | BCAL                      | RCAL                       |
|-----------------------|---------------------------|---------------------------|----------------------------|
| $\theta$-range        | $2.5°\ -\ 39.9°$          | $36.7°\ -\ 129.1°$        | $128.1°\ -\ 178.4°$        |
| EMC rad. length $X_0$ | 25.9                      | 22.7                      | 25.9                       |
| Interaction length $\lambda$ | 7.14               | 4.92                      | 3.99                       |
| EMC cell dimensions   | $20\ \times\ 5\ cm^2$     | $20\ \times\ 5\ cm^2$     | $20\ \times\ 10\ cm^2$     |
| HAC cell dimensions   | $20\ \times\ 20\ cm^2$    | $20\ \times\ 20\ cm^2$    | $20\ \times\ 20\ cm^2$     |

**Table 2.1:** Basic properties of the three regions of the CAL.

thicknesses. Since the final state particles are boosted to the forward (proton) direction, the FCAL region is the thickest one with $\lambda = 7.14$, followed by the BCAL with $\lambda = 4.92$ and the RCAL with $\lambda = 3.99$, where $\lambda$ is the interaction length. All the sections are divided in modules (see figure 2.9). The FCAL and RCAL have 23 modules each, whereas the BCAL consists of 32 calorimeter modules. Each of these modules is subdivided in towers of $20 \times 20$ cm$^2$, which are segmented longitudinally into an electromagnetic (EMC) and two (only one for the RCAL) hadronic (HAC) sections. The EMC sections are further transversely divided into four cells (only two for the RCAL). The basic properties of the different regions of the CAL are summarized in table 2.2.1.
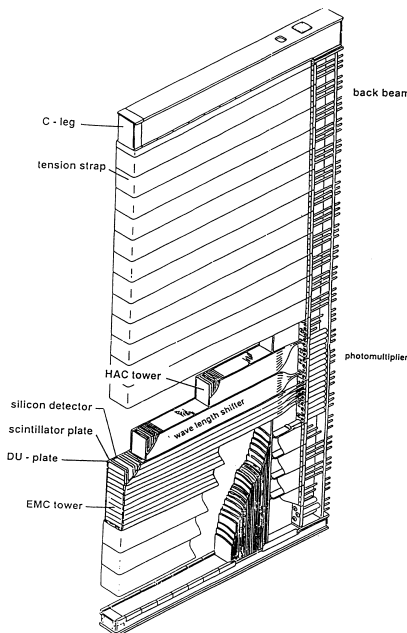


**Figure 2.9:** Layout of a FCAL module.

Each of the calorimeter cells is read out on two opposite sides in $x$ direction by photomultiplier tubes (PMTs), that receive the scintillator light via wave-

length shifters. Using this kind of readout, the energy measurement becomes independent of the impact position within the cell, since the signals of the two PMTs are summed up. The comparison of the amplitude of the two signals allows the determination of the horizontal impact position. The excellent time resolution of the CAL, of the order of 1-2 ns, allows the rejection of background events.

The energy calibration of the CAL was performed using test beam measurements with different particles types of different energies. Continuous monitoring of the calibration is done using the signal from the radioactive decay of the $^{238}$U (half-life $4.5 \cdot 10^9$ years). The PMTs and the readout electronics are additionally calibrated using LED, LASER and test pulses.

### 2.2.2   The Small-angle Rear Tracking Detector (SRTD)

The SRTD [71] was designed to improve the energy and position measurement of the electrons and charged particles around the beam pipe in the RCAL region. It is attached to the front face of the RCAL and covers an area of $68 \times 68$ cm$^2$ (excluding the beam pipe hole). The detector consists of two planes of scintillator strips, each with four quadrants of 24 cm $\times$ 44 cm. The strips are arranged in the $x$ direction in one of the planes and in the $y$ direction in the other (see figure 2.10). The total number of the strips is 272 and they have a width of 1 cm.
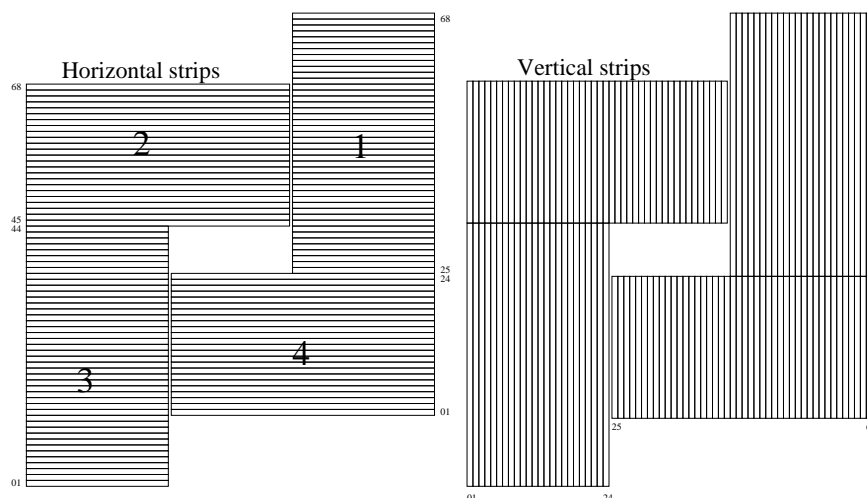


**Figure 2.10:** Orientation and numbering scheme of the strips of the two SRTD planes.

Electrons which lost energy through showers in inactive material in front of the CAL deposit more energy in the SRTD than non-showering electrons. These

energy deposits can be used to correct for this energy loss. Using this method an improvement in the measurement of the electron energy is achieved. For the position measurements, the SRTD provides a resolution of 3 mm. In addition, the fast time measurements provided by the SRTD (resolution of $\sim 2$ ns) are used to reject background events.

### 2.2.3   The Hadron-Electron Separator (HES)

The HES detector [72] consists of two layers of $3 \times 3$ cm$^2$ silicon diodes. One is located in the RCAL (RHES) and one in the FCAL (FHES) at a longitudinal depth of 3.3 radiation length $X_0$ which corresponds to the approximate position of the electromagnetic shower maximum in the CAL. Due to the fact that the hadronic interaction length is 33 times larger than the electromagnetic radiation length, the signals produced by hadrons in the HES are smaller. This provides the possibility to distinguish between electrons and hadrons. The HES provides a spatial resolution of $\sim 9$ mm for single hits. In case of more hits, clusters are formed and the resolution in the particle position improves up to $\sim 5$ mm.

### 2.2.4   The Central Tracking Detector (CTD)

The CTD [73] is a cylindrical drift chamber which measures the direction and momentum of charged particles and the energy loss $dE/dx$, which is used for particle identification. Its active volume ranges from $z = $ -100 cm to $z = 104$ cm. The inner and outer radius are 18.2 cm and 79.4 cm respectively. It covers polar angles of $15° < \theta < 164°$ and has a complete azimuthal angular coverage. The CTD is filled with a mixture of argon, ethane and carbon dioxide in proportions of 82:13:5.

The CTD consists of cells made up of 8 sense wires (see figure 2.11). The wires collect the signals produced by the charged particles which, passing through the gas, ionize the gas molecules along their trajectories and the produced electrons and positive ions drift towards the wires.

The cells are arranged in 9 superlayers (SL). The wires of the odd numbered SLs are parallel to the beam axis, whereas for the even numbered SLs they are inclined by a "stereo" angle of $\sim \pm 5°$ (see figure 2.12). This allows the determination of the $z$ position of the hit with an accuracy of $\sim$ 2 mm. In addition, the 1, 2, 3 SLs are equipped with a $z$-by-timing system which determines the $z$-position using the arrival times at both ends of the CTD. This method is used mainly for trigger purposes.
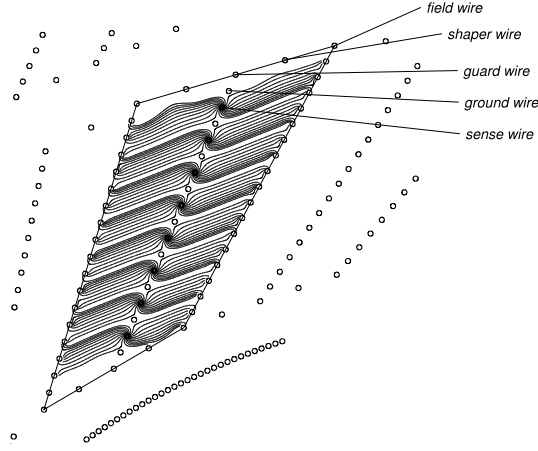
**Figure 2.11:** Layout of a drift cell in the CTD.

The transverse momentum resolution [74] for tracks fitted to the interaction vertex and with $p_\mathrm{T} > 150$ MeV , is given by

$$\frac{\sigma(p_\mathrm{T})}{p_\mathrm{T}} = 0.0058 \cdot p_T \oplus 0.0065 \oplus 0.0014/p_\mathrm{T} \ , \tag{2.4}$$

where $p_\mathrm{T}$ is given in GeV and the symbol $\oplus$ indicates that the three terms are added in quadrature. The first term results from the position resolution, whereas the second and third ones are due to multiple scattering before and inside the CTD, respectively. With the installation of the Micro Vertex Detector (MVD, see section 2.2.5) during the upgrade of the ZEUS detector in 2001, the resolution of the combined CTD+MVD tracking [75] is given by

$$\frac{\sigma(p_\mathrm{T})}{p_\mathrm{T}} = 0.0026 \cdot p_T \oplus 0.0104 \oplus 0.0019/p_\mathrm{T}. \tag{2.5}$$

## 2.2.5   The Micro Vertex Detector (MVD)

The silicon-strip Micro Vertex Detector (MVD) was installed during the shutdown in 2001. Its aim is the improvement of the tracking and vertexing capabilities, in order to increase the acceptance for high-$Q^2$ and heavy flavor physics [76]. The impact of the MVD in the analysis presented in this thesis is limited to the improvements in the tracking reconstruction using CTD+MVD hits, but in the future it might be used as a handle for the proton dissociative background by detecting activity in the forward region.

The physic requirements and the constraints imposed by the available space inside the CTD result in the following design characteristics for the detector:
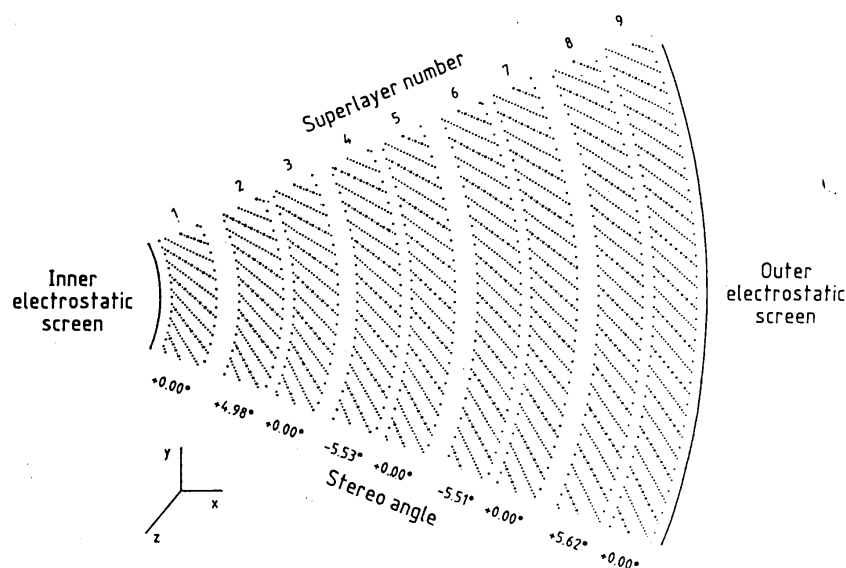
**Figure 2.12:** A $xy$-cross section of one octant of the CTD.

- polar angular coverage of $10° < \theta < 150°$,

- measurement of three points per track, in two projections each

- at least $20\,\mu$m hit resolution,

- two-tracks separation of 200 $\mu$m,

- inner and outer radius limited by the inner volume of the CTD and the beam-pipe volume,

- hit efficiency better than 95%,

- noise occupancy better than $10^{-3}$.

The MVD [77] is divided into two parts, the barrel (BMVD) and foward (FMVD) detectors. The BMVD is surrouding the interaction point and has a length of 64 cm. The FMDV is located next to the barrel region and extends to $z = 72.9$ cm in the forward direction. A schematic view of the MVD is shown in figure 2.13.

The BMVD consists of single sided silicon sensors with dimensions of 64 × 64 mm$^2$ and thickness of 320 $\mu$m. Each sensor has 512 readout strips with a pitch of 120 $\mu$m. The hit position can be measured very precisely comparing the charge fractions between two readout strips. The split of the charge is done via capacitive division. The single hit resolution determined during test beam measurements is
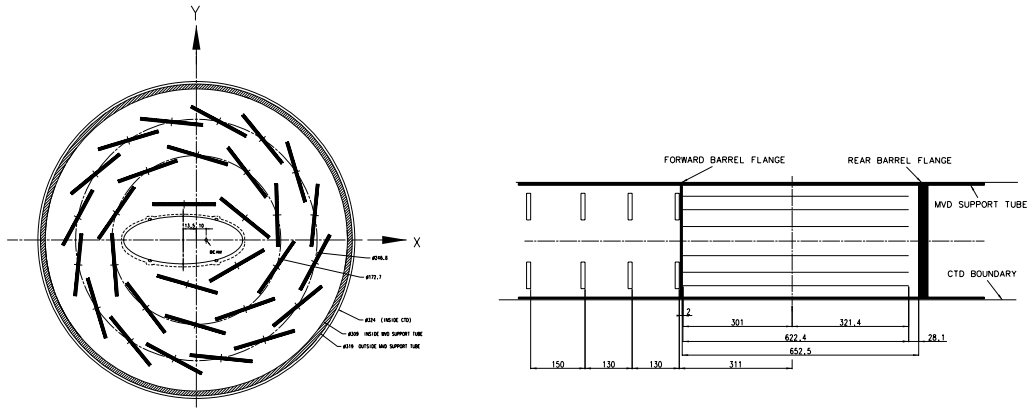
**Figure 2.13:** Layout of the MVD in the xy-view (left) and along the beam direction (right).

120 $\mu$m. The sensors are arranged in double sided modules which are mounted in three concentric Al layers around the interaction point. The inner layer is not complete due to the elliptical shape of the beam pipe.

The forward section consists of four wheels which are made of two layers of 14 silicon sensors. Unlike the barrel sensors, the FMVD ones have a trapezoidal shape. In each of the wheels, the two layers are parallel but the strips are tilted by 180°/14 in opposite directions.

## 2.2.6   The luminosity measurement

The event rate $\mathcal{R}$ for a given process with a cross section $\sigma$ is related to the luminosity $\mathcal{L}$ by

$$\mathcal{R} = \mathcal{L} \cdot \sigma \tag{2.6}$$

Therefore, an accurate measurement of the luminosity is crucial for the extraction of any cross section. The values of the luminosity can be calculated either from the beam parameters or using a well known and precisely calculable process and applying Eq. 2.6.

In ZEUS, the $\mathcal{L}$ determination is done using bremsstrahlung events $ep \rightarrow e\gamma p$. The main reasons to choose this process were that it has a large cross section which is also well known from the theory. In addition, the process has a clean experimental signature: the coincidence of an electron and a photon at small angles with respect to the lepton beam direction, with energies that add up to the initial electron energy. The luminosity measurement is performed by two systems: the Luminosity Monitor (LUMI) and the Spectrometer (SPEC). The LUMI has
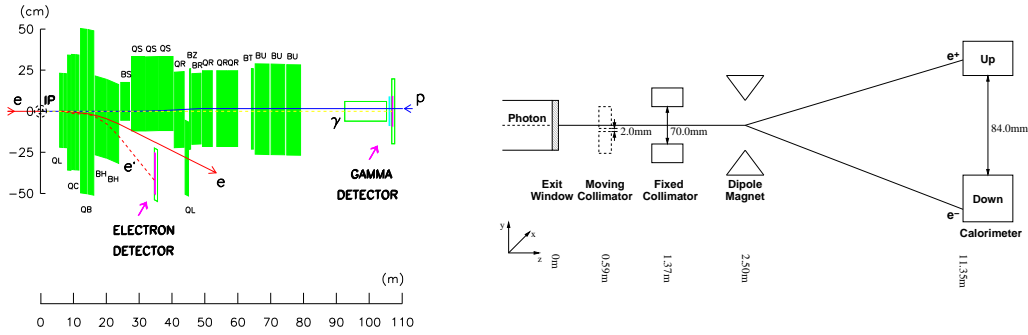
**Figure 2.14:** Schematic view of the LUMI (left) and the SPEC (right).

been used since the beginning of the data taking, whereas the SPEC was designed for the new scenario after the HERA upgrade in 2001, in which the increase of the synchrotron radiation and the high probability of bremsstrahlung photons in each bunch crossing posed new challenges to the luminosity measurement. The LUMI system has also been improved in order to adapt it to the new conditions.

In the LUMI system, the measurement is based on counting the rate of bremsstrahlung photons. The detector is located downstream of the lepton beam (see figure 2.14). The bremsstrahlung photons leave the beam pipe through a Cu-Be window of a thickness of $0.0095X_0$ which is situated at $z = $ -92.5 m and they are detected by a lead-scintillator sampling calorimeter at $z = $ -107 m. The energy resolution of the calorimeter is $\sigma(E)/E = 23\%/\sqrt{E}$. The measurement of the photon rate is corrected for the background coming from the bremsstrahlung of leptons with the residual gas in the beam pipe. The precision of the luminosity measurement is 1.5-2.2%. The largest uncertainty comes from the acceptance of the photon calorimeter. A more detailed description of the LUMI can be found in [78].

The measurements in the SPEC [79] are also based on counting the rate of bremsstrahlung photons, but unlike in the LUMI system, there is not a direct measurement of them, but in this case the photons are detected through their pair conversion, $\gamma \to e^+ e^-$, in the material of the exit window. The window of the SPEC is located 92 m from the nominal interaction point. Approximately 10% of the photons convert into a pair. This fraction of converted photons is uniform over the surface of the window. The converted pairs, after transversing the collimators, are split vertically by a magnetic dipole. Finally the electrons and positrons are detected by a segmented tungsten-scintillator sampling calorimeter. A schematic layout of the SPEC is shown in figure 2.14. With the 2004 data collected by

ZEUS, the estimated error for the luminosity measurement was 3.5%, however it is expected to decrease down to ~2% with a better understanding of the detector.

### 2.2.7   Trigger and data acquisition

The HERA accelerator delivers a bunch crossing rate of 10.4 MHz. This rate is dominated by beam-gas interactions, which contribute about $\sim$ 10-100 kHz. In contrast, the rate of interesting $ep$ events is several orders of magnitude smaller (e.g. for NC DIS events, with $Q^2 > 100$ GeV$^2$ , the rate[3] is about 0.1 Hz).

In order to select the interesting events, the ZEUS experiment has a three-level, pipe-lined trigger system [66, 80] which achieves the necessary rate reduction together with a high efficiency in selecting the physics events. A schematic view of the trigger is shown in figure 2.15.

The First Level Trigger (FLT) is a hardware trigger which reduces the output rate below 1 kHz. The central components of the ZEUS detector have their own FLT electronics and produce their own trigger decision based on raw quantities. These decisions are taken within $\sim 2\mu$s after a bunch crossing and then they are sent to the Global First Level Trigger (GFLT). Within $\sim 4\mu$s, the GFLT decides whether the event should be passed onto the next trigger level.

The Second Level Trigger (SLT) is based on a transputer network. It is designed to reduce the rate to 50-100 Hz. The different components of the SLT send the information to the Global Second Level Trigger (GSLT). The time for the GSLT to take a decision is longer than at the FLT, because the algorithms are more complex and allow the finding of calorimeter clusters, tracking and vertex variables which open the possibility for trigger decisions based on event topologies. If the event is accepted, the complete information is sent to the Event Builder (EVB), which creates the final data format ready to be used for the last level.

The Third Level Trigger (TLT) is a software trigger running on a computer farm. At this stage, the events can be fully reconstructed using algorithms very similar to the ones existing in the offline code. Calculations of the kinematic variables, electron, muon and jet finders are available at the TLT. The events are accepted and classified using different filters which are designed according to the physics to be studied. The final output rate at the TLT is $\sim$ 1-5 Hz. In the last step, the selected events are written to tape at the DESY computer center and are available for the offline reconstruction and analysis.

---

[3]For an instantaneous luminosity of $2 \cdot 10^{31}$cm$^{-2}$s$^{-1}$.
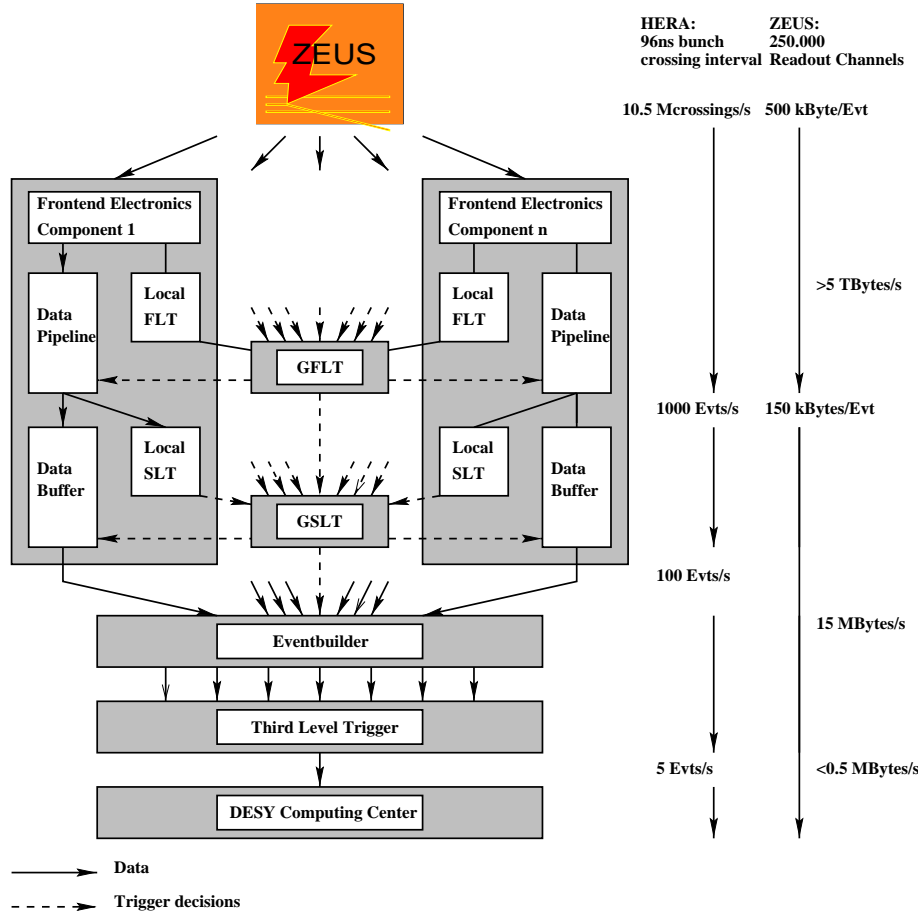
**Figure 2.15:** The ZEUS trigger and data acquisition system.

# Event simulation

Important parts of high energy experiments are the simulation programs. The extraction of many physics observables relies on simulations. From the experimental point of view, the simulation allows to study detector responses, resolution of the physics variables and acceptance corrections due to the geometrical limits of the detectors. Moreover, it is also used to design some details of the physics analysis like the criteria to filter the interesting events. Another task of the simulation techniques is related to the theoretical predictions. Due to the complexity of the high energy processes, some aspects[1] need to be treated with phenomenological models implemented through simulation. Therefore, the comparison of the simulation with the real measurements is used to test different theoretical approaches.

In this chapter, a brief description of the simulation of the $ep$ collisions at ZEUS is given followed by a description of the different Monte Carlo (MC) generators used in this analysis.

## 3.1 Physic and detector simulation at ZEUS

In a very simplified way, we can say that the general structure of the simulation can be divided in two steps: event generation and detector simulation.

The simulation of $ep$ processes starts with the event generation performed by MC generators. The MC generators produce random events following the statistical distributions deduced from the cross section of a given process. The usual output contains the 4-momenta of the initial and final particles produced as well as kinematic variables.

In the second step, the generated events are passed to the full simulation of the ZEUS detector, MOZART. Here, the information about the geometry and

---

[1]Large distances process, i.e. hadronization which can not be calculated within pQCD.

materials for the different components of ZEUS is contained. MOZART is based on the GEANT [81] package. The output of MOZART is given to ZGANA which carries out the simulation of the trigger. In the last stage, the events are reconstructed with the same package that is used for the real data, ZEPHYR.

The different steps of the simulation are in continuous development and periodically new versions are released. All the simulation chain is running on a large amount of UNIX machines distributed in different countries. Since the start up of HERA II and due to the increasing demands of computing power, the MC production is also running on the GRID.

## 3.2 MC used in the analysis

### 3.2.1 DVCS simulation: GenDVCS

The signal events for Deeply Virtual Compton Scattering were generated using GenDVCS [82]. It is based on FFS model (see section 1.5.2) and generates only elastic DVCS. The 4-momenta of the final particles are generated using the cross section formula (1.33). For the $F_2$ structure function, the parametrization ALLM97 [83] is used. The scattered proton is generated according to

$$\frac{d\sigma_{DVCS}^{ep}}{dt} \propto e^{-b|t|} \tag{3.1}$$

For the samples of GenDVCS used in this analysis, the value of the parameter $b$ was set to 6 GeV$^{-2}$ which has been chosen in accordance with the value measured by the H1 collaboration [2].

GenDVCS was interfaced with the MC generator HERACLES [84] to take into account the effects of QED radiative processes. The first order QED corrections to the Born level are shown in figure 3.1: initial state radiation, final state radiation and virtual loop corrections. These corrections can produce changes in the cross section and shifts in the measured kinematic variables with respect to the true values, hence the importance of being included in the simulation.

### 3.2.2 Bethe-Heitler simulation: GRAPE-Compton

The Bethe-Heitler processes $ep \to e'\gamma p'$ for the elastic case and $ep \to e'\gamma X$ for the inelastic case, were generated using GRAPE-Compton [85]. The cross-section calculation ares based on exact matrix elements in the electroweak theory at the
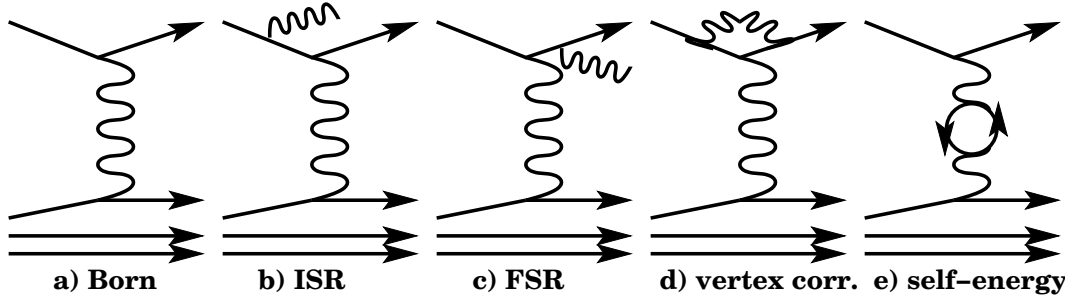
**Figure 3.1:** Diagrams showing LO QED correction to the Born level.

tree level. Radiative corrections to the incoming and outgoing electron are also included.

The processes are classified in three categories:

- elastic: $M_{had} = M_p$

- quasi-elastic[2]: $|t| < t_{min}$ or $M_p + M_{\pi^0} < M_{had} < 5$ GeV

- DIS: $|t| > t_{min}$ and $M_{had} > 5 GeV$

where $M_{had}$, $M_p$ and $M_{\pi^0}$ are the masses of the hadronic system, the proton and the neutral pion, respectively. $t$ is the squared momentum transfer at the proton vertex, $t_{min}$ is set[3] to $\sim 1 GeV^2$ .

For the elastic processes the calculations are done using the dipole form factor for the proton-proton photon vertex. For the inelastic process, the electromagnetic proton structure functions are used with the parametrization of Brasse *et al.* [86] for $M_{had} < 2$ GeV and the ALLM97 [83] parametrization for $M_{had} > 2 GeV$ . The MC generator SOPHIA [87] is used to generate the hadronic final state. In the DIS region the program library PDFLIB [88] is used to obtain the parton density functions with $|t|$ as the QCD scale and PYTHIA [89] for the hadronization process.

### 3.2.3   Dilepton simulation: GRAPE-Dilepton

The dilepton-production, $ep \rightarrow e'e^+e^-p$, can contribute to the background of the Bethe-Heitler process. To simulate this process the GRAPE-Dilepton [85]

---

[2]Quasi-elastic process will be referred as inelastic.
[3]The exact value depends on the set of PDFs used.

generator was used. The contributing Feynman diagrams are the 2-$\gamma$ (which is the dominant in most of the phase space), $\gamma Z^0$, $Z^0 Z^0$ process and the photon conversion into the lepton pair. Interference of the final states $e^{\pm}$ are taken into account for the di-$e$ channel. ISR and FSR can also be include. For this analysis, samples of elastic and inelastic di-$e$ production were used.

### 3.2.4  Vector Meson simulation: ZEUSVM

ZEUSVM [90] is a MC program to simulate the elastic production of VM (see figure 3.2). The diffractive electroproduction of vector mesons, such as $J/\psi$, $\omega$, $\rho$ and $\phi$, were considered as potential sources of background. Thus, ZEUSVM was used to simulated those processes.
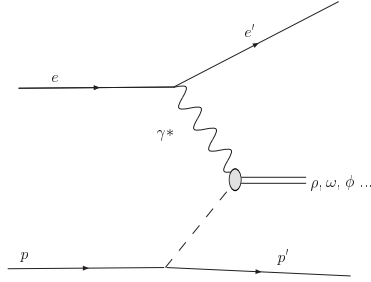


**Figure 3.2:** Schematic diagram of the processes generated by ZEUSVM.

The program generates the event kinematics using the following parametrization of the cross section:

$$\sigma^{ep \to e'Vp'}(Q^2, W) \propto \frac{W^{\delta}}{(M_V^2 + Q^2)^n}, \tag{3.2}$$

where $\delta$ and $n$ are parameters and $M_V$ is the mass of the vector meson. The 4-momenta of the scattered proton are generated according to the exponential function:

$$\frac{d\sigma^{ep \to e'Vp'}}{dt} \propto e^{-b|t|} \tag{3.3}$$

The values of the parameters $\delta, n$ and $b$ are set during the generation procedure from a fit of the resulting cross section to the diffractive VM data. The angular distributions of the decay products of the vector mesons in the helicity frame [91] are generated uniform. After generation the distribution are reweighted following a formula based on the $s$-channel helicity conservation hypothesis. Radiative corrections are calculated with HERACLES.

### 3.2.5 Summary of the MC samples

| MC Generator | Process | Events | $\mathcal{L}(\mathrm{pb}^{-1})$ |
|---|---|---|---|
| GenDVCS | elastic DVCS (e$^+$p) | $640k$ | 1444.7 |
| | elastic DVCS (e$^-$p) | $640k$ | 1444.7 |
| GRAPE-Compton | elastic BH (e$^-$p) | $480k$ | 277.7 |
| | elastic BH (e$^+$p) | $240k$ | 138.9 |
| | inelastic BH (e$^-$p) | $480k$ | 380.3 |
| | inelastic BH (e$^+$p) | $240k$ | 190.2 |
| GRAPE-Dilepton | $e^+ p \rightarrow e'e^+e^- p'$ | $80k$ | 707.9 |
| | $e^+ p \rightarrow e'e^+e^- X$ | $80k$ | 2687.3 |
| ZEUSVM | $\rho(\rightarrow \pi^+\pi^-)$ | $600k$ | 32.6 |
| | $\omega(\rightarrow \pi^0\gamma)$ | $168k$ | 5972.5 |
| | $\phi(\rightarrow K_L^0 K_S^0)$ | $192k$ | 289.1 |

**Table 3.1:** Summary of the main MC sample used in the analysis.

# ZEUS event reconstruction

The events stored on tape after the trigger selection described in section 2.2.7 are further reconstructed with the ZEUS reconstruction package. The information of the individual components of the detector is processed and combined in order to produce a complete event data set. This high level information, which is mainly made up of tracks and calorimeter deposits, is used to identify different kinds of particles, for example electrons and muons, as well as objects like jets.

The experimental signature of the exclusive production of a real photon in the ZEUS detector is a scattered electron and a real photon. The scattered proton, which escapes downstream in the beam pipe, is not detected. In this chapter, the reconstruction of the main quantities which are used to perform the selection and analysis of the this event topology is described.

## 4.1   Calorimeter reconstruction

The basic calorimeter information is the energy deposited in each of the cells which must be corrected to account for different experimental effects. Deposits in the calorimeter not coming from $ep$ interactions are classified as noise. There is a variety of noise sources: signals coming from the natural radioactivity of the uranium, bad operation of the PMTs and problems with the read-out electronics. The cells affected by noise are rejected with different criteria:

- Standard noise suppression cut: $E_{cell}^{EMC} < 60$ MeV, $E_{cell}^{HAC0} < 100$ MeV and $E_{cell}^{HAC} < 100$ MeV. If the cells are isolated, the threshold is 80 (140) MeV for the EMC (HAC) sections.

- Imbalance cut: $|E_{left} - E_{right}|/E_{cell} > 0.7$ where $E_{left}$ and $E_{right}$ are the signals coming from the two PMTs of the cell. The cut is only applied to cells with energy above 1 GeV.

- Noisy cell list[1]: list for different time periods which contains cells identified as noisy after quality and monitoring checks.

The calorimeter energy scale is corrected using the factors summarized in table 4.1. The method to calculate these factors is described in [92].

| CAL region | Cell type | Correction factor |
|:---:|:---:|:---:|
| RCAL | EMC | +2.2% |
|  | HAC | +2.2% |
| BCAL | EMC | +5.3% |
|  | HAC | +9.6% |
| FCAL | EMC | +2.4% |
|  | HAC | −5.9% |

**Table 4.1:** Energy correction factors applied to individual cells of the CAL.

After the treatment described above, global calorimeter variables are calculated. The total energy deposited in the CAL, $E_{tot}$, and its projections $p_x, p_y, p_z$ along the ZEUS coordinate system are defined as

$$E_{tot} = \sum_i E_i, \tag{4.1}$$

$$p_x = \sum_i E_i \sin \theta_i \cos \phi_i, \tag{4.2}$$

$$p_y = \sum_i E_i \sin \theta_i \sin \phi_i, \tag{4.3}$$

$$p_z = \sum_i E_i \cos \theta_i, \tag{4.4}$$

where the index $i$ runs over all calorimeter cells. $E_i$, $\theta_i$ and $\phi_i$ are the energy, polar and azimuthal angles for the $i-th$ cell, respectively. An important variable is the conserved quantity

$$E - p_z = \sum_i (E - p_z)_i = \sum_f (E - p_z)_f, \tag{4.5}$$

where the index $i$ and $f$ run over the initial and final particles, respectively. For a $ep$ interaction in which all particles are detected $E - p_z = 2E_e$. Particles

---

[1]Not done in the MC simulation.

which escape down to the forward beam pipe (mainly associated with the proton-remnant) give a negligible contribution to the sum since for them, $E - p_z \approx 0$. Photoproduction and DIS events have different $E - p_z$ distributions, therefore this variable is a useful tool to discriminate between processes.

Particles detected by the CAL will deposit their energy in several adjacent cells. The next step in the CAL reconstruction is the clustering of the cells to form objects that can be later identified as particles. There are different levels of clustering. A geometrical cluster composed of neighboring cells is referred to as *island*. In figure 4.1, a schematic view of the algorithm is shown. Cells must be connected around a local maximum which is the cell with the highest energy value. The *islands* are used as input to perform a clustering in the $\theta - \phi$ space resulting in the so-called *cone islands*. Information coming from other detectors, such as tracks, can be combined with these calorimeter objects to develop more sophisticated algorithms.
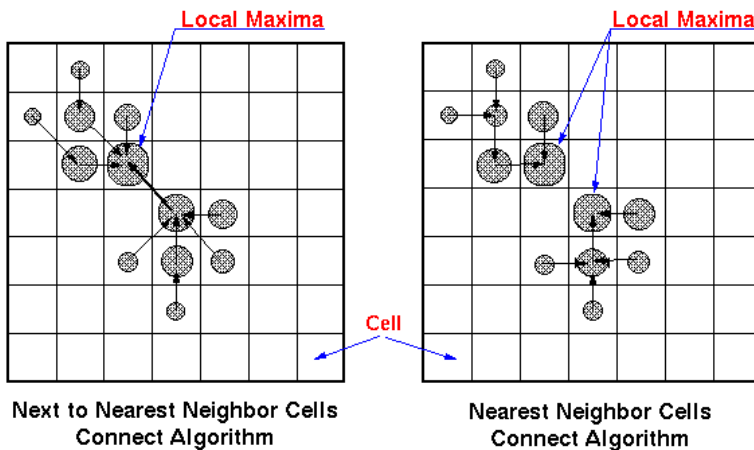


**Figure 4.1:** Schematic representation of the cell to island clustering.

## 4.2   Track and vertex reconstruction

The CTD and MVD are the main tracking devices (see sections 2.2.4 and 2.2.5). Their information is used to obtain tracks which are the reconstructed trajectories from charged particles. The relevant variables of the tracks are the momentum, the charge and the energy loss. Once the tracks are reconstructed they are used for the vertex finding.

The basic steps[2] to obtain a track are the pattern recognition and the track fit. In the pattern recognition, measured hits are assigned to a track candidates. During the fit phase, the hits belonging to a track candidates are fitted to obtain the trajectory of the track. The tracks are fitted using a helix parametrization. Three modes are available for the reconstruction:

**CTD-only :** only CTD information is used. The search of the track candidates starts with a group of hits (segments), from the outermost superlayer to the inner ones. After this the fit is performed.

**Regular :** joint information from CTD and MVD is used. MVD hits are combined in segments and compared to CTD segments, if they are compatible, a track candidate is formed. MVD segments which are not compatible are also kept as MVD stand alone tracks.

**ZTT :** this mode uses the CTD+MVD tracks as input for a re-fitting procedure based on Kalmam filter techniques [75].

The regular mode has been chosen for this analysis. Using MC simulations, the resolutions of the track reconstruction for the CTD-only and regular mode have been studied [75]. In figure 4.2 the resolution as a function of the transverse momentum of the track, $p_T^{track}$, is shown. A considerable improvement using the MVD information is seen for high $p_T^{track}$ tracks.

Reconstructed tracks are used to find the vertex of the interaction. Tracks that are compatible with the beam-line are fitted until a vertex position is found. The tracks are refitted to the found vertex and are denoted vertex fitted tracks. Secondary vertices are also found using the tracks that have not been fitted to the primary vertex.

The extraction of angular and kinematic variables depends on the vertex position. Hence it is important to have an accurate measurement of the vertex together with a good description of the vertex distribution by the MC simulation. The real vertex distribution has been measured using a minimum bias sample [94] and the MC samples have been reweighted to match the measured distribution.

Figure 4.3 shows a comparison of the $z_{vtx}$ position between data and MC. The data (dots) corresponds to $e^-p$ e-sample selection (see section 5.1). The MC histogram is normalized to the number of events in the data sample. The shoulder located around $\sim +70$ cm corresponds to interactions produced in the satellite bunches. A good description of the vertex distribution is observed.

---

[2]The track reconstruction is performed by the VCTRACK [93] package.
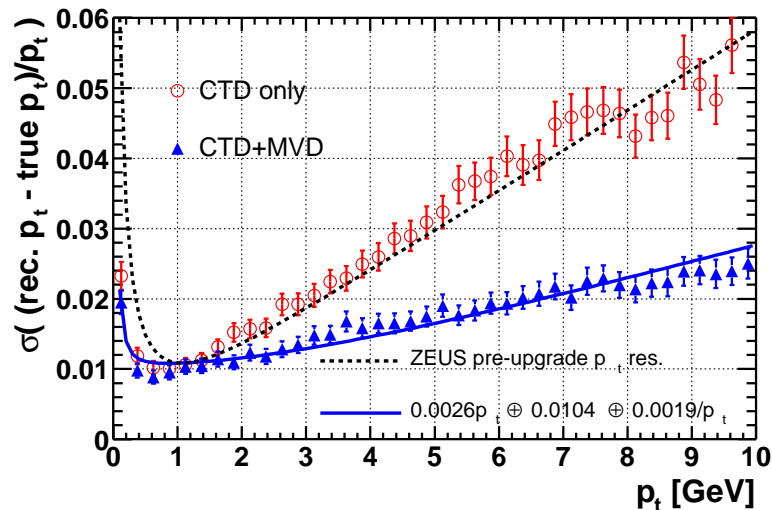
**Figure 4.2:** Resolution of the track reconstruction as a function of $p_T^{track}$. Plot taken from [75].
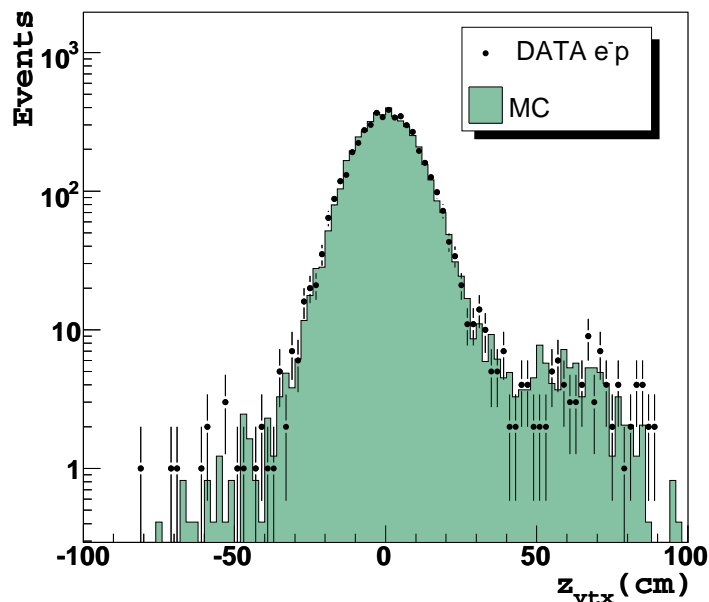


**Figure 4.3:** Distribution of the $Z$ component of the vertex for data and MC.

## 4.3 Particle identification and reconstruction

At the beginning of the chapter it has been mentioned that the basic event topology corresponds to a scattered electron and a real photon. The selection of this kind of events needs to distinguish the deposits belonging to electrons and pho-

tons from the ones coming from other particles. For this purpose the electron finder SINISTRA [95] has been used.

SINISTRA is a neural network which analyzes the islands in the whole calorimeter and returns a number which is interpreted as the probability of each cluster to be an electron. Electrons and photons mainly leave all their energy in the electromagnetic part of the calorimeter, however there are other particles, such as pions, that leave the same signal in the CAL. The key for the distinction between electrons and pions is the study of their shower profiles, which are different. Photon shower profiles are very similar to electron ones, so SINISTRA can be used to identify photons as well.
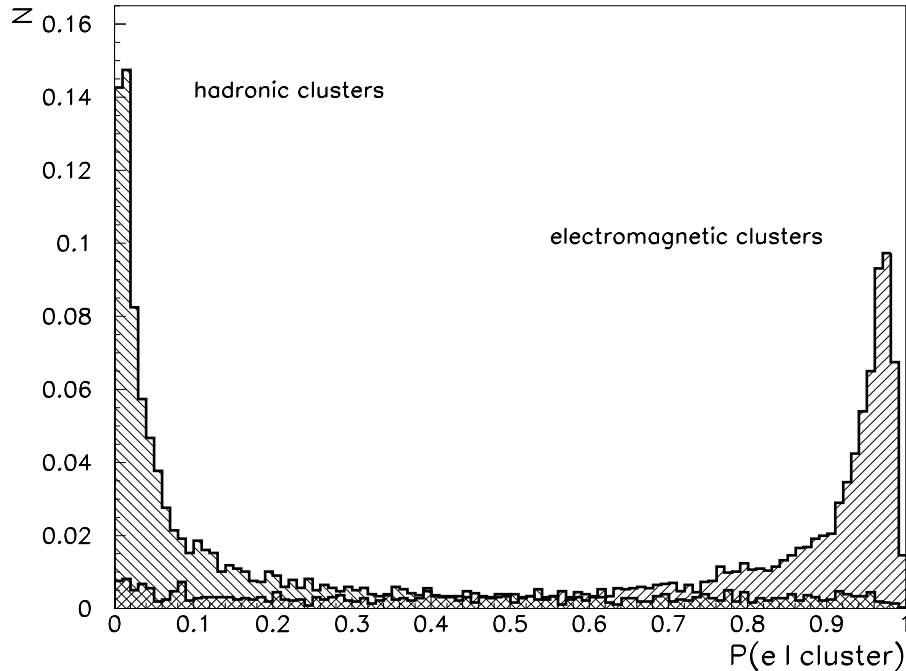


**Figure 4.4:** Probability distribution for a given cluster to be an electromagnetic cluster using the SINISTRA electron finder [95].

The neural network was trained with a MC sample of 4000 events and after that a pattern for the probability was produced. The results showed that electrons should have a probability close to one whereas the hadronic clusters will have probability close to 0 (see figure 4.4). The candidates found by the electron finder are ordered in descending probability and, since for this analysis the identification of photons is also needed, no track information has to be required. Studies on the performance of SINISTRA [96] have shown that the efficiencies for finding the scattered electron are above 95%.

A complete set of variables is calculated for each of the candidates. These

have associated basic quantities as their energy, position and tracking related variables and also more specific quantities like the number of cell associated or shower shape variables. Although SINISTRA uses only CAL information to identify the particles, the track information is combined with the candidates afterwards. Briefly, a match between the tracks available in the events and the candidates is performed. Tracks are extrapolated to the surface of the CAL and associated to the candidate when the distance of closest approach[3] (DCA) is less than 20 cm.

## 4.3.1    Position and energy reconstruction

The energy of the candidates provided by the electron finder is obtained by summing all the energies deposited on the cells that have been tagged as belonging to the candidates. These energies are used later for the event selection and also, to reconstruct the event kinematics (see section 4.4). Crucial cuts for the selection of events depend directly on them (i.e. $E - p_z$, $E'_e$ or $E_\gamma$). Thus, it is very important to have agreement between data and MC simulations.

The measurement of the energy is affected by different factors that produce mismatches between data and MC simulation. These effects are mainly due to an inaccurate description of the dead material in the detector. Other effects, such as an energy scale mismatch or different energy resolution in data and MC are also present. Therefore, the measurements should be corrected for these effects.

In figure 4.5 (left), the distribution of $E - p_z$, which have been calculated as

$$E - p_z = (E - p_z)_{scattered\ e} + (E - p_z)_\gamma, \tag{4.6}$$

is shown. As one can observed the peak positions are shifted from the nominal value ($E - p_z \approx 55 GeV$). This deviation is due to the energy loss by the particles in their interactions with the dead material in the detector.

During the HERA II running period, the amount of dead material (see figure 4.6) has considerably increased due to the installation of new components, mainly the MVD. The MC simulation of this material is limited due to its complexity.

There are different methods to obtain the corrections needed for the energy measurements. The method used in this analysis is based on kinematic peak events and the corrections are calculated by comparing double-angle quantities

---

[3]The distance of closest approach is defined as the shortest distance between the extrapolated track and the cluster.
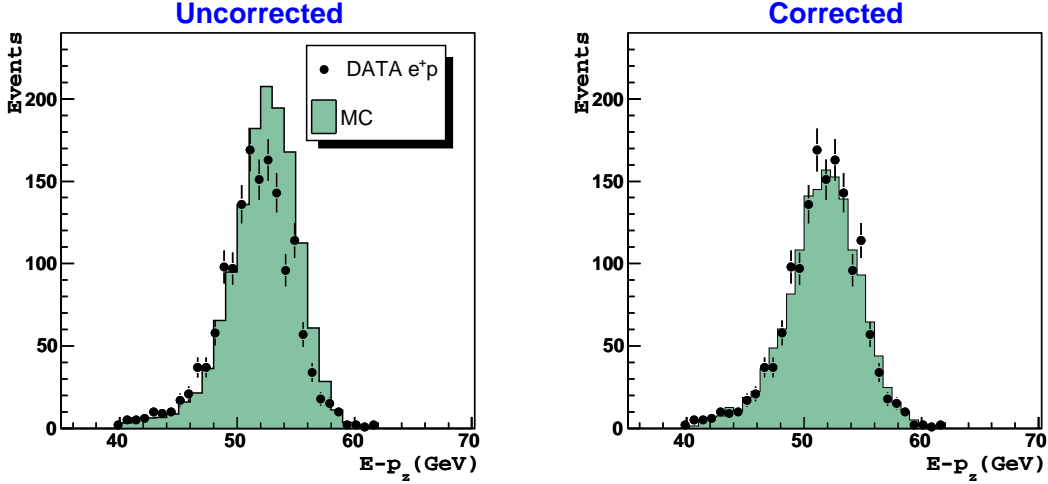
**Figure 4.5:** Uncorrected and corrected $E - p_z$ distribution for $e^+ p$ data and MC for e-sample candidates (see section 5.1). MC histograms are normalized to the data.
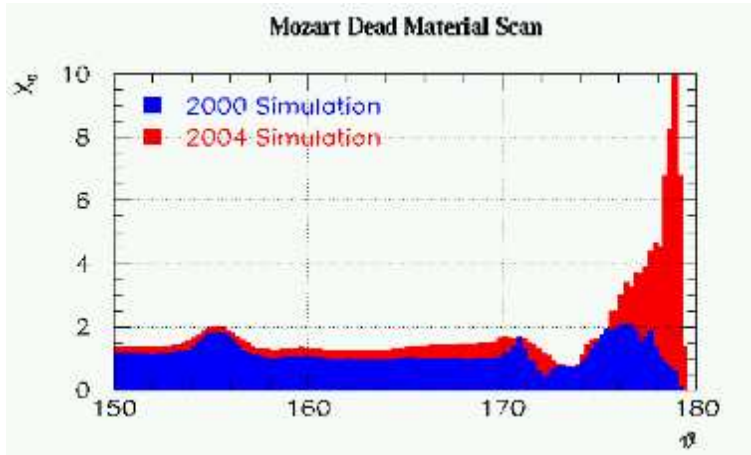


**Figure 4.6:** Map of the MC dead material distribution as a function of $\theta$ for the RCAL region. An increase is observed for post-upgrade simulation (red histogram) in comparison with pre-upgrade (blue histogram) due mainly to the MVD. Plot taken from [97].

with the measured ones [98]. The corrections factors obtained are

$$
\begin{array}{ll}
-3.5\%, & \text{if } r_i \ \leq \ 21 \text{ cm} \\
-3\%, & \text{if } 21 \text{ cm} \ < \ r_i \ \leq \ 25 \text{ cm} \\
-2.5\%, & \text{if } 25 \text{ cm} \ < \ r_i \ \leq \ 29 \text{ cm} \\
-2\%, & \text{if } 29 \text{ cm} \ < \ r_i,
\end{array}
$$

where the radius $r_i (= \sqrt{X_i^2 + Y_i^2})$ is calculated from the position of the particles. The factors have been applied to scale down the energy of all the MC samples

used in the analysis. The effect of the corrections can be seen in the right plot of figure 4.5. MC energies have been also smeared by 3% to account for the different energy resolutions in data and MC.

The energy corrections can be also calculated with the help of the SRTD and Presampler detectors. They provide a measurement of the preshowering and thus of the energy loss by the particles while traversing the material. Results and further details in the procedure can be found in [99]. A comparison of the different methods presented is shown in figure 4.7. The best description is achieved with the radial dependence correction, for SRTD and Presampler methods small shifts in the peak position are still visible. Note that during the development of the corrections and also of this analysis the dead material description in MC has been changing for tuning.
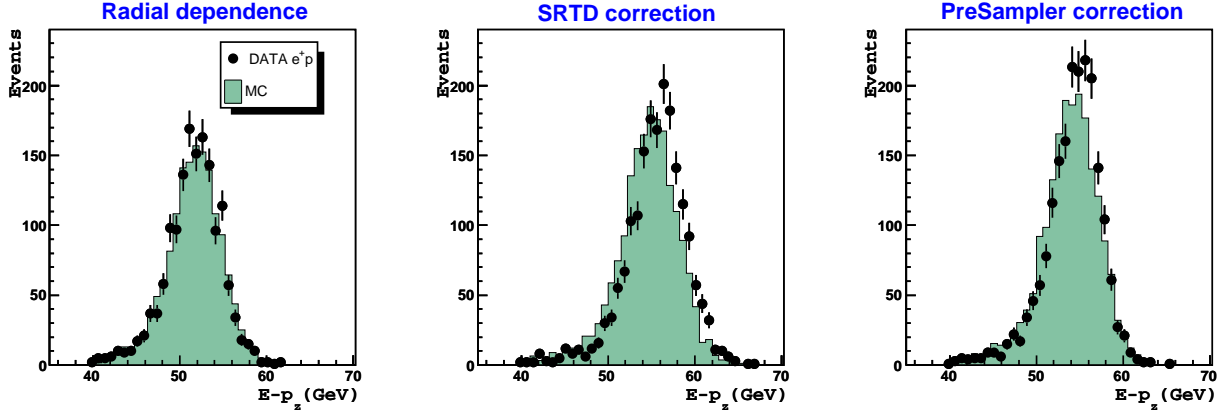


**Figure 4.7:** Comparison between different energy corrections for HERA II data.

### Energy calibration

In order to check the energy calibration, a comparison of the corrected energy of electrons measured in the CAL and the momentum of the particle measured in the CTD was performed.

Figure 4.8 shows the comparison of the quantity $E_e/p_{e,track} - 1$, with $E_e$ being the CAL electron energy and $p_{e,track}$ the momentum measured from the CTD track. Three different regions of the electron polar angle, $\theta_e$, are considered: 2 BCAL areas, $40° < \theta_e \leq 75°$ and $75° < \theta_e \leq 130°$ and RCAL region ($130° < \theta_e$). It can been seen that the energy measured in the CAL agrees with $p_{e,track}$ to within

3%. The comparison between data and MC shows an agreement to within 1-2%. This uncertainty is used for systematic checks.
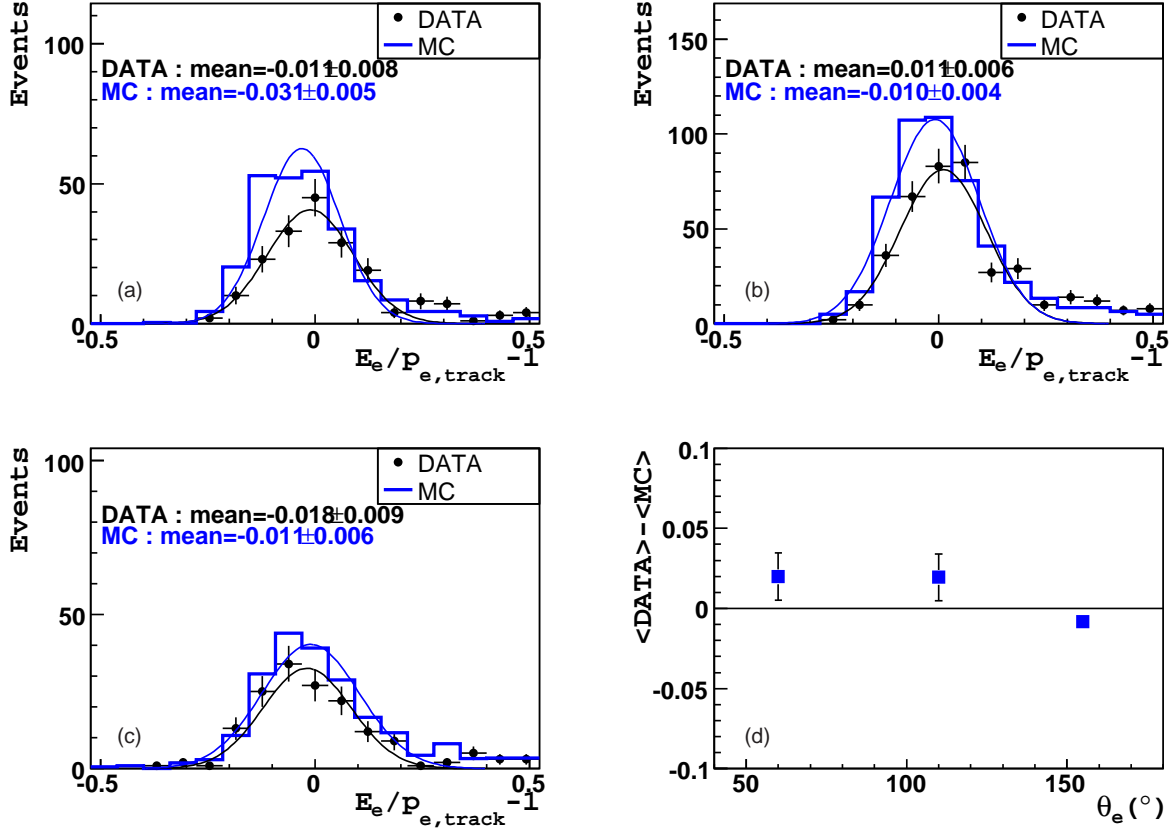


**Figure 4.8:** Comparison between the corrected electron energy measured in the CAL ($E_e$) with the corresponding momentum ($p_{e,track}$) measured in the CTD for $e^- p$ DATA and MC. Figures (a), (b) and (c) show the comparison for $40° < \theta_e \le 75°$, $75° < \theta_e \le 130°$ and $130° < \theta_e$, respectively. In (d), the differences between the mean values from MC and DATA are plotted.

As for the case of the energy, the position of the candidates is calculated using the position of the cells belonging to the candidates. The $X, Y$ and $Z$ positions are calculated as a weighted average of the cell centers where the weights are proportional to the logarithm of the energy deposited in that cell. For candidates found in RCAL or FCAL the $z$ position is fixed and for the ones found in the BCAL the radius $r = \sqrt{X^2 + Y^2}$ is fixed. When the candidates are found in the acceptance of the SRTD or HES detector, their position measurements are used to improve the CAL position.

## 4.4   Reconstruction of kinematic variables

Reconstructed angles and energies are then used to calculate the 4-momenta [4]:

$$
k = \begin{pmatrix} E_e \\ 0 \\ 0 \\ -E_e \end{pmatrix} \quad
p = \begin{pmatrix} E_p \\ 0 \\ 0 \\ E_p \end{pmatrix} \quad
k' = \begin{pmatrix} E'_e \\ E'_e \sin\theta_e \cos\phi_e \\ E'_e \sin\theta_e \sin\phi_e \\ E'_e \cos\theta_e \end{pmatrix} \quad
g' = \begin{pmatrix} E'_\gamma \\ E'_\gamma \sin\theta_\gamma \cos\phi_\gamma \\ E'_\gamma \sin\theta_\gamma \sin\phi_\gamma \\ E'_\gamma \cos\theta_\gamma \end{pmatrix},
$$

where $k$ and $k'$ are the 4-momenta of the initial and scattered electron and $p$ and $g'$ are the 4-momenta of the initial proton and the final state photon. $E'_e, \theta_e$ and $\phi_e$ are the energy, polar and azimuthal angle of the scattered electron while the same notation using the subscript $\gamma$ refers to the variables for the final state photon. The 4-momentum of the scattered proton has been omitted since it is not measured.

The kinematic variables (see equations 1.1-5) are calculated using the 4-momenta of final and initial state particles. Due to the almost $4\pi$ solid angle coverage of ZEUS, there are four independent measurements: the energies and the polar angles from the scattered electron and the final photon. This allows the determination of the kinematic variables $Q^2$, $x$ and $y$ with different methods.

**Electron method**

The electron method uses only the information based on the scattered electron. It is the simplest method since only the scattered electron energy, $E'_e$, and its polar angle, $\theta_e$, are required. The expressions for the kinematic variables are given by:

$$
Q^2_{el} = 2 E_e E'_e (1 + \cos\theta_e), \tag{4.7}
$$

$$
y_{el} = 1 - \frac{E'_e}{2 E_e}(1 - \cos\theta_e), \tag{4.8}
$$

$$
x_{el} = \frac{E_e}{E_p} \frac{E'_e (1 + \cos\theta_e)}{2 E_e - E'_e (1 - \cos\theta_e)}. \tag{4.9}
$$

**Double-angle method**

The double-angle method (DA-method) [100] uses not only the electron observables but also information coming from the hadronic final state. For the

---

[4]4-momenta are given in the ZEUS coordinate system (see figure 2.5) and neglecting the mass of the initial particles.

DVCS process the hadronic final state corresponds to the real photon. The formulae for this method are

$$Q^2_{DA} = 4E^2_e \frac{\sin\theta_\gamma (1 + \cos\theta_e)}{\sin\theta_e + \sin\theta_\gamma - \sin(\theta_e + \theta_\gamma)}, \tag{4.10}$$

$$y_{DA} = \frac{\sin\theta_e (1 - \cos\theta_\gamma)}{\sin\theta_e + \sin\theta_\gamma - \sin(\theta_e + \theta_\gamma)}, \tag{4.11}$$

$$x_{DA} = \frac{E_e}{E_p} \frac{\sin\theta_e + \sin\theta_\gamma + \sin(\theta_e + \theta_\gamma)}{\sin\theta_e + \sin\theta_\gamma - \sin(\theta_e + \theta_\gamma)}. \tag{4.12}$$

**Jacquet-Blondel method**

This method [101], which will be abbreviated as JB-method, relies only on the information from the hadronic final state and assumes that all the hadrons which escape undetected through the beam pipe carry very little transverse momentum. In our case, again, the hadronic final state corresponds to the real photon. The kinematic variables read as

$$Q^2_{JB} = \frac{2E_e (E_\gamma \sin\theta_\gamma)^2}{2E_e - E'_\gamma (1 - \cos\theta_\gamma)}, \tag{4.13}$$

$$y_{DA} = \frac{E_\gamma (1 - \cos\theta_\gamma)}{2E_e}, \tag{4.14}$$

$$x_{JB} = \frac{Q^2_{JB}}{s y_{JB}}. \tag{4.15}$$

The choice between these methods depends on the particular characteristics of the analysis. Depending on the kinematic region used, one method can be more precise than the others. Also the fact that the electron and JB methods use the measured energies makes them strongly dependent on the corrections applied. On the other hand the DA-method is not affected since it uses only angular observables.

Figure 4.9 shows a comparison between the reconstructed variables $Q^2$, $x$ and $W$ calculated with the DA-method (first column), electron method (second column) and JB-method (third column) and the true variables from non-radiative events of the DVCS MC simulation. $W$ is reconstructed for each of the methods as $W = \sqrt{4ys - Q^2}$.

The electron and DA-method have a good resolution for $Q^2$ in comparison with the JB-method, in which for low values of $Q^2$, the measured variables are

widely spread around the true ones. The electron method gives a very poor resolution for $W$ and $x$, also the same situation is observed for the $x$ calculated with the JB-method.

The DA-method has been used in this analysis since overall, it gives the best resolution and is independent of the energy corrections.
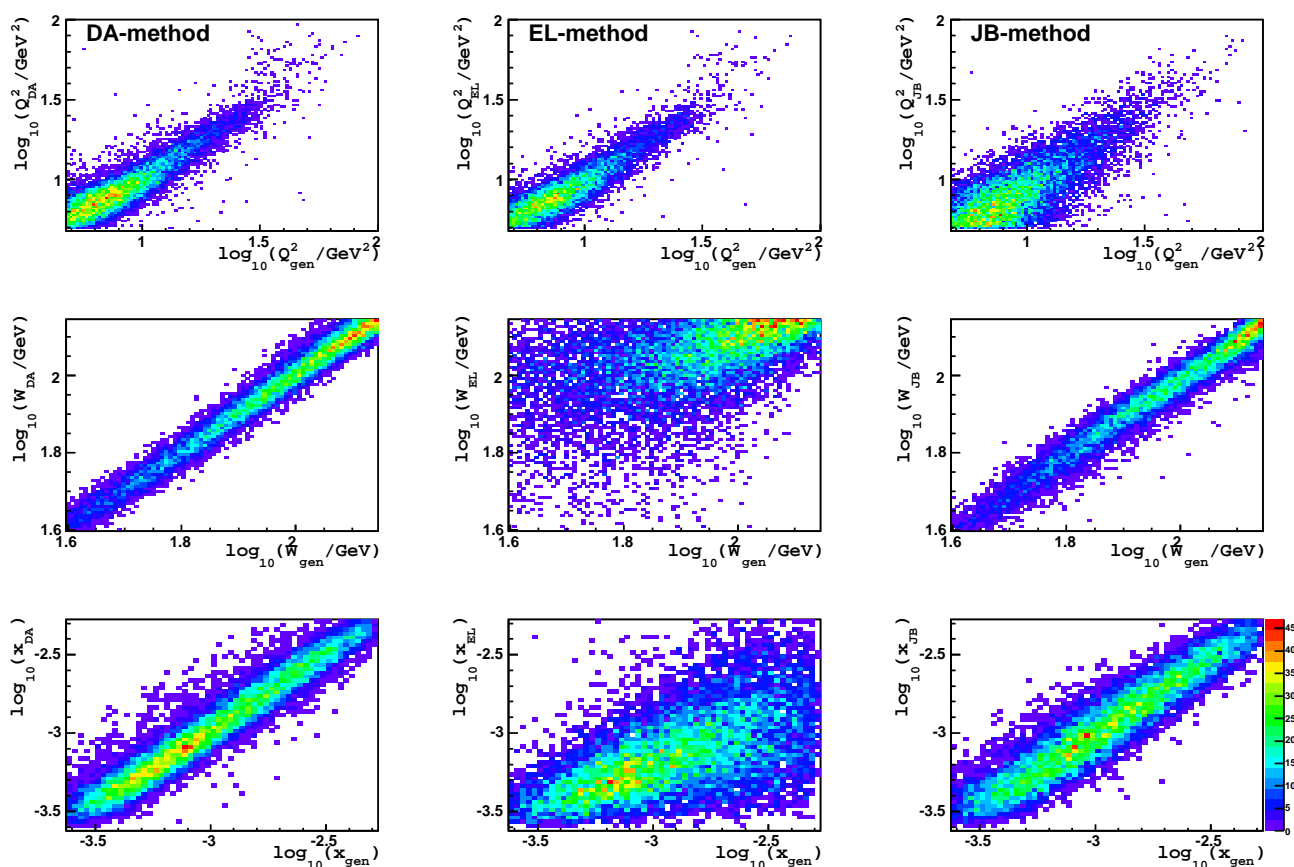


**Figure 4.9:** Comparison between the true and reconstructed kinematic variables for the DA, electron and JB methods.

# Samples definition and selection

This chapter will explain the analysis strategy followed to obtain a sample of DVCS and Bethe-Heitler events. The selection procedure, going from the trigger level to the more sophisticated set of cuts applied, is reviewed in detail.

## 5.1  Analysis strategy: e-sample and $\gamma$-sample

The technique for measuring the DVCS is to first select a sample of events which are characterized by the DVCS topology, since BH events have the same final state, the sample will contain a mixture of DVCS + BH. Assuming that the interference between the two processes is suppressed (see section 1.5), in a second step, the BH contribution is subtracted from the sample using the MC predictions leading to a "pure" DVCS sample.
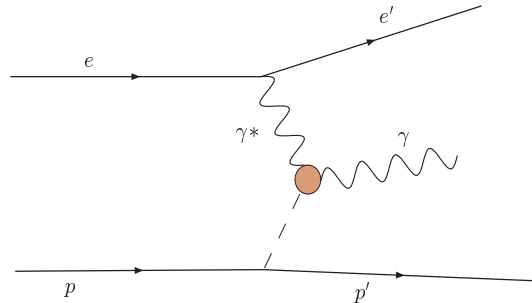


**Figure 5.1:** Schematic diagram for the DVCS process.

Looking again at a generic DVCS diagram (see figure 5.1), the main characteristics of the events are:

- 2 electromagnetic clusters, corresponding to the final particles electron and photon[1]. In the language of the previous chapter, this means two candidates

---

[1]The scattered proton escapes undetected.

identified by the SINISTRA electron finder. The cluster with higher $\theta$ w.r.t. the proton beam will be referred to as candidate 1 and the other as candidate 2.

- At most 1 track in the event which has to match with one of the electromagnetic clusters.

- No other activity in the detector, since we are interested in elastic events.

The ratio DVCS over BH is expected to increase as the photon is scattered at small $\theta$ angles. Hence, events are further classified in two different samples:

- **$\gamma$-sample**
  This is the signal sample. Events belong to this sample when the most forward electromagnetic cluster does not have a track associated with it and hence it is identified as the photon. Candidate 1 is assumed to be the scattered electron. This topology is dominated by events without tracks since the electron is scattered at higher $\theta$ angles where it is outside the acceptance of the CTD.

- **e-sample**
  Here events have a track matched with candidate 2, the electron in this case, while candidate 1 is the photon. BH events dominate this sample. The DVCS contribution is highly suppressed since this topology would correspond to very high values of $Q^2$. The e-sample is used as a control sample for the $\gamma$-sample to test the performance of the simulation and to cross-check the BH normalization. The elastic cross section of Bethe-Heitler events is also obtained from this sample.

Figure 5.2 shows an example of a $\gamma$-sample event (top) and a e-sample event (bottom) using the ZEUS event display.

These are the bases of the analysis. However, this view is very simplified in the sense that both samples contain not only DVCS + BH or BH only as other processes can also deliver the same topology. Studies of the backgrounds are shown in next chapters.
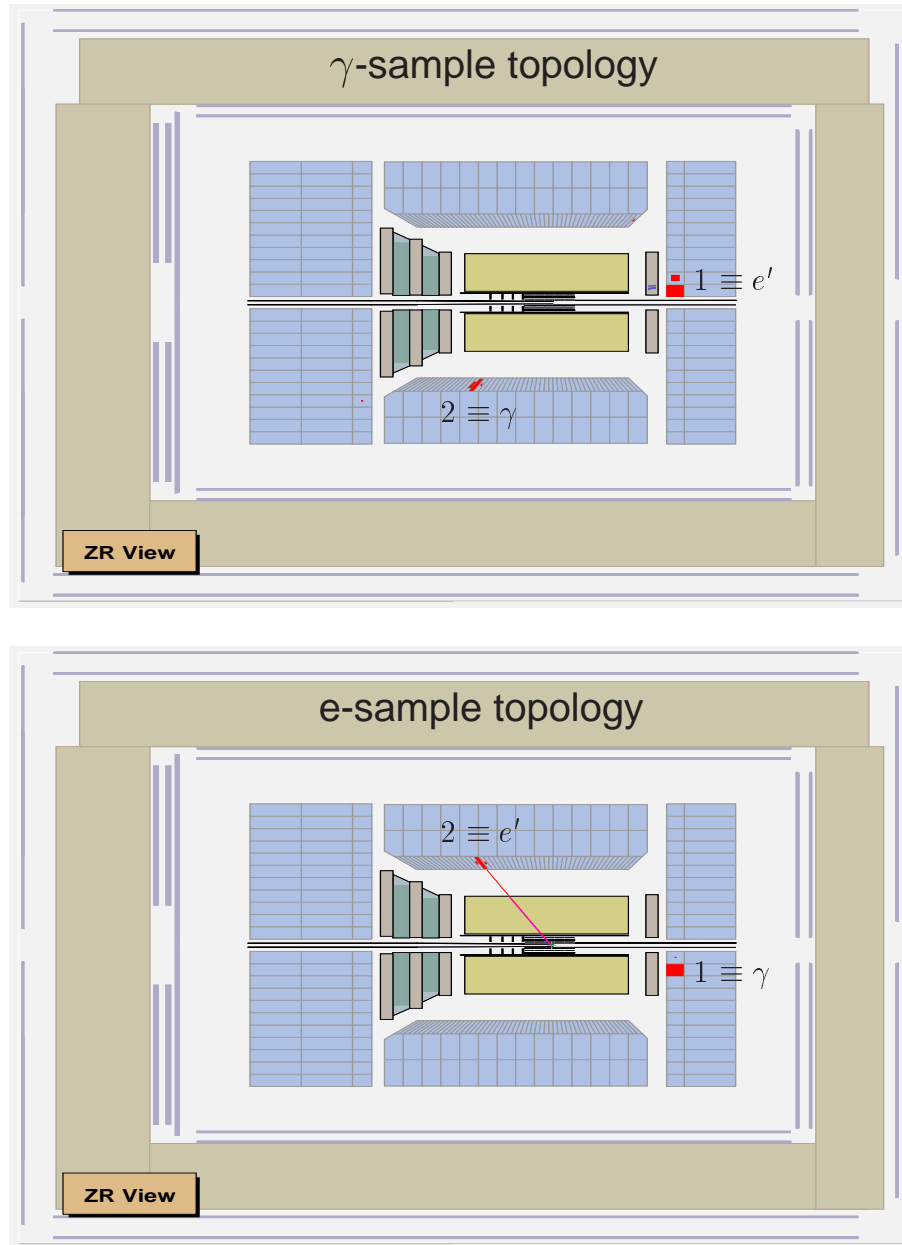
**Figure 5.2:** Topology of events in the $\gamma$-sample (top) and in the e-sample (bottom). When the candidate 2 is matched with a track, it is defined as an electron and classified in the e-sample .

## 5.2   Event selection

### 5.2.1   Hera II data set

The data sample used in the analysis was taken between 2003 and 2005. During this period HERA delivered both $e^+p$ and $e^-p$ collisions.

Not all the data taken can be used for analysis purposes. Runs have to pass a series of quality criteria such that the main components, like CTD and CAL, were fully functioning. This is done in order to guarantee a good data quality. The data samples analyzed correspond to an integrated luminosity of 135.6 pb$^{-1}$ for $e^-p$ data and 40.7 pb$^{-1}$ for $e^+p$ data. The samples are summarized in table 5.1.

| Year | Collisions | Integrated luminosity(pb$^{-1}$) | Systematic error(%) |
|---|---|---|---|
| 2003 | $e^+p$ | 2.1 | 5.1 |
| 2004 | $e^+p$ | 38.7 | 4.5 |
| 2004-05 | $e^-p$ | 135.6 | 2.7 |

**Table 5.1:** Integrated luminosity for the different years considered in this analysis.

## 5.2.2   Trigger selection and efficiency

Different logics,"slots", are implemented at the 3 levels of the ZEUS trigger (see section 2.2.7). A proper combination of logic allows the selection of the desired events. DVCS events were selected by requiring that the so-called SPP08 or DIS 11 slots fired. The only difference between the two slots resides at the first level. SPP08 is based on the multielectron slot, FLT62. DIS11 also employs the multielectron slot but makes use of the whole inclusive chain of FLT slots.

**Firts Level Trigger selection**

FLT62 slot triggers on two or more isolated electromagnetic clusters. Depending on the region in which the clusters are located, they are required to be above a certain energy threshold. Clusters located in the RCAL or BCAL are required to have $E > 2$ GeV. For the FCAL region, the threshold varies depending in which ring [2] the cluster is located: for the first ring it is set to infinity and for the second, third and outside third ring, the threshold is set to 20 GeV, 10 GeV and 5 GeV, respectively.

**Second Level Trigger selection**

At the SLT level, the conditions required for the events are:

- $E^{REMC} > 2.5$ GeV or $E^{BEMC} > 2.5$ GeV or $E^{FEMC} > 10$ GeV or $E^{FHAC} > 10$ GeV.

---

[2] First towers of the CAL around the beam hole define the first ring.

- Energy in the first ring of the FCAL, $E_{\text{fcalbp}}$, smaller than 20 GeV.

- $E - p_z > 30$ GeV.

- SLT electron energy $> 5$ GeV.

- Off-momentum electrons[3] rejection: Events are rejected when the SLT electron is located in the angular region of $172° < \theta < 174°$ and $|\phi| < 10°$ and $E_{Total}^{CAL} - E_{SLTe} < 1.5$ GeV.

## Third Level Trigger selection

The trigger logic at the TLT is given by the following conditions:

- Number of hadronic islands is equal to 0.

- Two electromagnetic islands, one with $E > 4$ GeV and the other with $E > 2$ GeV.

- $E_{fcalbp} < 50$ GeV.

- Difference of azimuthal angles between the two islands greater than $\pi/2$.

In addition to the criteria explained above, at each trigger level general conditions are applied to reduce background. At the FLT level, events are rejected by signals coming from the C5, VetoWall, SRTD or CTD (see section 2.2). The SLT uses timing information coming from the CAL to veto beam-gas background events. At the TLT level, it is possible to recognize and reject cosmic and beam-halo muons.

## Trigger efficiency

Trigger decisions are also simulated for MC events. In the analysis, data and MC events are passed through the same chain of slots and therefore, the simulation should reproduce the behavior of the data. To check this assumption, the trigger efficiency of the main FLT bit for the analysis, FLT62, has been studied.

The definition of FLT62, two or more electromagnetic cluster with energy threshold starting at 2 GeV, makes the efficiency strongly dependent on the lower energy cluster. In the typical DVCS topology, the DIS electron will trigger as

---

[3]Electron beam particles which lose part of their momenta due to collision with residual gas molecules from the beam pipe walls.

one of the electromagnetic candidates and the final photon as the second. The typical energy for the DIS electron is above 15 GeV and the photon, with lower energy, could be affected by threshold effects.

To study the trigger efficiency, the idea is to select a sample using independent triggers. An inclusive[4] trigger chain relying on the selection of the DIS electron in the RCAL was chosen. This selection gives an unbiased sample to test trigger efficiencies for the lower energy candidate. The sample used to study the efficiencies correspond to the e-sample topology with the following cuts:

- 2 electron candidates, one (1) located in the RCAL and the other (2) either in BCAL or RCAL.

- $E_1 > 15$ GeV and electron identification probability $P_1 > 0.6$.

- $N_{vtxtrk} = 1$. The track has to be matched with the candidate 2.

- 40 GeV $<$ E $-$ p$_z$ $<$ 70 GeV.

- $|z_{vtx}| < 50$ cm.

Using this sample, the efficiency has been calculated as a function of the energy of candidate 2, $E_2$. The definition of the efficiency is given by

$$\text{efficiency} = \frac{\text{N}^{\text{sample \& FLT62}}}{\text{N}^{\text{sample}}}, \tag{5.1}$$

where $\text{N}^{\text{sample}}$ is the number of events in the basic sample and $\text{N}^{\text{sample \& FLT62}}$ is the number of events in the basic sample and fired by the FLT62.

The efficiency has been calculated for data and MC. Figure 5.3 shows the FLT62 trigger efficiency for both data sets, $e^+p$ and $e^-p$ . Also two different cases have been considered: when the candidate 2 is found in the RCAL and when it is found in the BCAL region. For clusters with low energy ($E_2 \sim 2 - 3$ GeV), the efficiency is around 0.5, increasing to almost 1 for energies above 5 GeV. There are no significant differences between candidates in the RCAL or BCAL and similar behavior is observed for the $e^+p$ and $e^-p$ sample.

The MC efficiencies calculated with GRAPE are shown in figure 5.4. They exhibit the same behavior as the data, with the same rapid increase of the efficiency for higher values of $E_2$. MC efficiencies have higher values in the BCAL

---

[4]TLT SPP02 and FLT30.
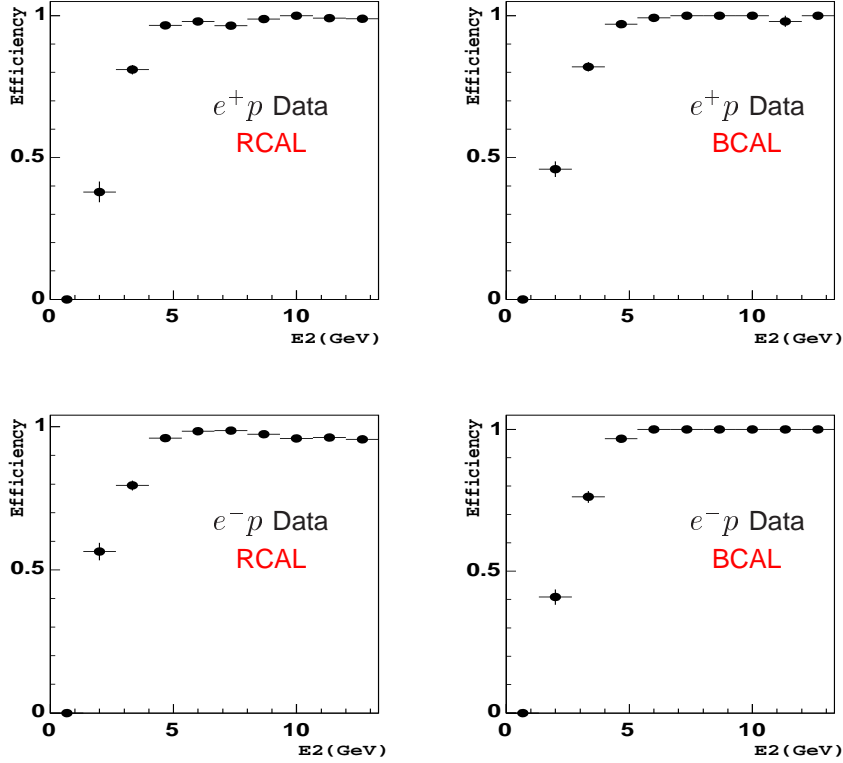
**Figure 5.3:** Trigger efficiency of the FLT62 slot as a function of E2 for $e^+p$ (top) and $e^-p$ (bottom) data. Efficiencies are shown depending on the position of the second candidate, RCAL (BCAL) in the left (right) plots.

region than in the RCAL. No differences are observed where comparing both $e^+p$ and $e^-p$ data.

Two strategies can be followed from this: one can try to match the behavior of data and MC efficiencies for $E_2 < 5$ GeV calculating a correction factor or one can go to the region with efficiencies $\sim 1$ which means $E_2 > 5$ GeV. A big disadvantage for the latter is the reduction of the number of events due to the harsh requirement on the energy. However, as one of the goals of this analysis is to explore the region in which asymmetry measurements could be performed and since corrections for trigger efficiencies can deliver false asymmetries, the second option was chosen.

### 5.2.3   Analysis cuts

In this section, the cuts applied to obtain the final sample will be explained. Together with the trigger selection, additional requirements are needed to eliminate remaining background as well as to avoid regions in which the MC simulation

does not describe the data.

The quantities labeled with the subscripts 1 and 2 refer to the candidates 1 and 2 as defined in the section 5.1. The observables associated with the candidates
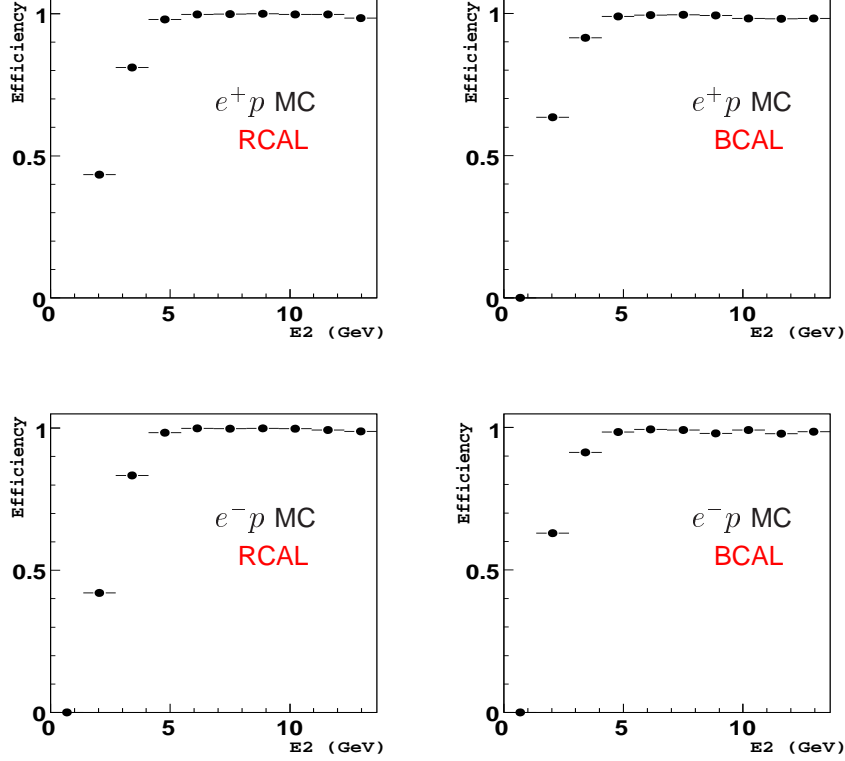


**Figure 5.4:** Trigger efficiency of the FLT62 slot as a function of E2 for $e^+p$ (top) and $e^-p$ (bottom) GRAPE MC. Efficiencies are shown depending on the position of the second candidate, RCAL (BCAL) in the left (right) plots.

are the ones given by SINISTRA, as explained in section 4.3. The following cuts were applied to define the final sample:

- **Number of electron candidates greater than 1.**
  After applying the complete set of cuts, no event was found with more than 2 candidates. Moreover with a loose selection[5], events with 3 candidates were found but doing the analysis assuming different combinations between them, no event was found surviving the complete set of cuts.

- $\mathbf{E_1 > 15}$ **GeV and** $\mathbf{E_2 > 5}$ **GeV**.

- **Electron identification probability:** $\mathbf{P_1 > 0.6}$ **and** $\mathbf{P_2 > 0.6}$.

---

[5]Only trigger selection, $E - p_z$ and energy and probability cut apply to the candidate 1.

- **Candidate 2 inside the CTD acceptance.**
  In this region there is a high efficiency for the reconstruction of the tracks and since the separation between electrons and photons is done using tracks, this is also the region which allows a clear identification. The angular limits for the region are defined according to the minimun number of hit superlayers needed to have well reconstructed tracks, which is equal to 3 [93].

- **Number of vertex fitted tracks less than 2**.
  If there is one track, it has to be matched (see section 4.3) with one of the two candidates and have a momentum $p_{trk} > 0.5$ **GeV**.

- $|z_{vtx} < 100$ **cm**$|$.
  This cut rejects events in which $z_{vtx}$ is outside the central region of the detector (CTD region) where the vertex reconstruction is not well-defined.

- **40 GeV** $< E - p_z < $ **70 GeV**.
  The lower limit rejects background coming from photoproduction events where the electron escapes trough the rear beam pipe and hence, reduces the values of $E - p_z$. The upper limit is used to reduce overlay events in which DIS events and beam gas or cosmic events occur at the same time. In section 6.4, a detailed study of this background is presented.

- $E_{FCAL} < 1$ **GeV**.
  Energy deposited in the FCAL part of the detector is required to be very small. This rejects possible inelastic and proton dissociation events which typically deposit a considerable amount of energy around the FCAL beam pipe.

- $E_{BHAC} < 1$ **GeV**.
  The cut is applied to reject hadronic background which leave a large fraction of energy in the hadronic part of the BCAL.

- **Elasticity cut.**
  This cut removes events with energy deposits in the CAL which do not belong to the two candidates. It aims to ensure a sample of elastic events reducing proton dissociation background. In addition higher variations in the calorimeter noise will be reduced as well. The cut is applied in the following way: events are rejected if individual cells, which do not belong to the candidates, have a energy above these values :
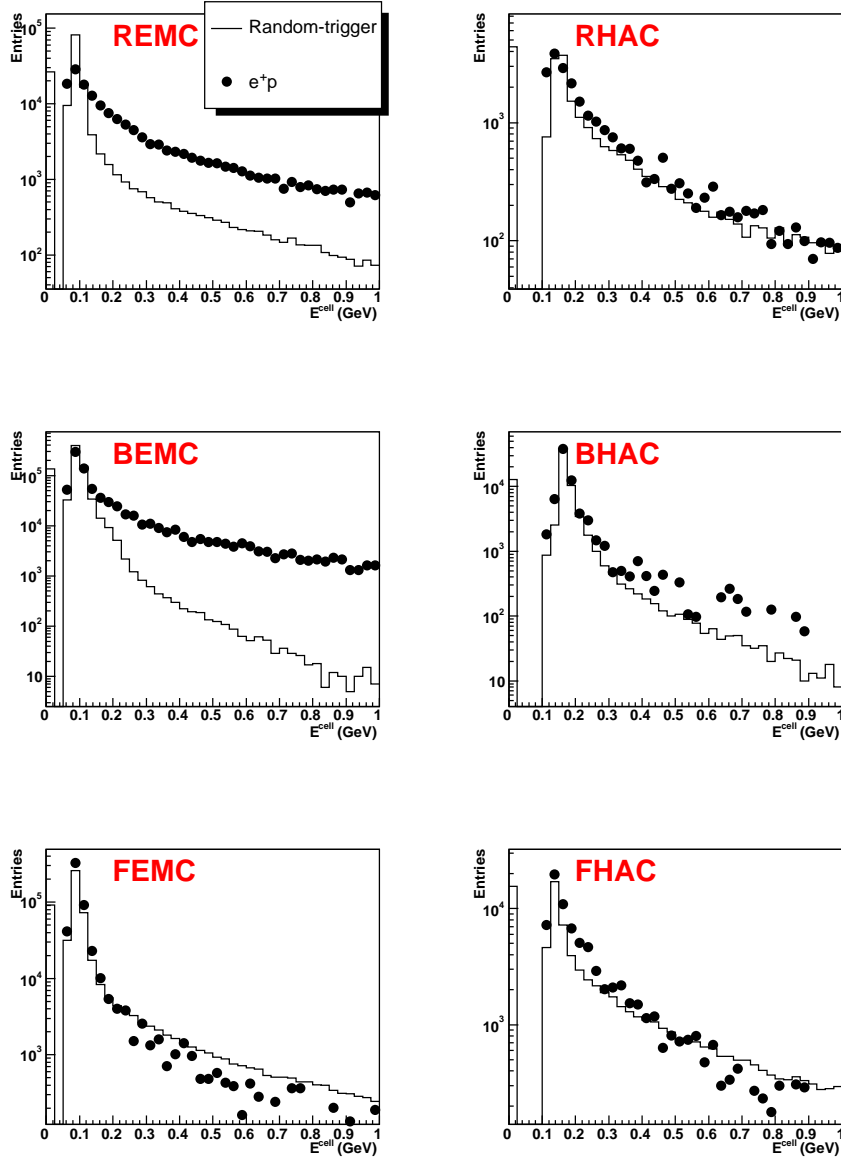
**Figure 5.5:** Energy deposited in individual cells which do not belong to the candidates in $e^+p$ and random trigger events. Different sections of the calorimeter are shown.

- RCAL region : 150 MeV for EMC cells and 300 MeV for HAC cells.

- BCAL region : 180 MeV for EMC cells and 350 MeV for HAC cells.

- FCAL region : 280 MeV for EMC cells and 300 MeV for HAC cells.

The threshold values were obtained by comparing the $E^{cell}$ from the $e^+p$ data sample with random trigger events (see Fig. 5.5).

- **Box-cut and CAL-crack cuts.**
  These cuts reject events which are situated in problematic areas of the

detector which are known to be not well simulated. The box-cut cut rejects events in which the impact positions of the candidates on the RCAL surface are inside an area of $14 \times 18$ cm$^2$ in $x$ and $y$. The CAL-crack cut rejects events which are located in the crack region between the two halves of the RCAL, $|x - 10| < 2.5$ cm and $|x + 10| < 2.5$ cm.

# Deeply Virtual Compton Scattering data analysis

This chapter describes different studies performed in order to understand the sample of DVCS candidates. The discussion about background contributions affecting the e-sample and $\gamma$-sample are presented here. The comparison between the data and MC simulation are shown together with different studies to understand remaning problems in the analysis. Finally, a study of the non-$ep$ background is summarized.

## 6.1 Definition of the kinematic region

For both the e-sample and the $\gamma$-sample samples, the kinematic variables are calculated assuming that the candidate 1 is the scattered electron. The cuts which defined the kinematic region of interest for DVCS are:

- **40 GeV < W < 140 GeV**

- **5 GeV$^2$ < Q$^2$ < 100 GeV$^2$**

- **|t| < 1 GeV$^2$**

The number of events selected by the cuts explained in the previous chapter and belonging to the kinematic region defined above are summarized in table 6.1.

## 6.2 e-sample studies

### 6.2.1 Physics backgrounds

Processes which could deliver the same topology of the e-sample were considered as potential sources of background. The background processes are studied based

| Sample | $e^+p$ | $e^-p$ |
|---|---|---|
| $\gamma$-sample | 140 | 481 |
| e-sample | 248 | 907 |

**Table 6.1:** Number of events selected for the different samples and periods.

on the MC samples describe in chapter 3.

- Dilepton production.
  Dilepton production, $ep \rightarrow e'e^+e^-p$ and $ep \rightarrow e'e^+e^-X$, delivers the same topology as the e-sample if only two leptons from the final state are detected. In addition, one of them has to be scattered at large $\theta$ angles where its associated track is not measured and therefore it fakes the photon in the e-sample. Samples of elastic and inelastic contribution were considered. The absolute value of the cross section given by the MC program was used to normalize the sample. The contribution for the dilepton background to the e-sample was estimated as 3.5% (4.7%) for the $e^-p$ ($e^+p$ ) data set.

- Diffractive $\rho$ production: $ep \rightarrow e'\rho p'$, $\rho \rightarrow \pi^+\pi^-$.
  The event topology of the e-sample is also faked by diffractive $\rho$ production. It was found that no events survive the analysis cuts.

- Diffractive $J/\psi$ production: $ep \rightarrow e'J/\psi p'$, $J/\psi \rightarrow e^+e^-$.
  This process can contribute to the e-sample under the same conditions as explained for the dilepton background, mainly the loss of one of the final state leptons. In previous studies [104], this contribution was estimated $\sim 1\%$ of the total e-sample and is therefore neglected here.

**Proton-dissociative background**

Although the analysis cuts are used to ensure the selection of elastic events, a sizeable fraction of inelastic[1] events is still present in the sample. This background refers to the process in which the proton dissociates to a low-mass hadronic system. When the low-mass system escapes undetected into the forward beam pipe, the topology of the event is identical to the elastic one. The study of this background is done by means of the GRAPE MC (see section 3.2.2) which can generate elastic and inelastic contributions.

---

[1]Proton-dissociative background is referred to as inelastic.
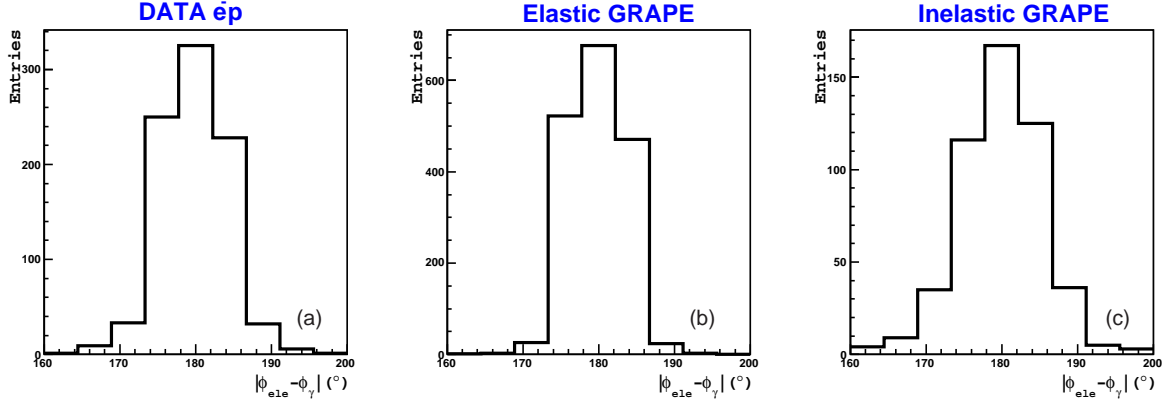
**Figure 6.1:** Coplanarity distributions of the e-sample for data (a), elastic (b) and inelastic (c) GRAPE MC.

The fraction of inelastic events given by the MC was adjusted using the coplanarity method. In a pure elastic sample, the two-final state particles should balance in transverse momentum resulting in a back-to-back configuration in the transverse plane. In other words, the difference between the azimuthal angles of the particles, the coplanarity, should peak at 180 degrees. Figure 6.1 shows the distributions of the coplanarity for the $e^-p$ data (a) and for elastic (b) and inelastic (c) GRAPE MC samples. The inelastic component has a broader distribution than the elastic. For the adjustment, both contributions were mixed and fitted to the data by minimizing the $\chi^2$ distribution. The fractions obtained by the fitting procedure and the MC predictions are listed in table 6.2.

| | Inelastic contribution (%) | |
|---|---|---|
| | MC prediction | fitted |
| $e^+p$ | 29 | $26.6 \pm 15.6$ |
| $e^-p$ | 22.5 | $38.7 \pm 13.3$ |

**Table 6.2:** MC prediction for the inelastic contribution in comparison with the fraction obtained by fitting the coplanarity distribution.

The coplanarity distributions for $e^-p$ data and MC, before and after the adjustment, are shown in figure 6.2.

The values obtained here were used to readjust the mixture of elastic and inelastic GRAPE but keeping the absolute normalization.

83
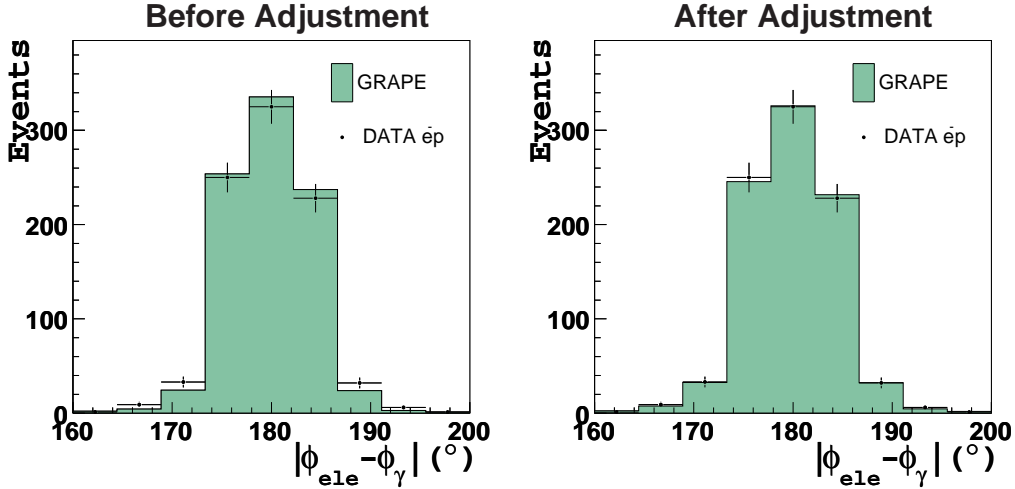
**Figure 6.2:** Distribution of the coplanarity for $e^- p$ data compared with MC before and after the adjustment of the inelastic contribution (see text).

### 6.2.2   Data and MC comparison

The comparison between the data and MC distributions of a selected group of variables are shown in figure 6.3 for $e^- p$ and in figure 6.4 for $e^+ p$ . In each of the plots, the dots represent the data distributions and the different histograms show the MC predictions for the contributing processes to the e-sample . The GRAPE contribution contains both, elastic and inelastic parts adjusted as previously explained. The dilepton contribution also corresponds to the sum of elastic and inelastic parts. MC histograms are normalized to the luminosity of the data. These MC predictions are added together and the result is shown by the topmost line.

The distributions present a clear disagreement on the normalization, where MC predictions are higher than data. This problem is further discussed in the next section. No significant differences are observed in the behavior of the $e^+ p$ and $e^- p$ samples. As mention in section 6.1, the kinematic variables are calculated assuming that the candidate 1 is the scattered electron. In case of the e-sample topology, these variables does not correspond to the "true" kinematics and therefore are labeled as $Q^2_\gamma$ and $W_\gamma$.

### 6.2.3   Normalization of the BH contribution

The normalization of the BH contribution is a crucial point, since the extraction from the $\gamma$-sample of a pure DVCS sample directly depends on the amount of BH which is subtracted.
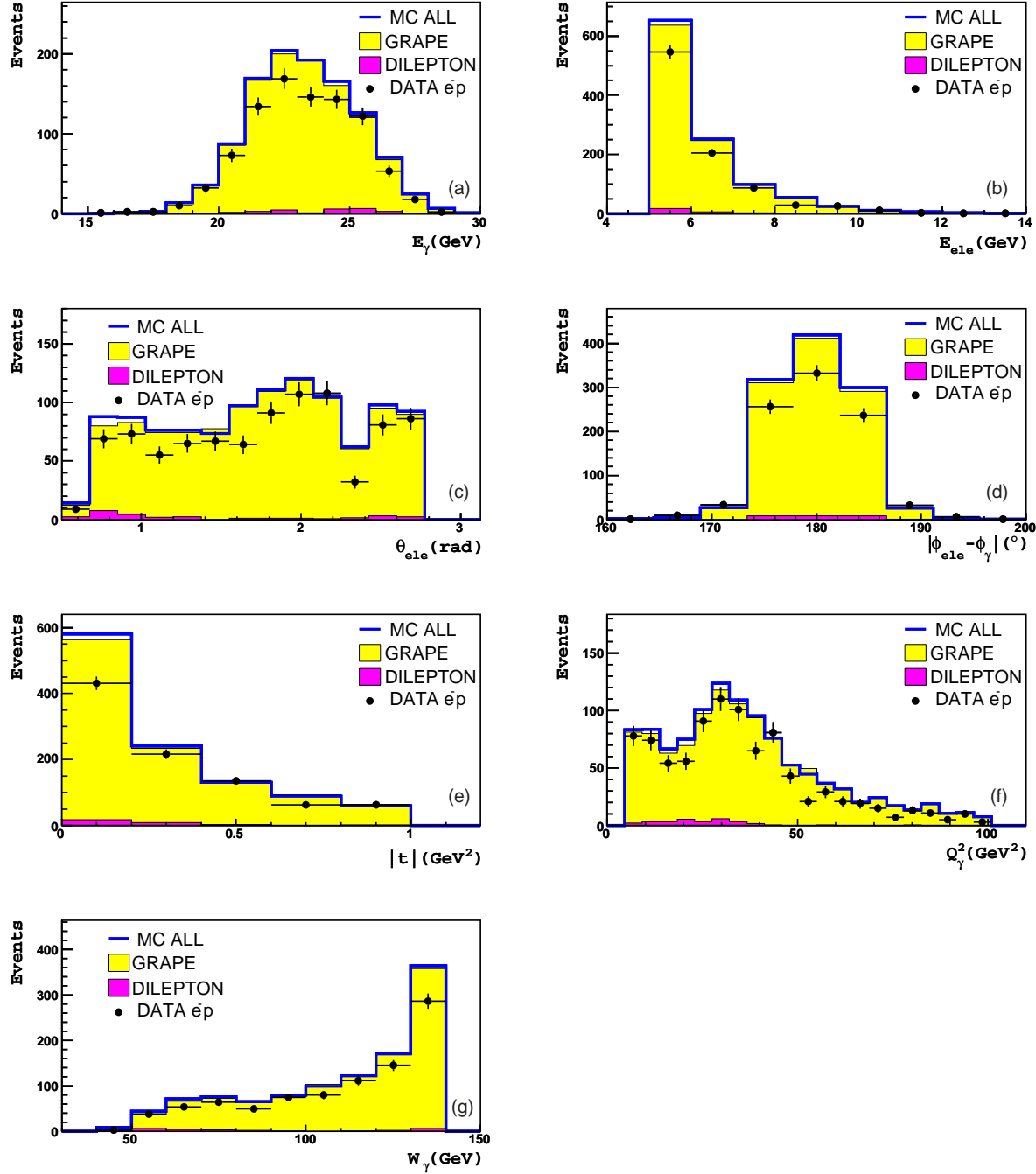
**Figure 6.3:** e-sample control plots for $e^- p$ : data distributions of the energy of the $\gamma$ (a), the energy of the electron (b), the polar angle of the electron (c), the coplanarity (d), the absolute value of $t$ (e), $Q^2_\gamma$ (f) and $W_\gamma$ (g) compared to the MC samples. $Q^2_\gamma$ and $W_\gamma$ refer to the kinematic variables considering the photon as the scattered electron. MC histograms are normalized to the luminosity of the data.

85
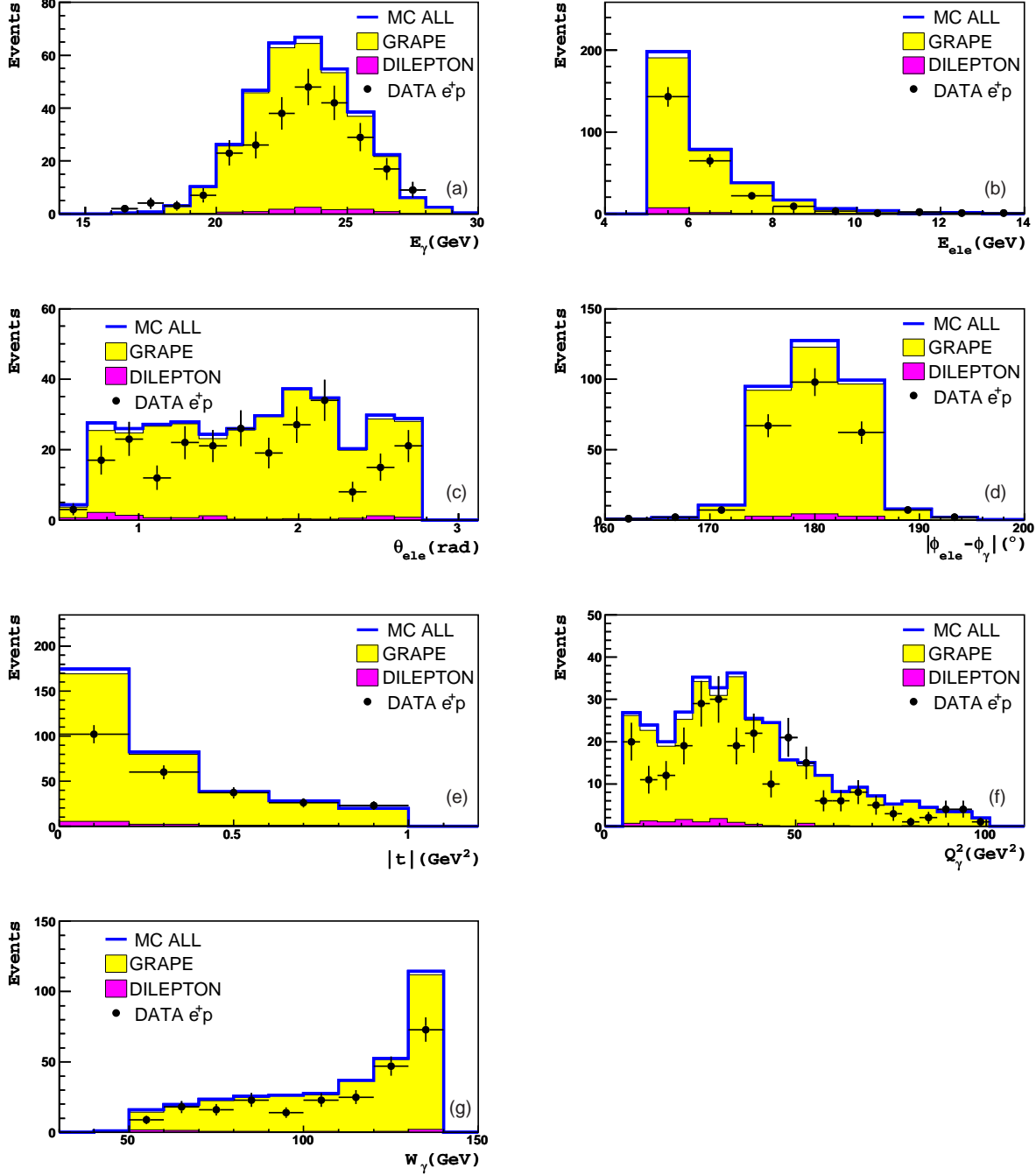
**Figure 6.4:** e-sample control plots for $e^+p$ : data distributions of the energy of the $\gamma$ (a), the energy of the electron (b), the polar angle of the electron (c), the coplanarity (d), the absolute value of $t$ (e), $Q^2_\gamma$ (f) and $W_\gamma$ (g) compared to the MC samples. $Q^2_\gamma$ and $W_\gamma$ refer to the kinematic variables considering the photon as the scattered electron. MC histograms are normalized to the luminosity of the data.

The absolute normalization of the BH contribution is not described for the e-sample, as shown in the previous control plots. After the subtraction of the dilepton contribution from the data, the GRAPE MC predictions are $\sim 15\% - 20\%$ higher than the data.

Attempts to explain this problem lead to two of the selection criteria: the number of tracks fitted to the vertex and the elasticity cut. If these cuts are removed, the problem with the normalization disappears as seen in figure 6.5. This may be a hint of an incomplete MC simulation, i.e., more dead material in
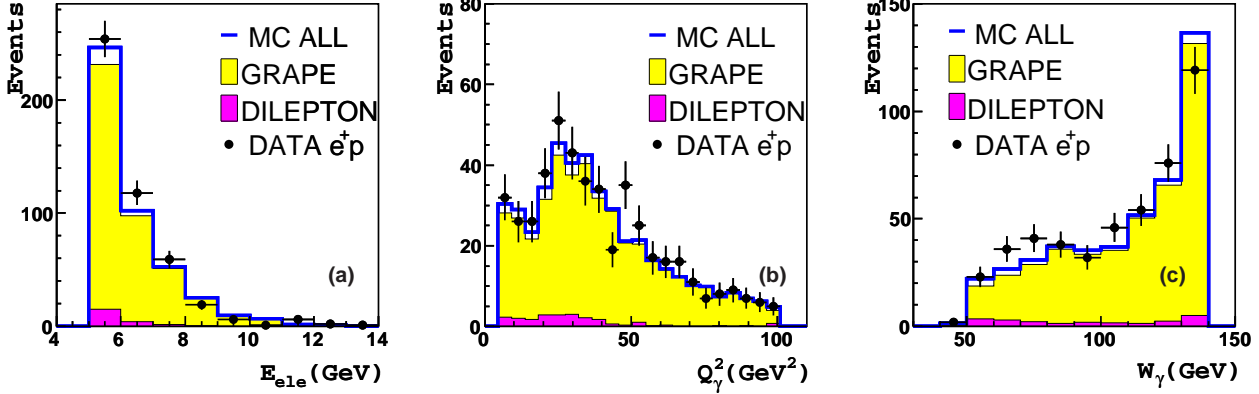


**Figure 6.5:** $e^+p$ data distributions of $E_{ele}$ (a), $Q_\gamma^2$ (b) and $W_\gamma$ (c) compared with MC for the e-sample without applied the requirement $N_{vtxtrk} > 2$ and the elasticity cut. The normalization problem seen before (see figure 6.3) disappears.

the detector than simulation results in more secondary interactions. However, this solution of the normalization problem could also be a fortunate coincidence.

Moreover if these cuts are removed from the $\gamma$-sample in order to have the "proper" normalization for the BH contribution, the data in the $\gamma$-sample is higher than the MC predictions. A visual scan of the new accepted events showed that most of them had a very different topology than the expected for the $\gamma$-sample, mainly consisting in events with a high number of tracks.

Considering that the e-sample and the $\gamma$-sample could have different behaviors, it was decided to use the $\gamma$-sample itself to cross-check the BH normalization. This has the advantage of making use of the same topology. The region of the high-W (from 160 GeV to 240 GeV) in the $\gamma$-sample is dominated by the BH process with a small contribution from the DVCS. The background of DVCS was estimated by MC and subtracted. Then, MC predictions of GRAPE were compared with the data.

The ratio between the number of events predicted by GRAPE and the events found in data in the high $W$ region in the $\gamma$-sample are shown in table 6.3;

the values obtained for the e-sample are also shown. The quoted uncertainties correspond to the statistical uncertainties and the following systematics checks: the electromagnetic energy scale in MC was varied by $\pm 2\%$ in BCAL and $\pm 1\%$ in RCAL; the mixture of elastic-inelastic[2] was vary according with its uncertainty and only for the high $W$ $\gamma$-sample , DVCS MC prediction was varied by $\pm 50\%$. The values obtained are consistent within uncertanties for both samples.

| | high W $\gamma$-sample | | e-sample | |
|---|---|---|---|---|
| | $e^+p$ | $e^-p$ | $e^+p$ | $e^-p$ |
| Data/MC | $0.87 \pm 0.09$ | $0.92 \pm 0.05$ | $0.82 \pm 0.10$ | $0.85 \pm 0.07$ |

**Table 6.3:** The ratio between number of data and MC events for different samples.

## 6.3   $\gamma$-sample studies

### 6.3.1   Physics backgrounds

Bethe-Heitler process is the main background to the signal sample. In this section, other processes that can mimic the topology of the $\gamma$-sample are considered.

**Vector meson background**

The diffractive electroproduction of $\omega$ and $\phi$ mesons was considered as a possible sources of background to the $\gamma$-sample .

- $\omega$ background: $ep \rightarrow e'\omega p'$, $\omega \rightarrow \pi^o\gamma$.
  This process can produce the same topology as the $\gamma$-sample when only one of the decay products of the $\omega$ meson is detected in addition to the scattered electron. This background was investigated using a sample generated by ZEUSVM (see section 3.2.4). The MC was normalized using the measured $\omega$ cross section [103]. After the selection cuts, the contribution of $\omega$ events was estimated to 0.3% of the $\gamma$-sample and therefore neglected.

  In order to check the proper normalization of this MC, the procedure used in [104] has been followed. Calorimeter objects called *condensates* are groups of adjacent  cells with energy above some cut-off [3]. Considering

---

[2]The adjustment described in 6.2.1 was also performed for the high $W$ $\gamma$-sample resulting in $(15 \pm 6)\%$ and $(21 \pm 5)\%$ inelastic contribution for the $e^-p$ and $e^+p$ sample, respectively.
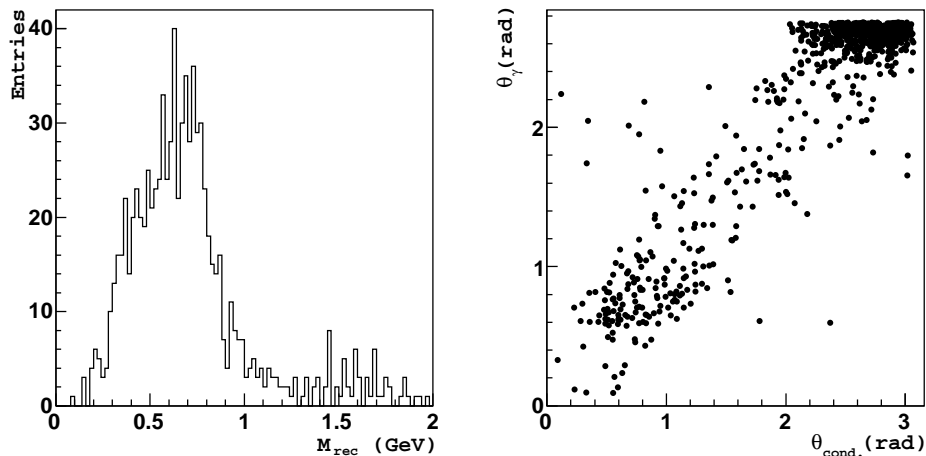
**Figure 6.6:** Invariant-mass spectra (left) and correlation between polar angles (right) of the candidate 2 and the *condensate* in the γ-sample for a $\omega$ MC sample.
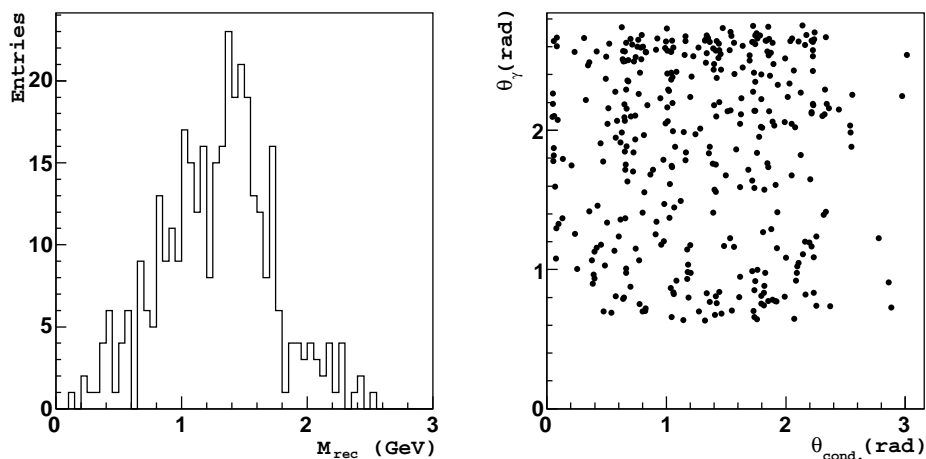


**Figure 6.7:** Invariant-mass spectra (left) and correlation between polar angles (right) of the candidate 2 and the *condensate* in the γ-sample for $e^-p$ data.

only *condensates* formed by cells that do not belong to the candidates, the MC simulation for $\omega$ events shows that it is possible to reconstruct a peak ($\sim 0.65$ GeV, which is close to $M_\omega = 0.78$ GeV) in the invariant-mass spectra using the candidate 2 and the most energetic *condensate*. The reconstructed value is underestimated due to the uncalibrated quantities used to build the *condensates*. In addition, the *condensate* and the candidate 2

---

[3]For pure EMC *condensates* the cut-off is set to 0.1 GeV and for pure HAC and mixed HAC-EMC *condensates* the value is 0.2 GeV.

have an angular correlation. In figure 6.6, the invariant-mass spectra (left) and the correlation between the polar angles (right) for the $\omega$ MC sample are shown.

As seen in figure 6.7, neither of the behaviors exhibited for the $\omega$ MC are reproduced in data which confirms the negligible contribution of this background obtained before.

- $\phi$ background: $ep \rightarrow e'\phi p'$, $\phi \rightarrow K_L^0 K_S^0$.
  In this process, when a further decay of the $K_S^0 \rightarrow \pi^0 \pi^0$ is produced, and these neutral pions decay into 2-$\gamma$'s, the $\gamma$-sample topology can be obtained if only one of the decay products is detected. A MC sample of $\phi$ was used to estimate the contribution of these events. The normalization of the sample was done using the measured cross section [105]. It was found that no events survive the selection.

**Proton-dissociative background**

No MC generator for inelastic DVCS was available for this analysis. Thus, following [104], the fraction of inelastic contribution was taken from the measurements of the diffractive $J/\psi$ photoproduction [106]: $f = 17.5 \pm 1.3(stat.)^{+3.7}_{-3.2}(syst.)\%$. The use of this value is based on the assumption than the inelastic background in diffractive interactions is process independent. The assumption is confirmed, within a relative large uncertainty, from the measurements of elastic vector-mesons. It is assumed that the fraction has no kinematic dependence. However it is possible to speculate about the contribution of the inelastic component, for example, looking at possibles time or kinematic dependences. Time dependences can be due to the removal of the Forward Plug Calorimeter (FPC) [107] which was previously used to reject inelastic events. Thus, samples at HERA II might contain more inelastic events.

In figure 6.8, the fractions of inelastic events obtained in the different samples belonging to this analysis and to HERA I analysis are plotted as a function of the $W$ region. Low $W$ and high $W$ represent $W$ between 40 GeV and 140 GeV and between 160 GeV and 220 GeV, respectively. For the e-sample (squares) and $\gamma$-sample (triangles) of this analysis, the fraction was obtained using the coplanarity method (see section 6.2.1). The point labeled as DVCS HERA I corresponds to the previous analysis of DVCS [104]. The LPS[4] HERA I point refers to the proton-dissociative contribution estimated in the inclusive diffractive cross

---

[4]LPS stands for Leading Proton Spectrometer.
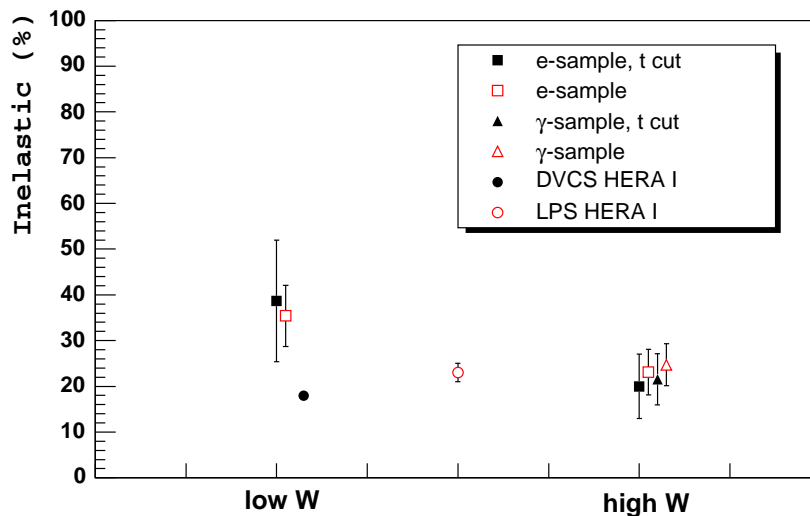
**Figure 6.8:** Inelastic contributions for various samples of this analysis and HERA I analysis as a function of $W$. The contributions for the e-sample and γ-sample of this analysis were calculated with (solid markers) and without (hollow markers) the cut $|t| < 1 \mathrm{GeV}^2$. All the results are consistent, however a tendency to higher contributions is observed in the low $W$ region for e-samples.

section measurement [108] using the LPS, calculated for the whole $W$ range. The values of this analysis at low $W$ show a tendency to be higher than the previous HERA I and than the HERA II high $W$ results, nevertheless all the values are consistent within the uncertainties.

**Other contributions**

In photoproduction, though the electron is scattered at very small angles and lost down the rear beam pipe, isolated hadrons could be misidentified as the scattered electron. The MC program PYTHIA [89] was used to generate a photoproduction sample with single photons in the final state [112], however no events survived the analysis selection. Another source of background could be prompt photon events. These are characterized by the presence of a high-$E_T$ photon which emerges directly from the lepton-proton interaction. From the MC simulation, the prompt photon signal was rejected after the cuts, mainly due to jets present in the events. Finally, the possible contamination from inclusive DIS and diffraction were tested using samples of DJANGOH [113] and RAPGAP [114], respectively. No events were found for both contributions.

## 6.3.2   Data and MC comparison

Distributions of the $e^-p$ and $e^+p$ $\gamma$-sample are shown in figures 6.9 and 6.10, respectively. The data are compared with the MC predictions for the contributing processes: elastic and inelastic BH and elastic DVCS. All the contributions have been normalized to the luminosity of the data. The BH predictions have been adjusted using the coplanarity method as described in section 6.2.1. The fractions used for the adjustment correspond to the fit performed on the high W $\gamma$-sample since the Bethe-Heitler events have the same topology as the ones contributing to the kinematic region of interest (40 GeV < W < 140 GeV).

Overall, a fair agreement is observed between data and MC. However, the $\theta_\gamma$ distributions show a clearly excess of data at low $\theta_\gamma$ , which is also reflected in the distribution of $W$. For the rest of the distributions, the excess is smeared out. It is specially important to understand this excess since it is located in the low $W$ area which corresponds to the main region for the extraction of the DVCS signal.

A visual scanning of the events located in the region of the excess could help in the identification of any common characteristic of those events. A typical example of a low $\theta_\gamma$-data event is shown in figure 6.11 and, as can be seen, is a nice example of a DVCS candidate with the two clusters and an empty detector . All the events scanned were found to be similar to this one, the only common feature found in a fraction of them was the existence of small deposits of energy close to the photon candidate (also seen in figure 6.11). However such signature was not conclusive since most of these deposits were at the noise level. In the following sections, the different studies performed to understand the excess are reviewed.

## 6.3.3   Shower shape study

Neutral particles, such as $\pi^0$ and $\eta$, leave the same signal as photons in the detector, so they can be a potential source of background in the $\gamma$-sample . A way to identify them is using their shower shapes (see section 4.3). The clusters coming from those particles are mainly formed by the 2 $\gamma$'s in which they decay. Thus, their shower shapes are expected to be different from the ones of a cluster formed by a single photon. To investigate this contribution the shower shape variable, $f_{MAX}$ , which is defined by

$$f_{MAX} = \frac{\text{energy in the most energetic cell of the cluster}}{\text{total energy in the cluster}}, \qquad (6.1)$$
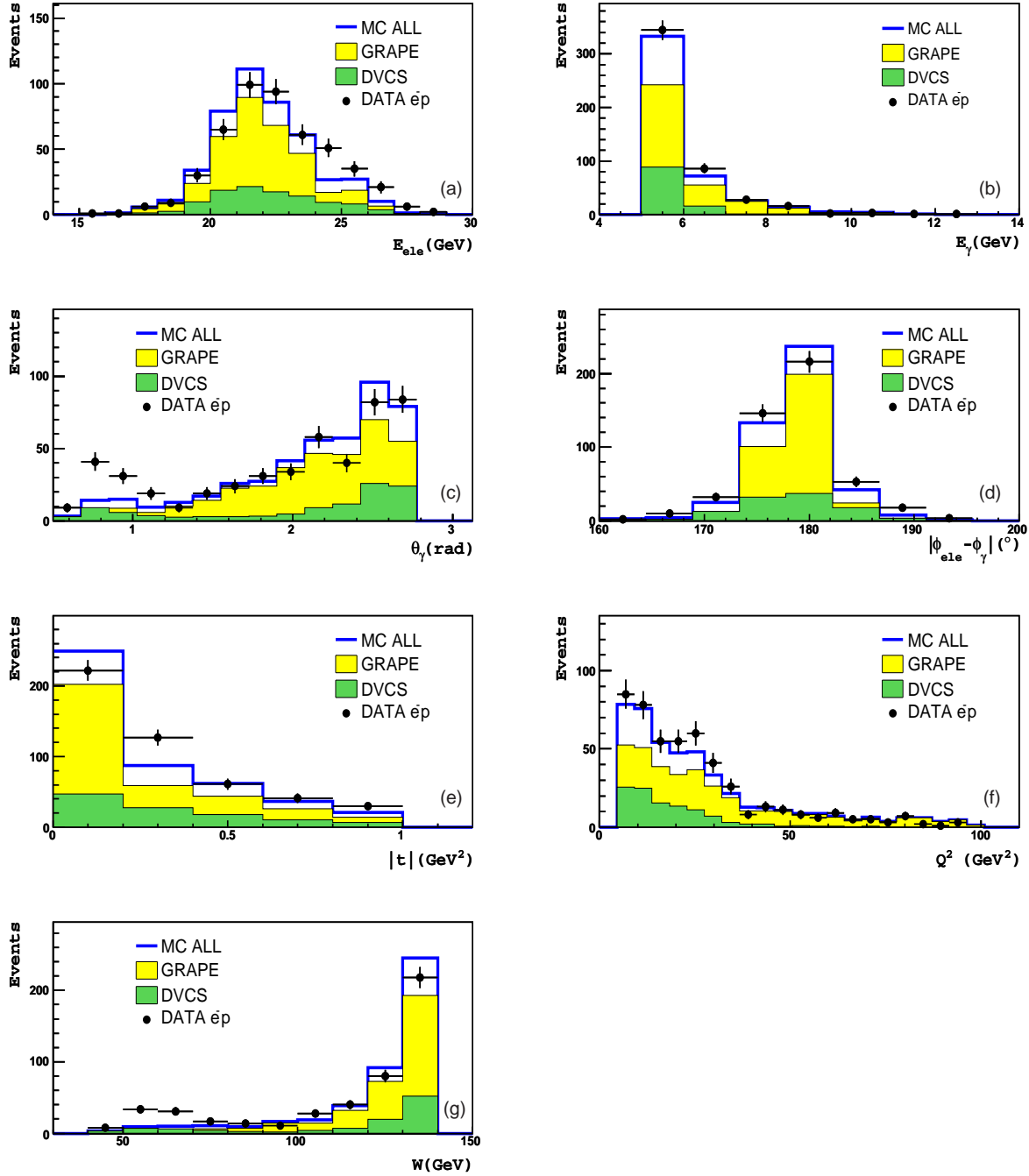
**Figure 6.9:**    γ-sample control plots for $e^-p$ :  data distributions of the energy of the electron (a), the energy of the $\gamma$ (b), the polar angle of the $\gamma$ (c), the coplanarity (d), the absolute value of $t$ (e), $Q^2$ (f) and $W$ (g) compared to the MC samples. MC histograms are normalized to the luminosity of the data.

was used.
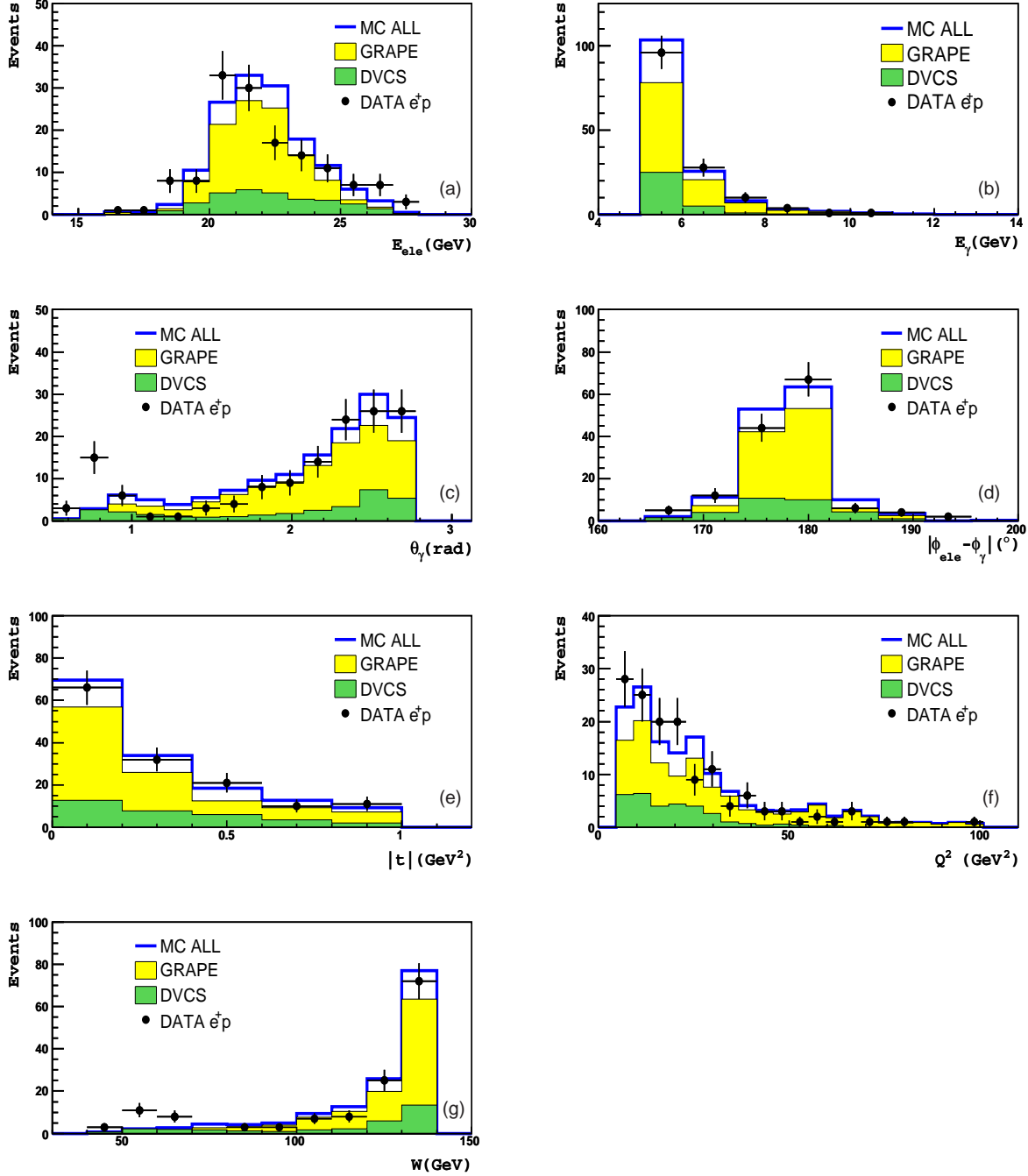
**Figure 6.10:** $\gamma$-sample control plots for $e^+p$ : data distributions of the energy of the electron (a), the energy of the $\gamma$ (b), the polar angle of the $\gamma$ (c), the coplanarity (d), the absolute value of $t$ (e), $Q^2$ (f) and $W$ (g) compared to the MC samples. MC histograms are normalized to the luminosity of the data.

The characteristic of the neutral meson background is analyzed using single-particle MC sample of $\pi^0$ ($\to \gamma\gamma$). The sample was generated with a flat $\theta$ angle

| Zeus Run 53242 Event 57841 | | | date: 11-02-2005 time: 16:13:20 | |
|---|---|---|---|---|
| E=32.6 GeV | $E_t$=11.1 GeV | E-$p_z$=53 GeV | $E_t$=0 GeV | $E_b$=0 GeV |
| $E_r$=-4.8 GeV | $p_t$=1.27 GeV | $p_x$=1.19 GeV | $p_y$=-0.437 GeV | $p_z$=-20.4 GeV |
| phi=-0.35 | $t_t$=-100 ns | $t_s$=-0.484 ns | $t_r$=0.14 ns | $t_g$=-0.0324 ns |
| $E_e^{SIRA}$=25.7 GeV | $\theta_e^{SIRA}$=2.94 | $\phi_e^{SIRA}$=0.24 | Prob$_e^{SIRA}$=0.999 | |
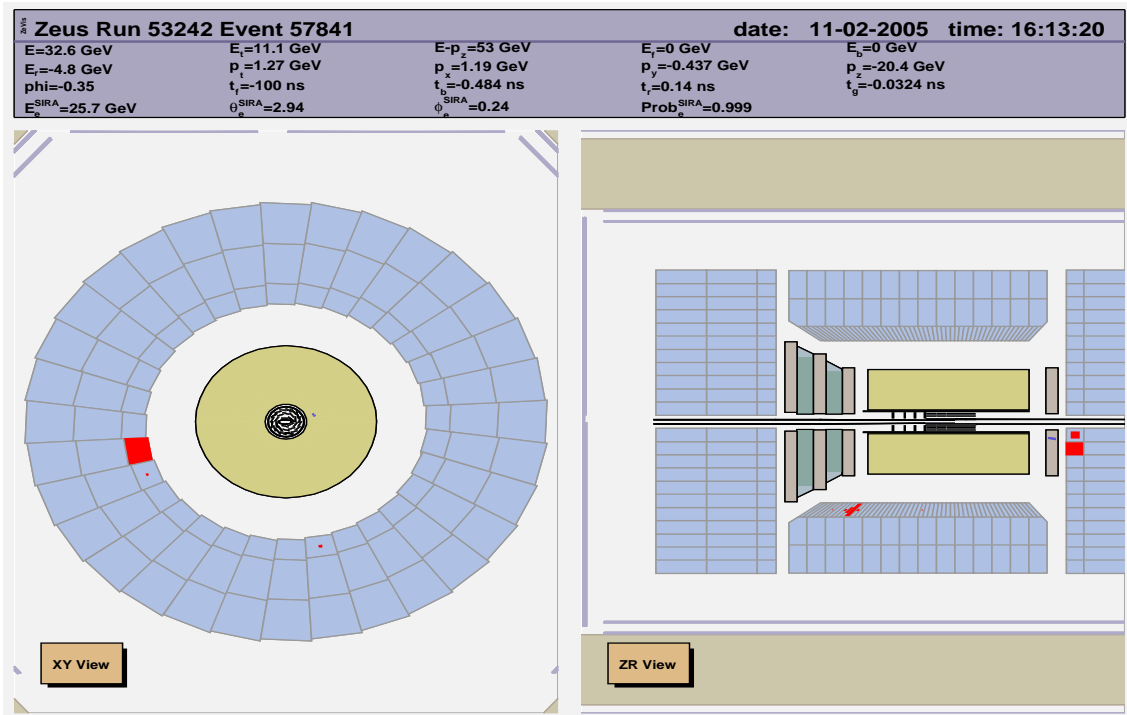
**Figure 6.11:** An example of a low $\theta_\gamma$ -data event in the $\gamma$-sample .

and with 2 GeV $<$ E$_{\pi^0}$ $<$ 6 GeV.

After the reconstruction, for all the events in the MC sample, only one electron candidate was found by the electron finder SINISTRA. Figure 6.13 (a) shows the generated energy of $\pi^0$ together with the reconstructed energy above 4 GeV. The reconstruction efficiency for $\pi^0$ in this range of energy is $\sim$25%. In a small fraction of events ($\sim$ 5%) it is possible to resolve the 2 $\gamma$'s from the decay considering the combination of the SINISTRA candidate and a *condensate* (see figure 6.12). The invariant-mass spectra for the SINISTRA candidate and the condensate is shown in figure 6.13(b). The region below 0.2 GeV corresponds to the mass peak of $\pi^0$ and thus to the correct identification of the two photons from the decay. The rest of the spectra is associated to condensates coming from noise. This distribution can be compared with the invariant-mass spectra for the $\gamma$-sample shown in figure 6.7 (left), where almost no events are seen in the region below 0.2 GeV. Figure 6.13 (c) and (d) show the polar angle and the $f_{MAX}$ distribution for the reconstructed $\pi^0$ , respectively. Regarding to the angular distribution, the RCAL region has less candidates reconstructed than the barrel part. This effect is due to the better tuning of the electron finder SINISTRA in the RCAL region which results in a better distinction between photons and $\pi^0$ in that area. The BCAL region presents a flat distribution with no signif-
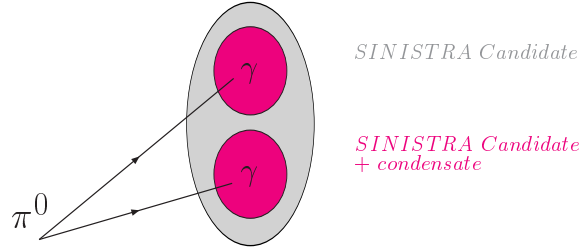
**Figure 6.12:** Schematic view of $\pi^0$ decay and the combinations to reconstruct the $\pi^0$ .

icant evidence of detector effects in any particular region. The $f_{MAX}$ distribution is flat with values in the range from 0.2 to 1.
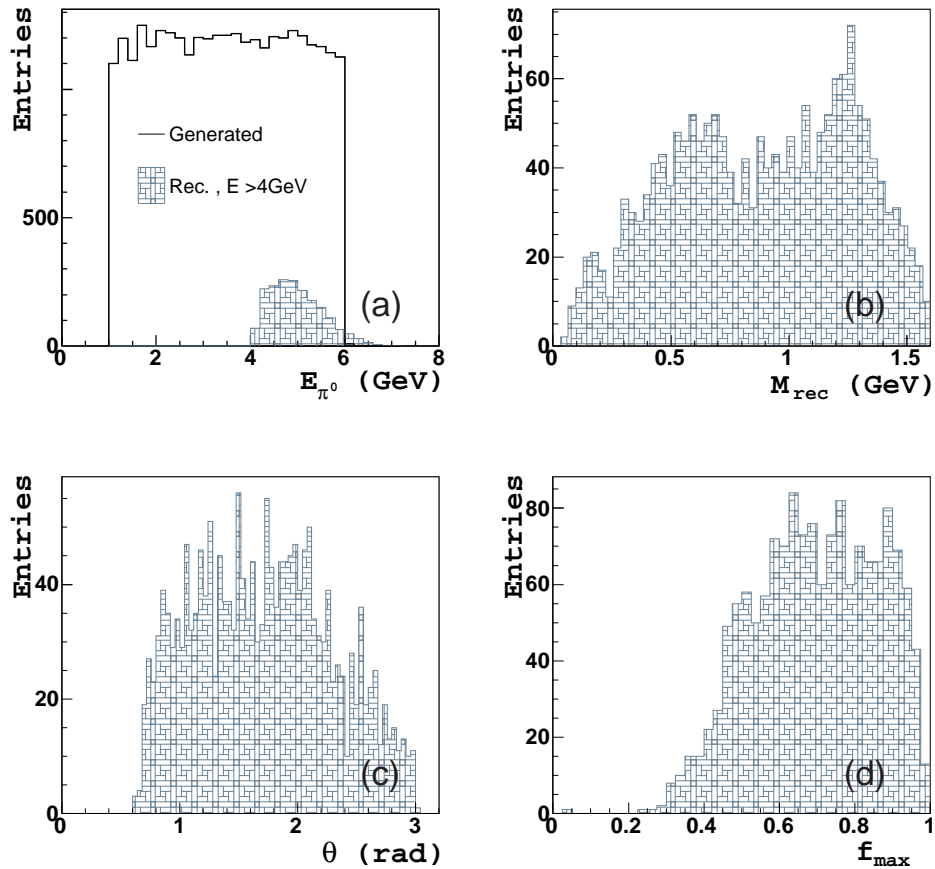


**Figure 6.13:** Generated and reconstructed energy (a), invariant-mass spectra (b), reconstructed polar angle (c) and $f_{MAX}$ distribution (d) for single-particle MC sample of $\pi^0$ .
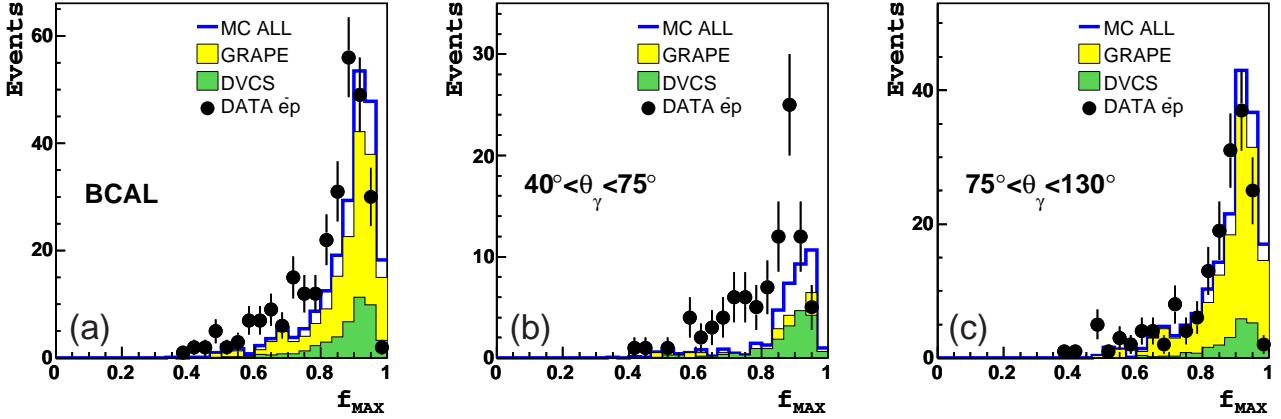
**Figure 6.14:** The $f_{MAX}$ distributions of the candidate 2 in the γ-sample for the whole BCAL region (a) and for 2 separated regions, (b) and (c).

Having seen the properties of $f_{MAX}$ for the $\pi^0$ , figure 6.14 shows the $f_{MAX}$ distributions of the candidate 2 in the γ-sample for two different regions in the BCAL: the low $\theta_\gamma$ region ($40° < \theta_\gamma < 75°$) and the high $\theta_\gamma$ region ($75° < \theta_\gamma < 130°$), and for the combination of these two which correspond to the complete BCAL region. MC histograms are normalized to the luminosity of the data. In the whole BCAL region, $f_{MAX}$ distributions in data and MC have very similar shapes, however a slight shift in the peak position is observed. The distribution for the high $\theta_\gamma$ region shows a good agreement between data and MC and, as seen before, the low $\theta_\gamma$ region exhibits an excess of data over MC predictions.

The shift in the peak positions was corrected. This effect is due to a missing correction factor to the energy of the single cells[5] from which the $f_{MAX}$ is calculated. The peak positions from data and MC in the high $\theta_\gamma$ region were obtained from the mean values of a Gaussian fit performed on the $f_{MAX}$ distributions. The difference between the peak positions

$$\langle MC \rangle - \langle Data \rangle = 0.93 - 0.90 = 0.03, \qquad (6.2)$$

was used to shift down the MC $f_{MAX}$ distributions. The correction factor was applied for both regions in the BCAL since no differences were found in the MC behavior for the low and high $\theta_\gamma$ regions (see figure 6.16).

In figure 6.15, the $f_{MAX}$ data distributions are compared to MC after the correction, where the total MC contribution has been normalized to the number

---

[5]The energy corrections explained in section 4.3.1 were applied to the total energy of the cluster.

of data. Comparing the distributions between the two different region of the BCAL it can be seen that the data in the low $\theta_\gamma$ region appears to have a small plateau at $\sim 0.7$ which is not seen for the data distribution in the high $\theta_\gamma$ region of the BCAL. Such a plateau could accommodate some background coming from $\pi^0$ . Since the high $\theta_\gamma$ region shows a very good agreement between data and MC, it can be assumed that this region is dominated by clusters that have their origin in single photons.
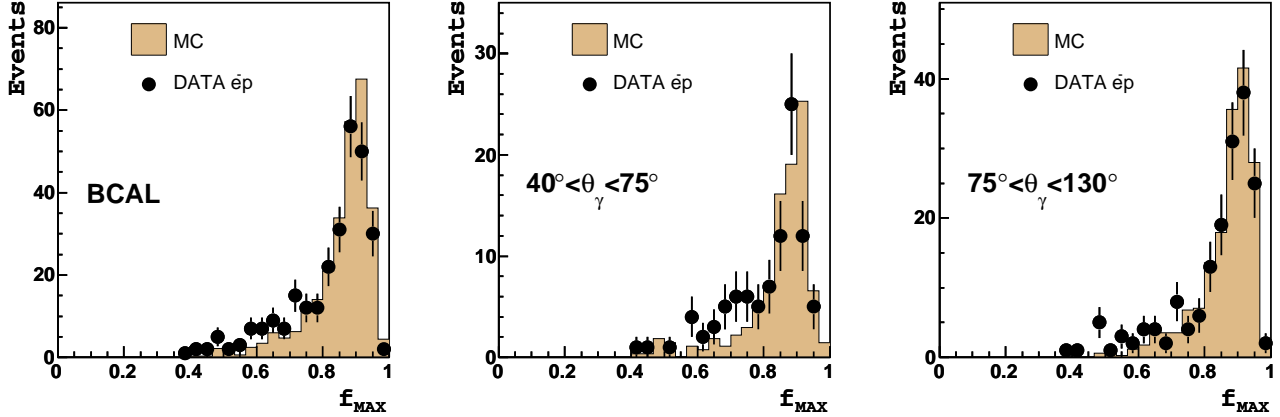


**Figure 6.15:** The $f_{MAX}$ distribution (lower) after being corrected (see text).

Figure 6.16 shows a direct shape comparison between the $f_{MAX}$ distributions in the two BCAL regions for data (left) and MC (right). MC-MC comparison shows that the behavior of the $f_{MAX}$ distribution is the same in both regions of the BCAL. In the case of the data-data plot, the shapes of the distributions are very similar and the small plateau mentioned before is covered by the statistical uncertainty and therefore not significant. However, it is visible that the distributions are shifted. This fact could be due to an inhomogeneous distribution of dead material in front of the BCAL. With the arguments presented here, it can be concluded that it is very unlike that background coming from neutral particles could account for the excess of data observed in the low $\theta_\gamma$ region.

## 6.3.4   Presampler energies

Another way for checking the contamination from neutral particles is looking at the energies deposited in the Presampler detectors, specifically the BPRES (see section 2.2). The multiple-photon signal left by the decay of neutral particles will produce a higher response in the BPRES than a single-photon signal. Figure
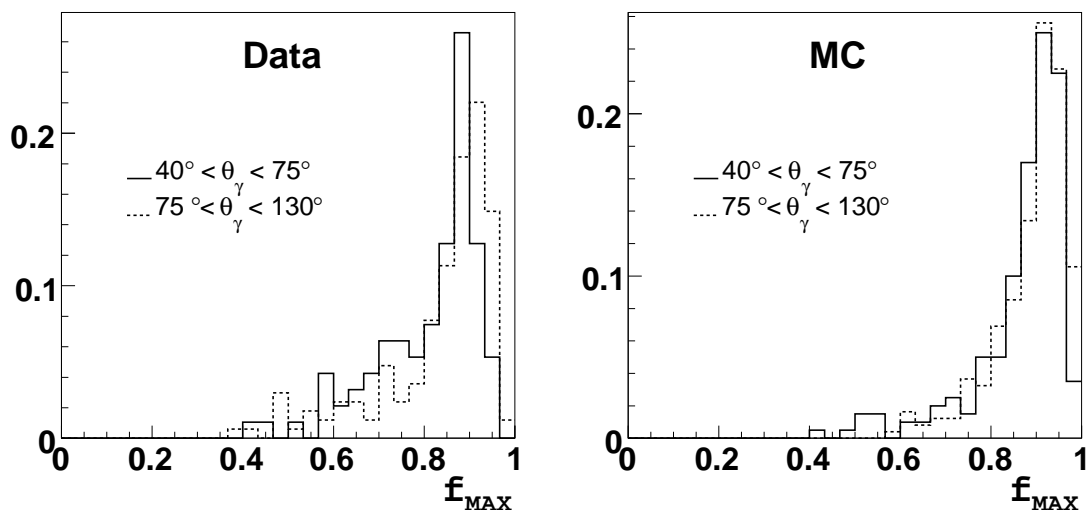
**Figure 6.16:** Shape comparison between the $f_{MAX}$ distribution in two different ranges of $\theta_\gamma$ for $e^-p$ data (left) and MC (right).
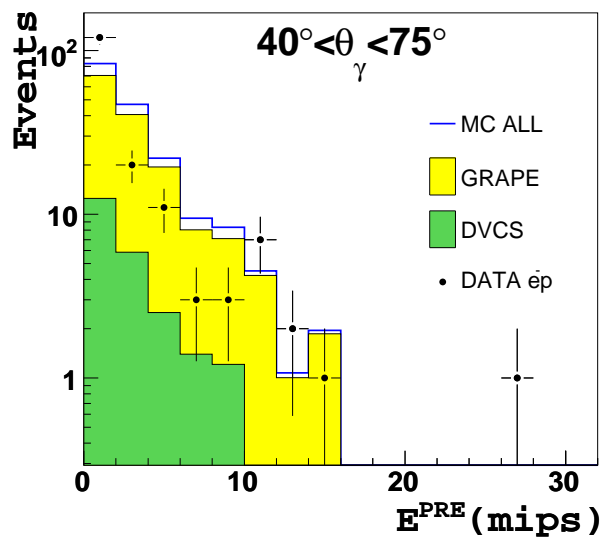


**Figure 6.17:** BPRES energy for the $\gamma$-sample at low $\theta_\gamma$ values.

6.17 shows the BPRES energy for the $\gamma$-sample in the region where the excess is observed. The distribution shows that all the excess of data is concentrated close to 0 confirming the low probability of having $\pi^0$ or $\eta$ contamination. Moreover, preshowering photons can be also discarded for the same reason.

### 6.3.5  $\theta_\gamma$ study

Since from the $\gamma$-sample control plots, the excess was more visible in the $\theta_\gamma$ distributions (see figures 6.9 and 6.10, (c)), it might be that the excess is related to a problem in the $\theta_\gamma$ calculation. The majority of the events in the $\gamma$-sample configuration does not have a track, therefore the $z_{vtx}$ is assumed to be at 0 and this could introduce a bias in the determination of $\theta_\gamma$ .
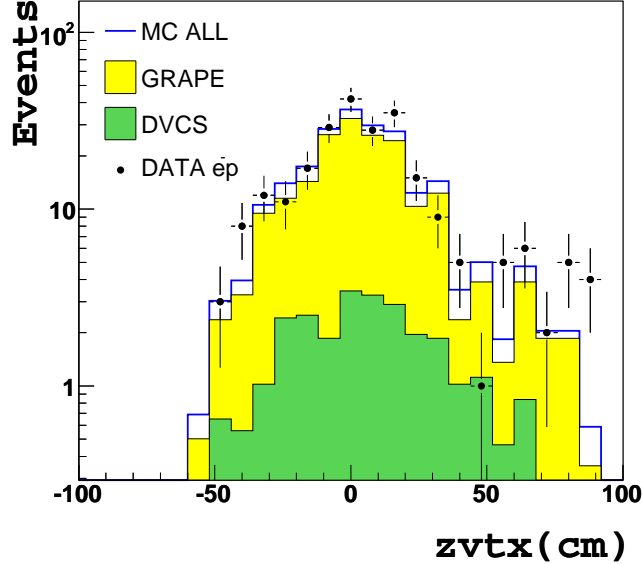


**Figure 6.18:** $z_{vtx}$ distribution in data and MC for events with a track in the $\gamma$-sample with loose cuts (see text). MC histograms are normalized to the luminosity of data.

An approach for studying this effect consists in taking the fraction of $\gamma$-sample events with a track and recalculate $\theta_\gamma$ for these events assuming $z_{vtx} = 0$. Only 103 events in the $e^-p$ $\gamma$-sample have a track associated to the scattered electron, to increase these numbers the following criteria were used:

  - Energy cut for candidate 2 was lowered to 4 GeV.

  - No cut on $t$.

  - The momentum cut of the track was lowered to 0.150 GeV.

After this selection a factor of 2.1 in the number of events was gained.

Figure 6.18 shows the distribution of the $z_{vtx}$ for this sample. The $z_{vtx}$ distribution has a reasonable shape taking into account the poor statistics and
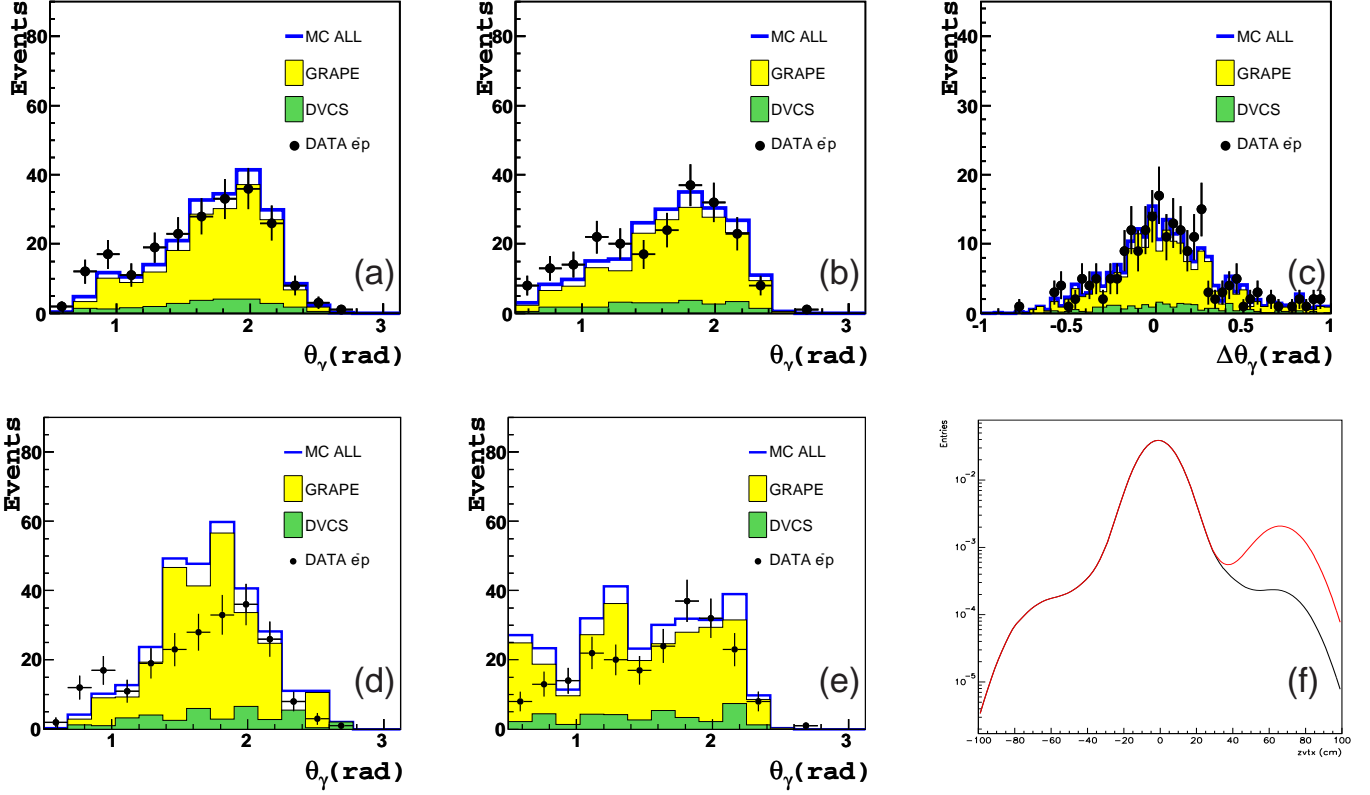
**Figure 6.19:** Distributions for events with track in the $\gamma$-sample of $\theta_\gamma$ (a), $\theta_\gamma$ calculated assuming $z_{vtx} = 0$ (b), the difference $\Delta\theta_\gamma = \theta_\gamma - \theta_{\gamma, z_{vtx}=0}$ (c), $\theta_\gamma$ after the reweighting of MC samples (d), $\theta_\gamma$ calculated assuming $z_{vtx} = 0$ after the reweighting of MC samples (e). Reweighting function (f) for the nominal (black line) and enhanced (red line) $z_{vtx}$ distribution.

also the low quality of the tracks used to find the vertex. These are tracks that go very rear, usually outside the acceptance of the CTD. On this sample, $\theta_\gamma$ is calculated again for each event assuming $z_{vtx} = 0$. The results are shown in figure 6.19 upper plots, where (a) corresponds to the distribution of $\theta_\gamma$ for the nominal vertex position, (b) shows the $\theta_\gamma$ calculated with $z$ of the vertex at 0 and (c) the difference between both polar angles.

The recalculated $\theta_\gamma$ distribution is very similar to the original one and it does not show a particular enhancement in any $\theta_\gamma$ range, which is understandable since the $z_{vtx}$ is approximately symmetric with respect to 0. Moreover the behavior of data is reproduced by the MC simulation.

However, as it is seen in the $z_{vtx}$ distributions, right plot in figure 6.18, there is a contribution from interactions of the satellite bunches ($z_{vtx} \sim 70$ cm). These events, situated in the $+z$ direction, produce lower $\theta_\gamma$ after the shift to $z_{vtx} = 0$. It is possible to check what would be the effect if the events in the satellite

bunches were underestimated. For that, MC samples were reweighted with a modified vertex distribution which contains a higher contributions of the satellite bunches [111] (see figure 6.19 (f) ). After the MC reweighting, the original and shifted $\theta_\gamma$ distributions are shown in figure 6.19 (d) and (e), respectively. The MC distributions of $\theta_\gamma$ exhibits a general distortion and in the shifted distribution an increase of events at low $\theta_\gamma$ is observed.

In order to see how large could be the contribution of the satellite bunches, two MC samples of Bethe-Heitler events were compared. One of them was produced with a generated vertex distribution at $z_{vtx} = +70$ cm and the other with the nominal position. Figure 6.20 shows the $z_{vtx}$ distributions from both samples. Both topology, e-sample and $\gamma$-sample are considered. The acceptance for the shifted sample is $\sim 1.4$ higher than the nominal one. From the distributions it can be seen that the satellite contributions have a reconstructed vertex at the expected position, around 70 cm, while only a small fraction ($\sim 8\%$) is reconstructed with a vertex at $z_{vtx} = 0$. From here, it can be concluded that the contribution of BH satellite bunch events should be small and, since the DVCS cross section is smaller than the BH, any possible contribution from DVCS satellite bunch events should be even smaller. Also any effect associated to this kind of contributions should appear in the e-sample, which has been not observed.
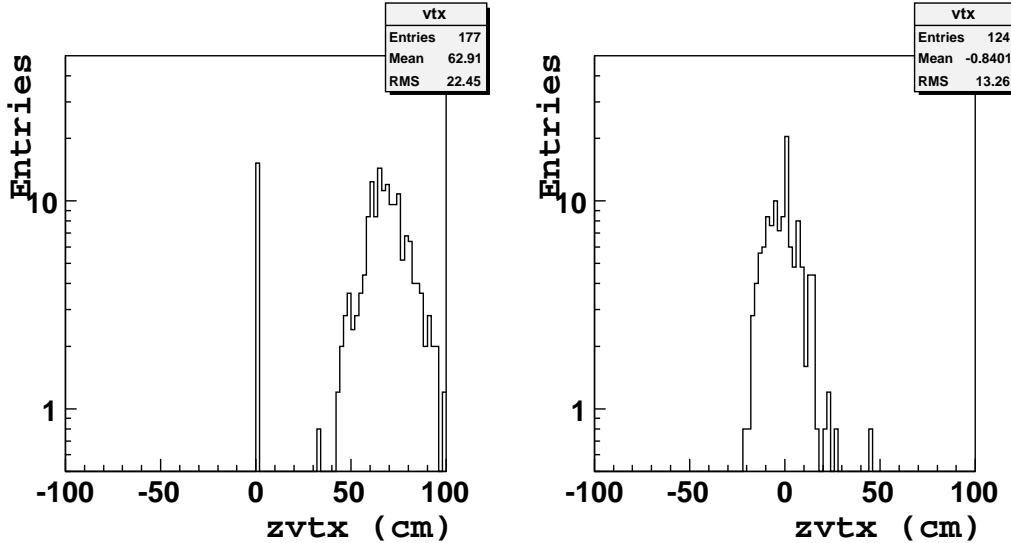


**Figure 6.20:** MC distributions of reconstructed $z_{vtx}$ for a sample with the generated vertex centered at $z = +70$ cm (left) and at $z = 0$ cm (right). See text.

In addition, a determination of the $z_{vtx}$ for each event was done using the conservation of the transverse momentum and geometrical arguments. This

method was tested using the data of the e-sample and further applied to calculate the $z$ position of the vertex for the γ-sample events. Figure 6.21 shows the nominal $z_{vtx}$ distribution (solid line) in comparison with the one obtained by the previous arguments (dashed line) for data events in the e-sample (left) and γ-sample (right). The method has not been tested in depth and features like the tails produced are not understood. Nevertheless the distributions obtained exhibit the Gaussian shape expected. So the aim of these distributions is only the demonstration that the γ-sample events are coming from a region close to the interaction point and therefore most likely from a $ep$ interaction.
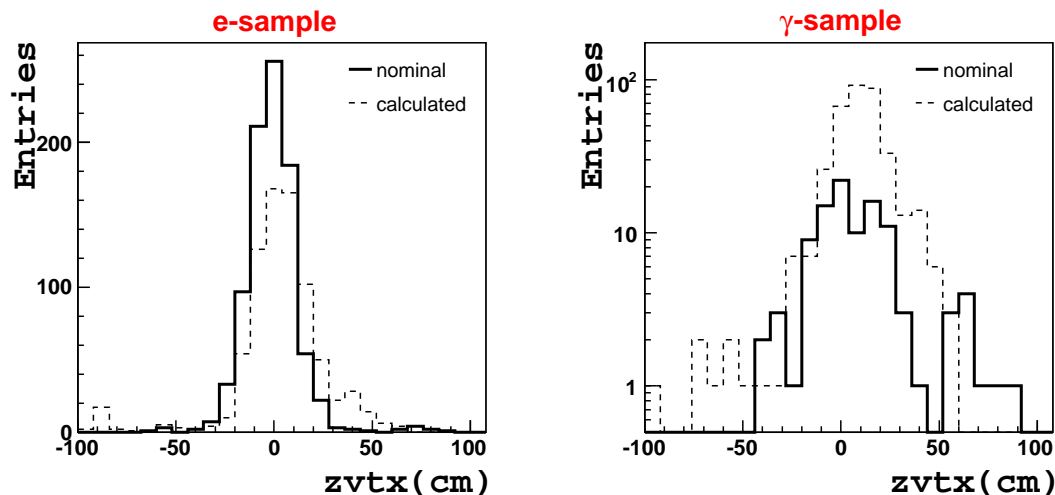


**Figure 6.21:** Distributions of the nominal $z_{vtx}$ (solid line) and the one calculated through the conservation of transverse momentum and geometrical arguments (dashed line) for data events in the e-sample and γ-sample .

## 6.3.6   Other checks

Further sources of background and hypothesis that could explain the excess of data were checked:

- Data quality checks.
  The runs which contain the data events in the excess region were taken over the whole running period. Also the events in excess region do not originate from the calorimeter hot cells. Moreover, the specific CAL data quality monitoring was checked but no indications of malfunctioning of the detector were found.

- Elasticity cut.
  Since one of the features observed during the scanning of the data events in the excess region was the presence of cells with small energies (see figure 6.11), the elasticity cut was revisited. Instead of applying a cut on the energy of individual cells, a test using the total energy deposited on the cells was done. Figure 6.22 shows the total EMC (first row) and HAC (second row) energy for different sections of the calorimeter (in columns) for the $\gamma$-sample . The third and fourth rows show, in the same way, the correlation between total energy and number of cells. Cutting on the total energy of cells results in a overall reduction of events that does not affect specifically the excess region.

- Super-cal crack events.
  The regions between the 3 calorimeter sections, FCAL to BCAL and BCAL to RCAL, are called super-cal cracks. These regions are known not to be perfectly described by the MC simulation and for example, the efficiency of the electron finders is lower in these regions of the CAL [96]. Less than 1% of the events in the $\gamma$-sample was located in the super-cal cracks and the effect in the excess region was minimal.

## 6.4   Beam induced background

Electron and proton interactions with the residual gas in the beam pipes are common sources of background. Proton-beam gas events are effectively rejected by the timing cuts at the trigger level and/or the $E - p_z$ cut. On the other hand, overlays of off-momentum electrons can fake a DIS signal and they can not be identified using timing. An estimation of the contribution of such events can be done using electron-only (e-only) runs[6].

From the background studies carried out after the HERA upgrade, a MC simulation for off-momentum electrons was available [102]. If it is possible to get a normalization of the MC, this could be used directly to subtract statistically the contribution of off-momentum electrons . However this MC simulation is very limited and its performance was checked by doing a comparison with e-only data runs.

The sample selected for the comparison satisfies these criteria:

---

[6]Only electron beam is operating in the machine
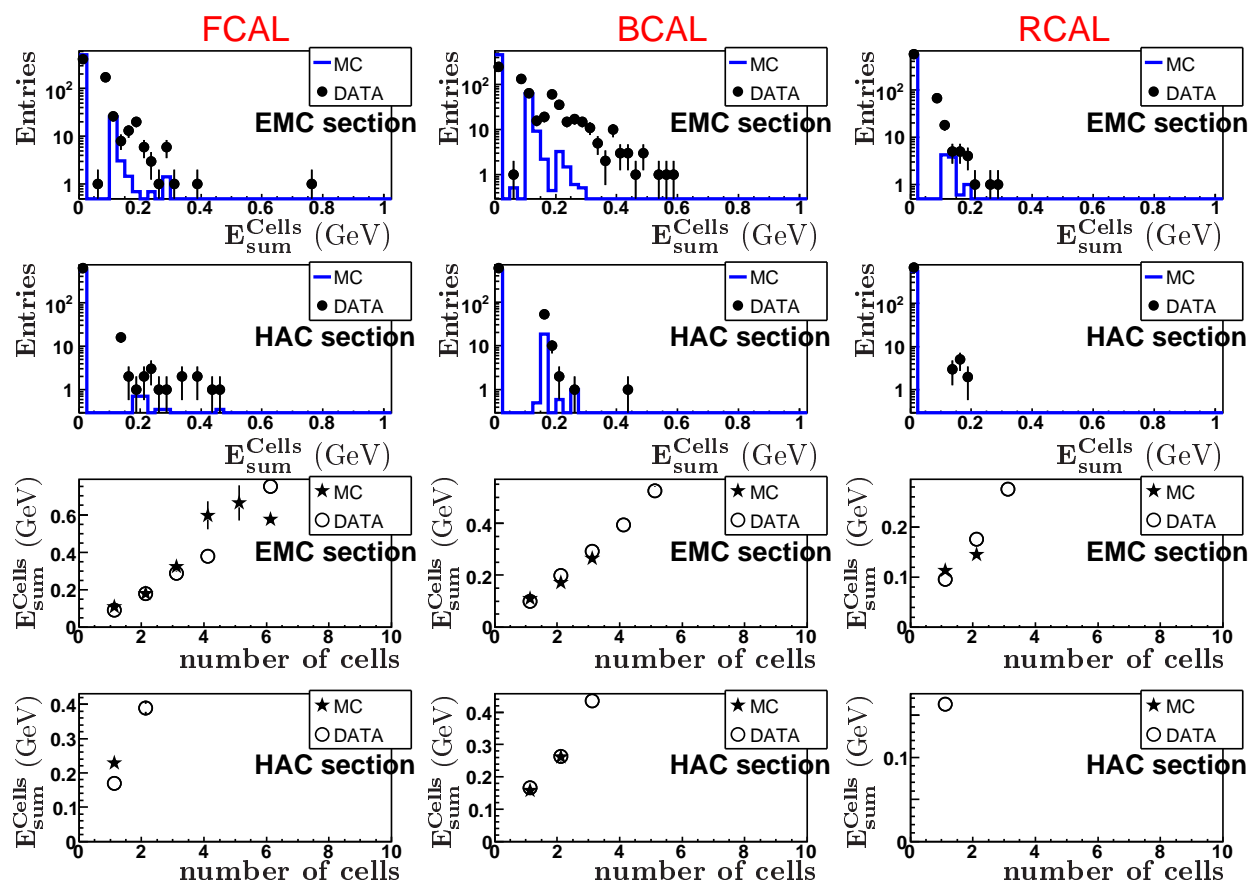
**Figure 6.22:** The distributions of the total energy deposited in cells not belonging to the candidates in the γ-sample are shown in the first (second) row for the EMC (HAC) sections located, from left to right, in FCAL, BCAL and RCAL. The correlation between the total energy and number of cells is shown in similar way in the last two rows.

- E-only runs were required to have a correct C5 timing in order to be able to use CAL information.

- At least one electron candidate. For all the e-only runs analyzed, no event with more than one candidate was found.

- Electron probability greater than 0.6.

- Energy of the candidate > 5 GeV.

- $Q^2_{ele} > 3$ GeV$^2$.

- Box-cut of $14 \times 18$ cm$^2$.

Figure 6.23 shows the energy of the electron candidate for 5 different e-only runs compared to the background MC. MC histograms are normalized to the

number of data events. The runs are ordered in time; the first one corresponds to the earliest period of data taking and a good agreement between data and MC is observed. For the rest of the runs, the MC is not describing the data. A characteristic peak at $\sim 15$ GeV, corresponding to the off-momentum electrons , is not reproduced by the MC. Differences between earlier and later runs could be
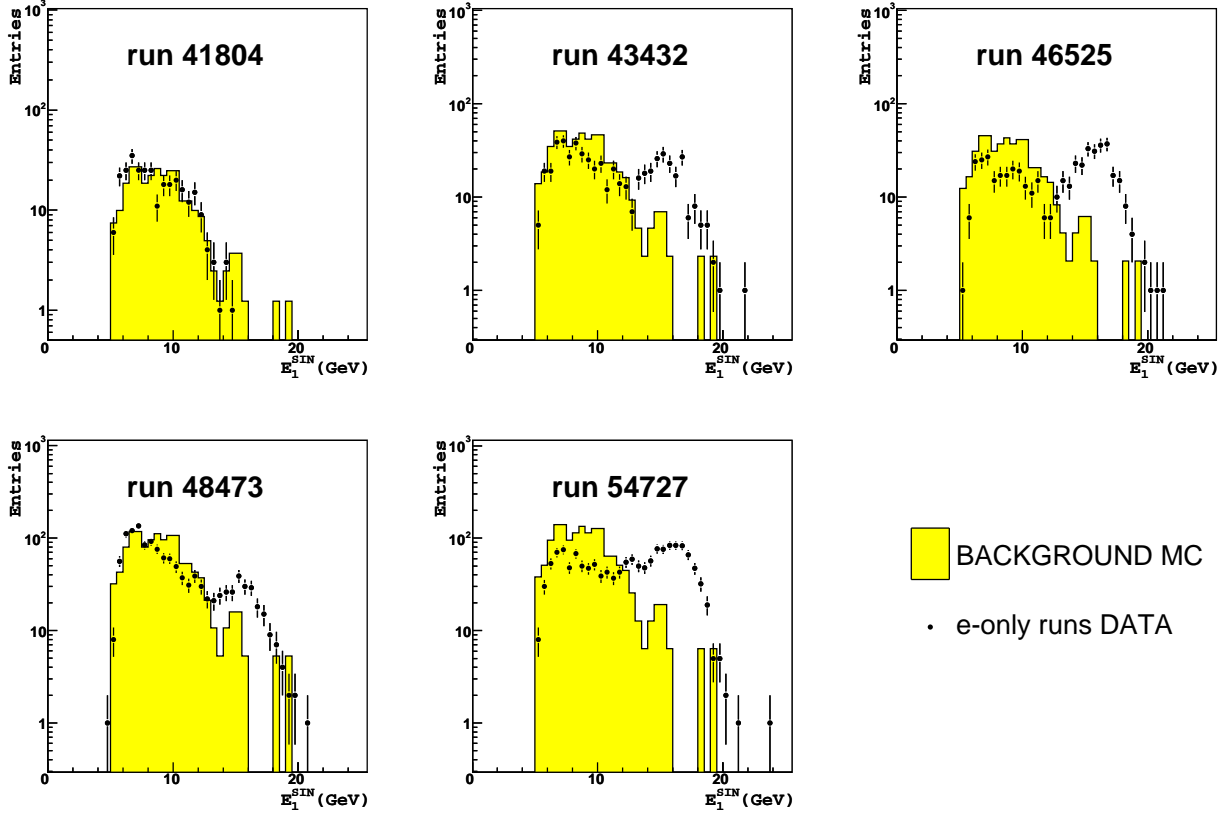


**Figure 6.23:** Examples of the energy distribution of the SINISTRA candidate for e-only runs data (dots) compared with a background MC (histograms). MC histograms are normalized to the number of data.

produced by different vacuum and beam conditions and also by the further tuning of the machine as the data taking period was developing. Thus, the use of this MC for a direct determination of the background contribution is not possible.

However, using the e-only runs it is possible to calculate a background rate coming from off-momentum electrons . For this, the FLT slot 38 was used. Slot 38 triggers on RCAL energies[7] and it is mainly dominated by beam-gas events. This slot is available in both, e-only and physic runs, and even though it is prescaled due to the high rate, it can be used to obtain an estimation of a cross section for these overlay events.

---

[7]Including the first inner ring but with a 5 GeV threshold.

The events in the e-only runs are triggered by a SRTD related slot [8] with a prescale factor of 64. Counting the number of events that survive the selection explained above, $N^{sel}$, the number of events taken by the slot 38 is

$$N^{slot38} = 64 N^{sel} \frac{\text{rate of slot 38}}{\text{rate of slot SRTD}}. \tag{6.3}$$

In this way, $N^{slot38}$ is the number of overlay-events coming from off-momentum electrons in a DIS selection. From here, the rate, $R$, for this contribution is calculated using the active time and the given rate of slot 38 in each e-only run. This was done in two different ways, as a check of consistency:

1. averaging method:

$$R = \frac{\sum_i \frac{N_i^{slot38}}{rate_i^{slot38}} \, w_i}{\sum_i w_i}, \tag{6.4}$$

   where $w_i = (\text{active time})_i \times (\text{rate}_i^{slot38})$ and the index $i$ runs over all the e-only runs.

2. summing method:

$$R = \frac{\sum_i N_i^{slot38}}{\sum_i \text{active time}}, \tag{6.5}$$

   where the index $i$ runs over all the e-only runs.

The rates obtained with the averaging and the summing methods are shown in figure 6.24, where the same tendency is observed for both methods. The top plot shows the rates as a function of an energy cut for the nominal $Q^2$ value used in the selection. In the bottom plot, the rates are shown as a function of a $Q^2$ cut for $E > 5$ GeV. In both cases, the rates were calculated with (triangles) and without (squares) the electron identification probability cut. As the energy increases the rates are decreasing, becoming almost 0 for energies of the candidate above 13 GeV. As a function of $Q^2$, the rates also decrease until $Q^2 = 6$ GeV$^2$ where they seem to reach a constant value.

Assuming an upper limit of 0.005 Hz and a lower limit[9] of 0.001 Hz, an estimation of the cross section for background events was done using the following

---

[8]The slot used the information from the SRTD timing to select or reject events.

[9]This value would correspond to the rates obtained for electron energies above 10 GeV or $Q^2$ greater than 10 GeV$^2$.
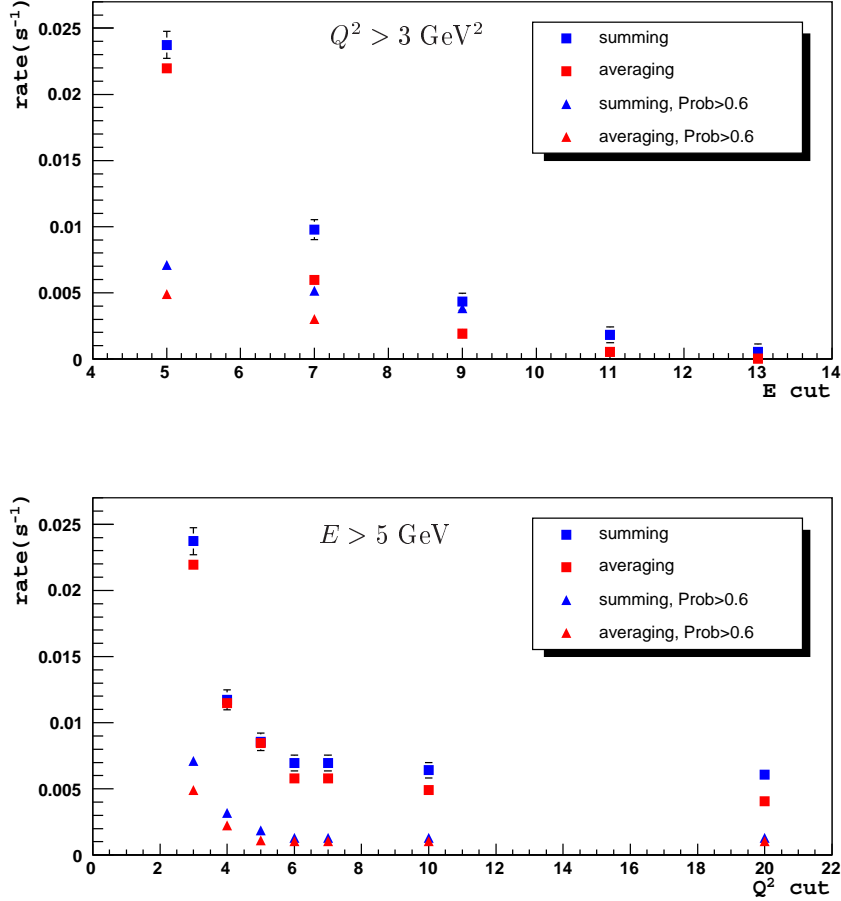
**Figure 6.24:** Off-momentum electron rates in e-only runs estimated for the slot 38 as a function of the energy of the electron (top) and $Q^2$ (bottom) cut. As the energy and the $Q^2$ increase the rates become smaller. The effect of using a probability requirement is shown with the color code, also the 2 different methods to estimate the rates are shown (see text).

formula:

$$\sigma_{bkg} = R \times \left(\frac{\text{Rates of slot 38}}{\mathcal{L}}\right)_{\text{physic runs}}. \tag{6.6}$$

The results as a function of the years are shown figure 6.25. Note that e-only runs are usually taken with different background and beam conditions respect to physic runs. This fact might affect the extrapolation of slot 38 rates from e-only to the physic runs.

It can be concluded that the possibility of overlays coming from off-momentum electrons is small and as it has been shown that, with the selection criteria of a typical DIS analysis (scattered electron with energies above 15 GeV), the contribution is negligible. For the DVCS analysis no contribution is expected since no
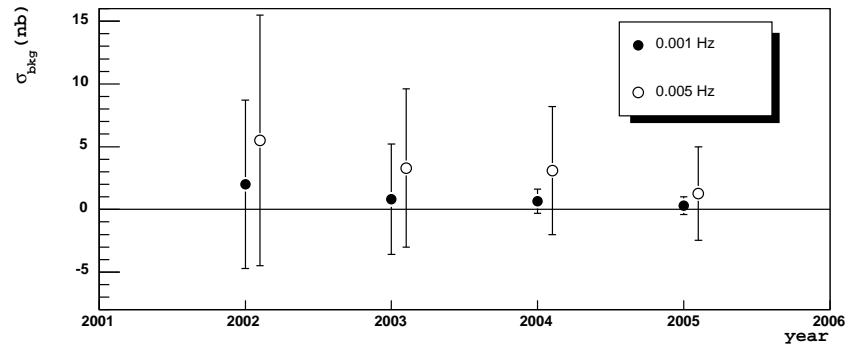
**Figure 6.25:** Estimated cross section for off-momentum overlay events for different year. The solid (hollow) dots represent the cross section calculated for a $R$=0.001 (0.005) Hz.

event was found in the e-only runs with more than one candidate.

# Bethe-Heitler data analysis

This chapter describes the e-sample which will be used to measured Bethe-Heitler cross sections. The sample analyzed here corresponds to the high statistic sample: 2004-2005 $e^-p$ data.

## 7.1 Definition of the kinematic region

According to the e-sample topology (see section 5.1), the scattered electron is the electromagnetic candidate found at lower $\theta$ w.r.t. the proton beam (the foward direction), which is referred to as candidate 2. In contrast to the analysis of the e-sample within the DVCS context (see section 6.1), the "true" kinematic variables are calculated and used here, i.e, the kinematic variables are calculated using the electron scattered.

The limits which define the kinematic region are:

- **230 GeV < W < 310 GeV**

- **20 GeV$^2$ < Q$^2$ < 1000 GeV$^2$**

- **|t| < 1 GeV$^2$**

## 7.2 Background

The background contributions to the e-sample have been presented in section 6.2.1. The main contributions correspond to dilepton production and proton-dissociative BH.

The amount of contamination from the dilepton process has been determined using the wrong-charge data sample. The events that belong to this sample have the same topology as the e-sample but with a positive charged track

associated to the scattered electron. This contribution correspond to 5% of the e-sample. Dilepton production, $ep \rightarrow e'e^+e^-p$, contribute to the wrong-charge sample since in the final state, it contains a opposite-charged electron with respect to the electron beam.

Figure 7.1 shows the distributions of the energy of the candidate 1 (higher $\theta$) and candidate 2 (lower $\theta$) for events belonging to the wrong-charge sample compared with the MC prediction for elastic and inelastic dilepton processes. The excess of data events over the MC predictions at small $E_1$ ($\sim 15\%$) could be attributed to the contribution from the diffractive $J/\psi(\rightarrow e^+e^-)$ production [104].

Assuming that the amount of events in which the right- or wrong-charge final state lepton are detected are the same, the wrong-charge sample can be used to subtract this kind of background. The advantage of using the wrong-charge sample instead of the dilepton MC predictions is that one does not depend on the MC simulation and the subtraction include the possible contributions from $J/\psi(\rightarrow e^+e^-)$ and other unidentified backgrounds. As explained in section 8.3, the uncertanty of this background estimation will be included in the systematic errors of the cross sections.
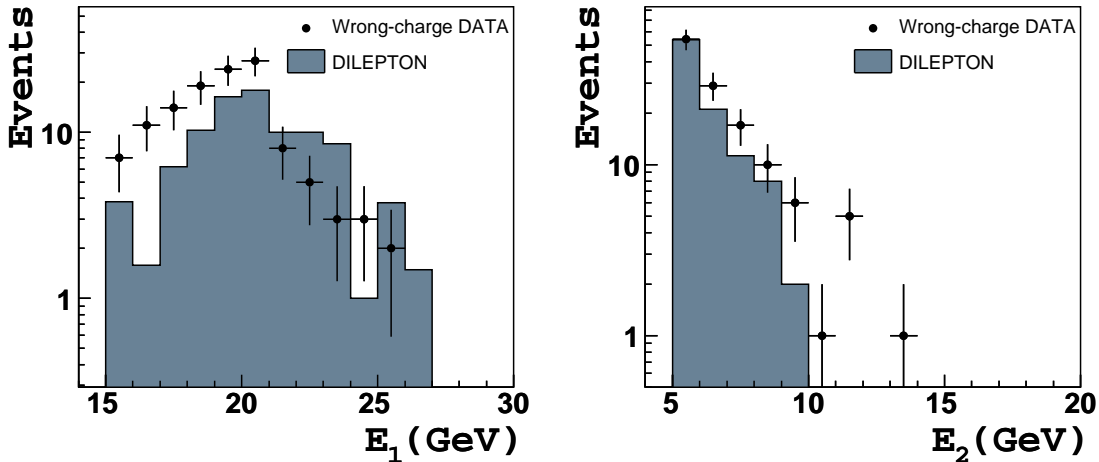


**Figure 7.1:** Distributions of the energy of the candidate 1 (left) and 2 (right) for $e^-p$ wrong-charge data events compared with the dilepton MC predictions.

**Proton-dissociative background**

The contribution of the inelastic background is estimated following the procedure explained in section 6.2.1. The fraction of inelastic events obtained with the

adjustment of the coplanarity distribution was $(23.2 \pm 5.6)\%$ in comparison to the MC expectation of 21%.

## 7.3  Data and MC comparison

The comparison between the data and MC distributions for the e-sample events after the selection detailed in chapter 5 is shown in figure 7.2. Also events with the candidates located in the super-cal crack[1] areas were rejected.

In each of the plots, the dots represent the data events after the subtraction of the wrong-charge events which are show as triangles. The histograms shown the GRAPE MC (elastic and inelastic) contribution normalized to the remaining data events after the subtraction of the wrong-charge sample.

Overall the shapes of the distributions are well described by the MC. MC distributions are reweighted in order to fit the electron polar angle data distribution. Only small improvements are observed. An additional cut on the transverse momentum of the electron, $p_{T,e} > 1.5$ GeV was required due to the not good description of the simulation for the low $p_{T,e}$ region. The final control distributions are shown in figure 7.3.

### $X$ and $Y$ position of the vertex

During the 2004-2005 data taking period, the $X$ position of the beam was changed. As it can be seen in figure 7.4 the data (dots) distribution of the $X$ position of the vertex (left) has a two peak structure which corresponds to the different positions of the beam. In the MC (histogram), there was only one vertex position available for the simulation. The peak position for the $Y$ component of the vertex (right plot in figure 7.4) is described by the MC, only the spread in $Y$ is large in the MC by about 0.5mm.

The changes in vertex position could deliver differences in the acceptance. The $e^-p$ data sample was divided in two subsamples which correspond to the time periods with a stable position of the vertex:

- $X_{vtx} = 1.32$cm, runs from 52258 to 54500, $\mathcal{L}_{X_{vtx}=1.32} = 47.1\text{pb}^{-1}$.

- $X_{vtx} = 1.25$cm, runs from 54500 to 57123, $\mathcal{L}_{X_{vtx}=1.25} = 88.8\text{pb}^{-1}$.

---

[1]R-BCAL crack:$-104$ cm $< Z < -98.5$ cm, F-BCAL crack: 164 cm $< Z < 174.5$ cm.

The number of data events selected for each of the subsamples was divided by the corresponding luminosity

$$\frac{no.\ of\ data\ events\ with\ X_{vtx} = 1.32}{\mathcal{L}_{X_{vtx}=1.32}} = \frac{1058}{47.1} = 22.5pb$$

$$\frac{no.\ of\ data\ events\ with\ X_{vtx} = 1.25}{\mathcal{L}_{X_{vtx}=1.25}} = \frac{2010}{88.8} = 22.6pb \qquad (7.1)$$

resulting in very similar numbers. Thus, the selection efficiencies are found to be rather independent of the vertex position and the differences between data and MC are neglected.
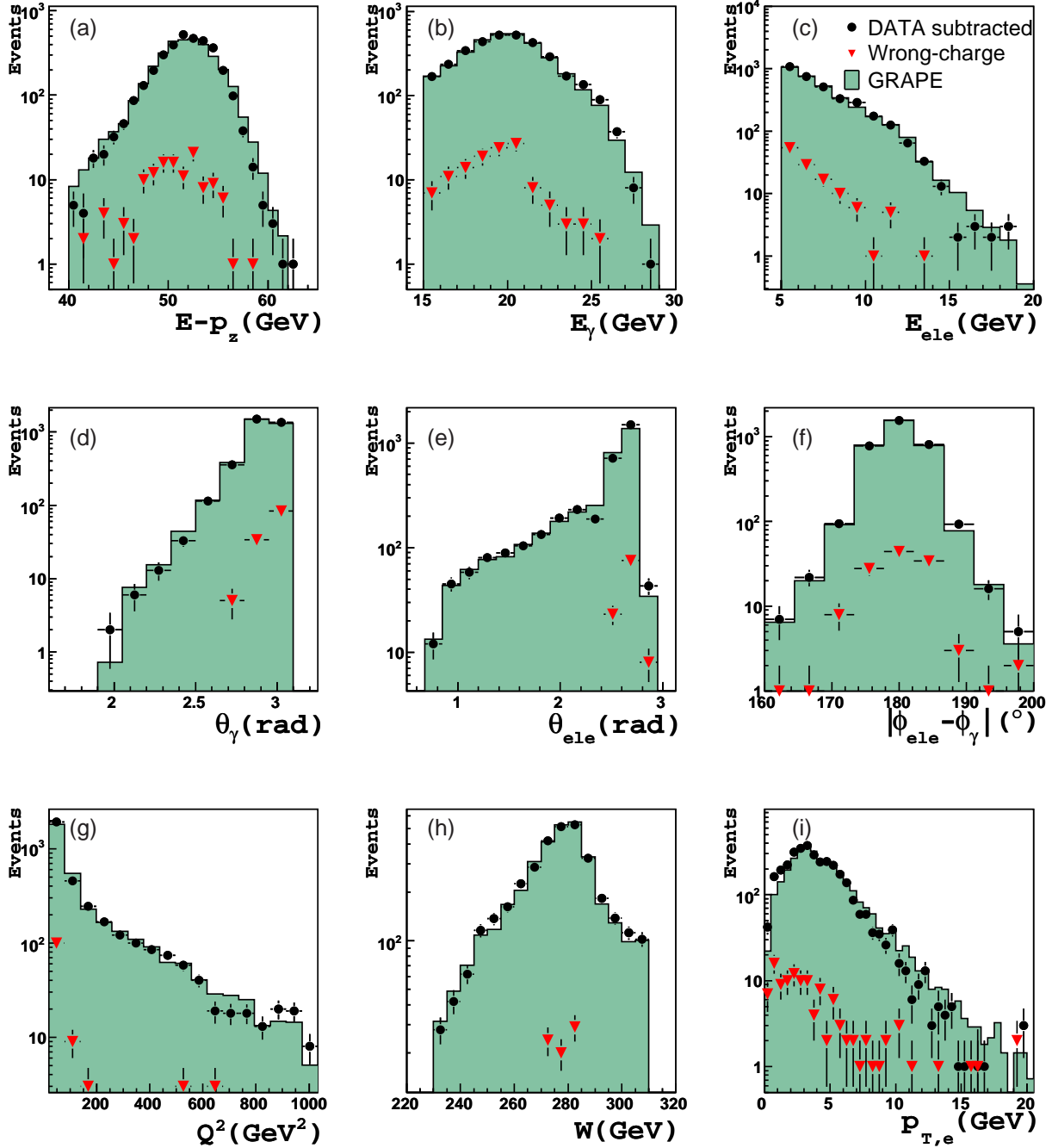
**Figure 7.2:** e-sample control plots for BH cross section measurement : data and MC distributions of $E - p_z$ (a), the energy of the $\gamma$ (b), the energy of the electron (c), the polar angle of the photon (d) and of the electron (e), the coplanarity (f), $Q^2$ (g), $W$ (h) and $p_{T,e}$ (i). The dots are the data events after the subtraction of the wrong-charge events which are shown as triangles. The histograms shown the GRAPE MC contribution normalized to the remaining data events after the subtraction.
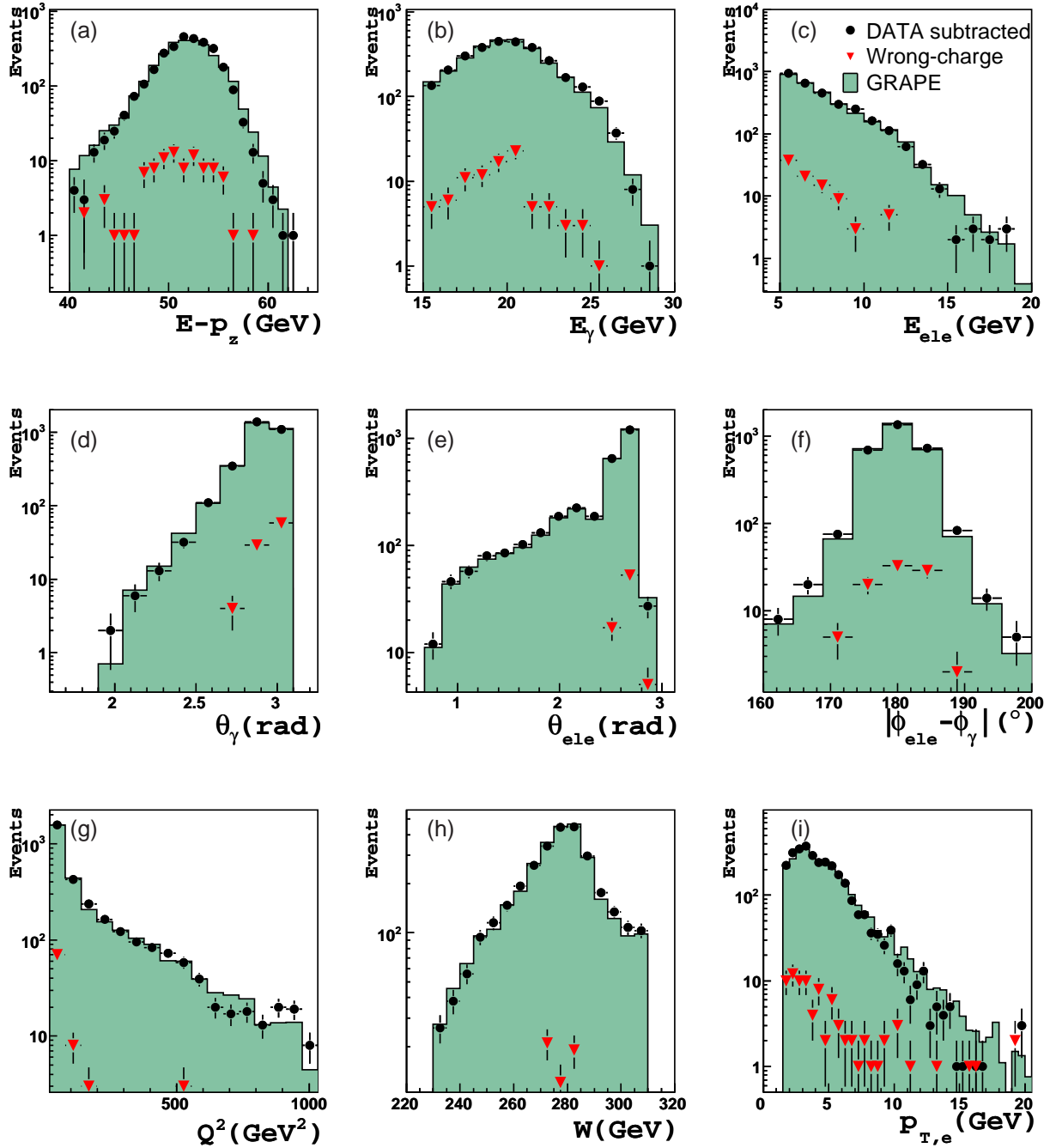
**Figure 7.3:** e-sample control plots for BH cross section measurement **after the reweighting and** $p_{T,e}$ **cut**: data and MC distributions of E $-$ $p_z$ (a), the energy of the $\gamma$ (b), the energy of the electron (c), the polar angle of the photon (d) and of the electron (e), the coplanarity (f), $Q^2$ (g), $W$ (h) and $p_{T,e}$ (i). The dots are the data events after the subtraction of the wrong-charge events which are shown as triangles. The histograms shown the GRAPE MC contribution normalized to the remaining data events after the subtraction.
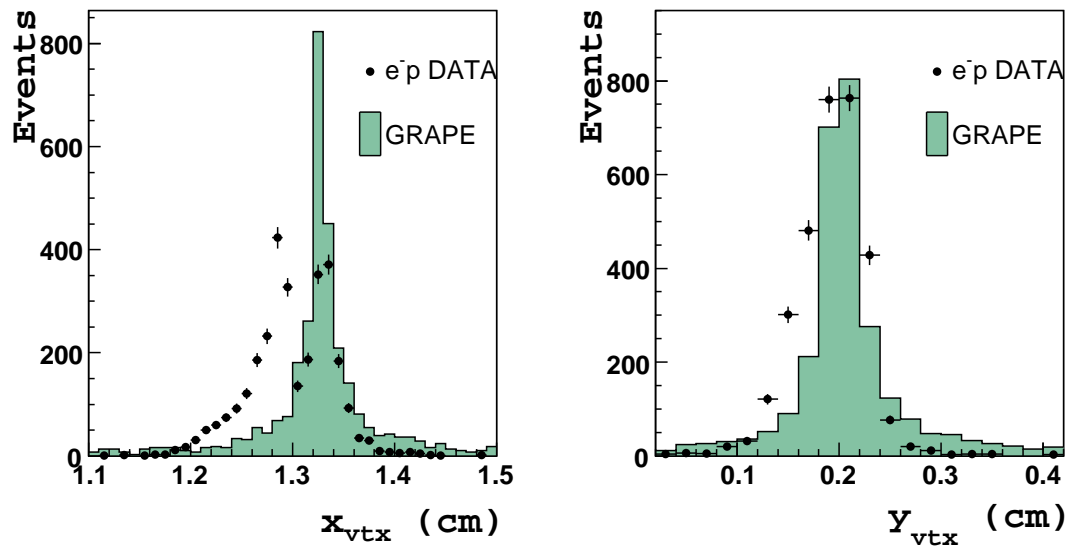
**Figure 7.4:** Distributions for the $X$ (right) and $Y$ (left) positions of the vertex for $e^-p$ sample compared the MC.

# BH cross section measurements

This chapter describes the measurements of the leading order cross sections for elastic Bethe-Heitler events. The extraction of the cross sections is done using the e-sample defined in the previous chapter. Measurements are made of single differential cross sections with respect to the kinematic variables $Q^2$ and $W$ and, to the transverse momentum of the electron, $p_{T,e}$, and the polar angle of the electron, $\theta_e$. The cross sections presented here are based on the 2004-2005 $e^-p$ data sample.

## 8.1  Bin selection, acceptance and purity

In order to extract the cross sections, the selected events are binned in the appropriated variables. The choice of the sizes and limits of the bins is done according to the statistical precision of the data and the resolution.

The acceptance, $\mathcal{A}$, and purity, $\mathcal{P}$, are defined for MC for each of the bins as follows

$$\mathcal{A} = \frac{N_{meas}}{N_{gen}} \quad , \quad \mathcal{P} = \frac{N_{meas\&gen}}{N_{meas}}, \tag{8.1}$$

where $N_{meas}$ is the number of events that satisfy the selection criteria and are binned according to the reconstructed variables. $N_{gen}$ is the number of generated events inside the kinematic region of interest, binned according to the true values of the variables. $N_{meas\&gen}$ represents the number of events measured and generated.

These quantities estimate the quality of the cross section measurement and the bin selection. The acceptance is mainly a measure of the effect of the event selection and the geometrical acceptance of the detector. The purity reflects the migration of events from adjacent bins.

The purity and acceptance, calculated from MC, in the bins used to extract the single differential cross section are shown in figures 8.1 and 8.2. The acceptances for most of the bins lie above of 30%. The dips observed in the acceptances

in $\theta_e$ and $W$ bins are caused by the super-crack cut, that has not been accounted for in the cuts of $N_{gen}$. Purities are typically $\gtrsim 70\%$.
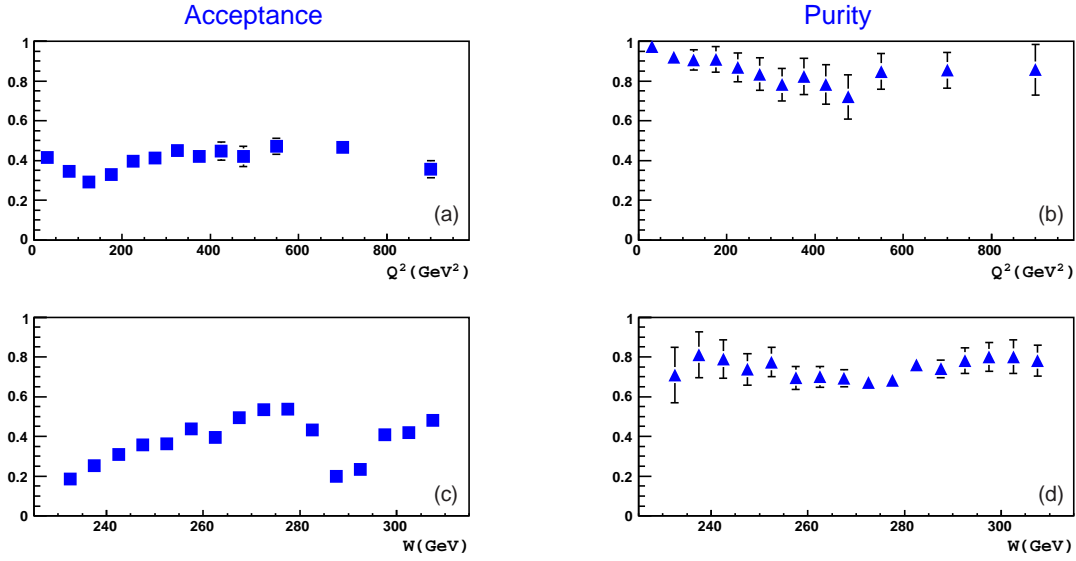


**Figure 8.1:** The acceptance of each $Q^2$ (a) and $W$ (c) bins. The plots on the right correspond to the purity for each $Q^2$ (b) and $W$ (d) bins.
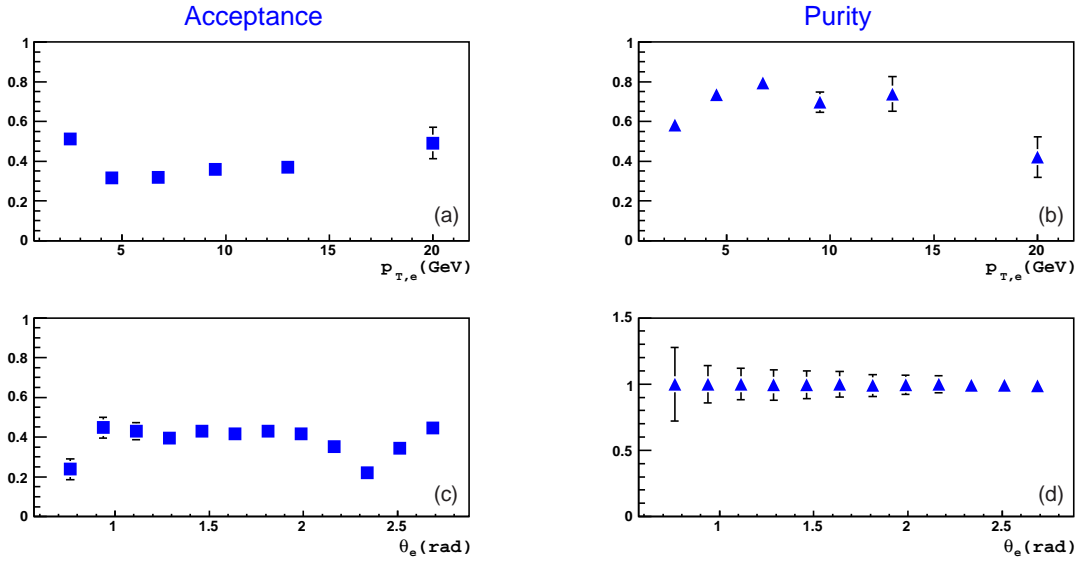


**Figure 8.2:**  The acceptance of each $p_{T,e}$ (a) and $\theta_e$ (c) bins. The plots on the right correspond to the purity for each $p_{T,e}$ (b) and $\theta_e$ (d) bins.

In figure 8.3, the $Q^2$ resolutions are shown in two cross section bins corresponding to the low and high $Q^2$ region. The distributions are centered around

zero, thus no large bias is expected. The resolutions for all bins choosen to calculate the single differential cross sections in $Q^2$, $W$, $p_{T,e}$ and $\theta_e$ are shown in A.
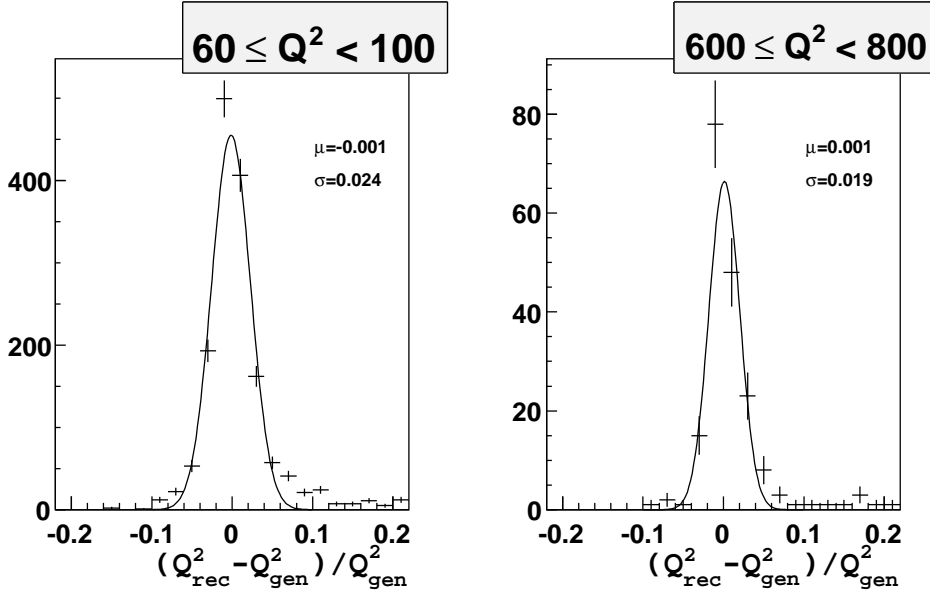


**Figure 8.3:** Example of resolution of the measured $Q^2$ in 2 bins used to extract the cross section $d\sigma/dQ^2$. Curves represent a fit with a Gaussian distribution.

## 8.2   Cross section extraction

The single differential cross sections in each bin of a generic variable $X$ were measured using the relation

$$\frac{d\sigma}{dX} = \frac{(N^{data} - N^{bg})}{\Delta X \mathcal{L}^{data}} \frac{1}{\mathcal{A}(1+\delta)} \tag{8.2}$$

where

- $N^{data}$ is the number of data events in the bin.

- $N^{bg}$ is the total number of background events in the bin. Two contributions are taking into account here: the measured events belonging to the wrong-charge sample and the inelastic events estimated by GRAPE MC, weighted to the luminosity of the data.

- $\mathcal{A}$ acceptance, as defined before, $\mathcal{A} = N^{MC}_{meas}/N^{MC}_{gen}$.

- $\mathcal{L}^{data}$ is the luminosity of the data.

- $\Delta X$ is the bin width.

- $\delta$ corresponds to the radiative correction factor: $\delta = \sigma^{full}/\sigma^{LO} - 1$, where $\sigma^{full}$ is the cross section including radiative corrections and $\sigma^{LO}$ is the leading order cross section.

Since the radiative corrections are fully included in the MC simulation, the cross section extraction can be simplified using

$$N_{gen}^{MC} = \mathcal{L}^{MC}\sigma^{full}, \tag{8.3}$$

where $N_{gen}^{MC}$ is the number MC events generated in the bin, $\mathcal{L}^{MC}$ is the MC luminosity. Then, the leading order cross section is extracted according to

$$\frac{d\sigma}{dX} = \frac{(N^{data} - N^{bg})}{\Delta X N_{meas}^{MC}}\frac{\mathcal{L}^{MC}}{\mathcal{L}^{data}}\frac{d\sigma^{LO}}{dX} \tag{8.4}$$

The statistical uncertainty calculation for the extraction of the cross sections takes into account the statistical error for the number of data and the contribution for MC statistics. The statistical error assigned to the data is $\sqrt{N^{data}}$. For MC, the statistical error is computed as $\sqrt{\sum_i w_i^2}$, where $w_i$ are the event weights.

## 8.3   Systematic uncertainties

The systematics uncertainties on the cross section measurements were calculated varying the relevant measured quantities as well as elements followed of the analysis procedure. For each systematic uncertainty the cross sections are extracted and compared to the nominal values, and the difference is considered to be the systematic error. The following systematics have been take into account:

**Variation of the selection thresholds**

The distributions of simulated and real data events are not identical. When the selection cuts are applied, these differences can result in biases in the measured cross sections. In order to estimate the uncertainties, the main selection thresholds are varied in data and MC according with to resolutions.

The variation of the selection cuts resulted in small changes in the measured cross sections. However, varying the threshold for the elasticity cut was found to

| Cut Quantity | Variation |
|:---:|:---:|
| $E - p_z$(low limit) | 40±2 GeV |
| $E - p_z$(high limit) | 70±2 GeV |
| $E_e$ | 5±1 GeV |
| $p_{track}$ | 0.5 ±0.1 GeV |
| $p_{T,e}$ | 1.5 ±0.15 GeV |
| $E_{cell}$(elasticity cut) | ± 40 MeV |

**Table 8.1:** Summary of the variation of selection threshold used as a systematic checks.

give changes of around 10%. Table 8.3 shows a summary of the selection thresholds varied.

**Systematic checks related to detector effects**

- The electromagnetic energy scale in MC was varied[1] by ±2% for electromagnetic clusters found in the BCAL region and by ±1% for the ones found in the RCAL. Variation up to $\sim 20\%$ are observed in the measured cross sections.

- To account for alignment effects, the position of the candidates found in the RCAL was changed by ±5 mm resulting in an average change on the cross section of $\sim 5\%$. In the lowest bin of W a variation up to 30% is observed.

**Systematic checks related to background subtraction and reweighting procedure**

- The normalization of the inelastic contribution was varied within the limits of the fit obtained from the coplanarity distribution. The highest variation ($\sim 10\%$) was found in the highest $p_{T,e}$ bin.

- The MC prediction of the dilepton process was subtracted (instead of using the wrong-charge data sample). Small changes, up to($\sim 5\%$), were observed.

- The reweighting of the MC events according to $\theta_e$ distribution was not applied. The average change resulting from this systematic check was $\sim$ 10%.

---

[1]See section 4.3.1.

The total systematic uncertainties were determined by adding separately in quadrature the positive and negative individual contributions for each bin. The individual contributions of each of the systematic checks are shown in B. In addition, an overall normalization uncertainty is expected due to the error in the luminosity measurements ($e^-p : \pm 2.7\%$).

## 8.4   Measured cross sections

The results on the measurements of the single differential cross section with respect to $Q^2$, $W$, $p_{T,e}$ and $\theta_e$ are shown in figures 8.4 and 8.5. In each of the plots, the inner error bars correspond to the statistical errors while the total error bar shows the quadratic sum of the statistical and systematic errors.

The measured cross sections are compared to the prediction given by the GRAPE MC. The absolute predictions of the MC were found to lie systematically above the data. In order to compare the shape of the cross sections, the GRAPE predictions have been scaled by a constant factor of 0.7 (dotted line in figures 8.4 and 8.5). As seen from the plots, the shape of the data is well reproduced by MC.

The values of the measured cross sections with their corresponding statistical and systematic uncertainties are listed in tables 8.2-5.

| $Q^2$ bin (GeV$^2$) | $d\sigma/dQ^2$ (pb/GeV$^2$) |
|:---:|:---:|
| 20-60 | $0.41 \pm 0.02^{+0.08}_{-0.02}$ |
| 60-100 | $0.31 \pm 0.02^{+0.01}_{-0.03}$ |
| 100-150 | $0.15 \pm 0.01^{+0.06}_{-0.03}$ |
| 150-200 | $0.08 \pm 0.01^{+0.01}_{-0.02}$ |
| 200-250 | $0.050 \pm 0.01^{+0.007}_{-0.001}$ |
| 250-300 | $0.030 \pm 0.01^{+0.001}_{-0.001}$ |
| 300-350 | $0.022 \pm 0.004^{+0.001}_{-0.005}$ |
| 350-400 | $0.014 \pm 0.003^{+0.003}_{-0.003}$ |
| 400-450 | $0.018 \pm 0.004^{+0.001}_{-0.002}$ |
| 450-500 | $0.015 \pm 0.004^{+0.001}_{-0.002}$ |
| 500-600 | $0.012 \pm 0.002^{+0.001}_{-0.003}$ |
| 600-800 | $0.004 \pm 0.001^{+0.001}_{-0.001}$ |
| 800-1000 | $0.005 \pm 0.001^{+0.001}_{-0.001}$ |

**Table 8.2:** Measured values of $d\sigma/dQ^2$
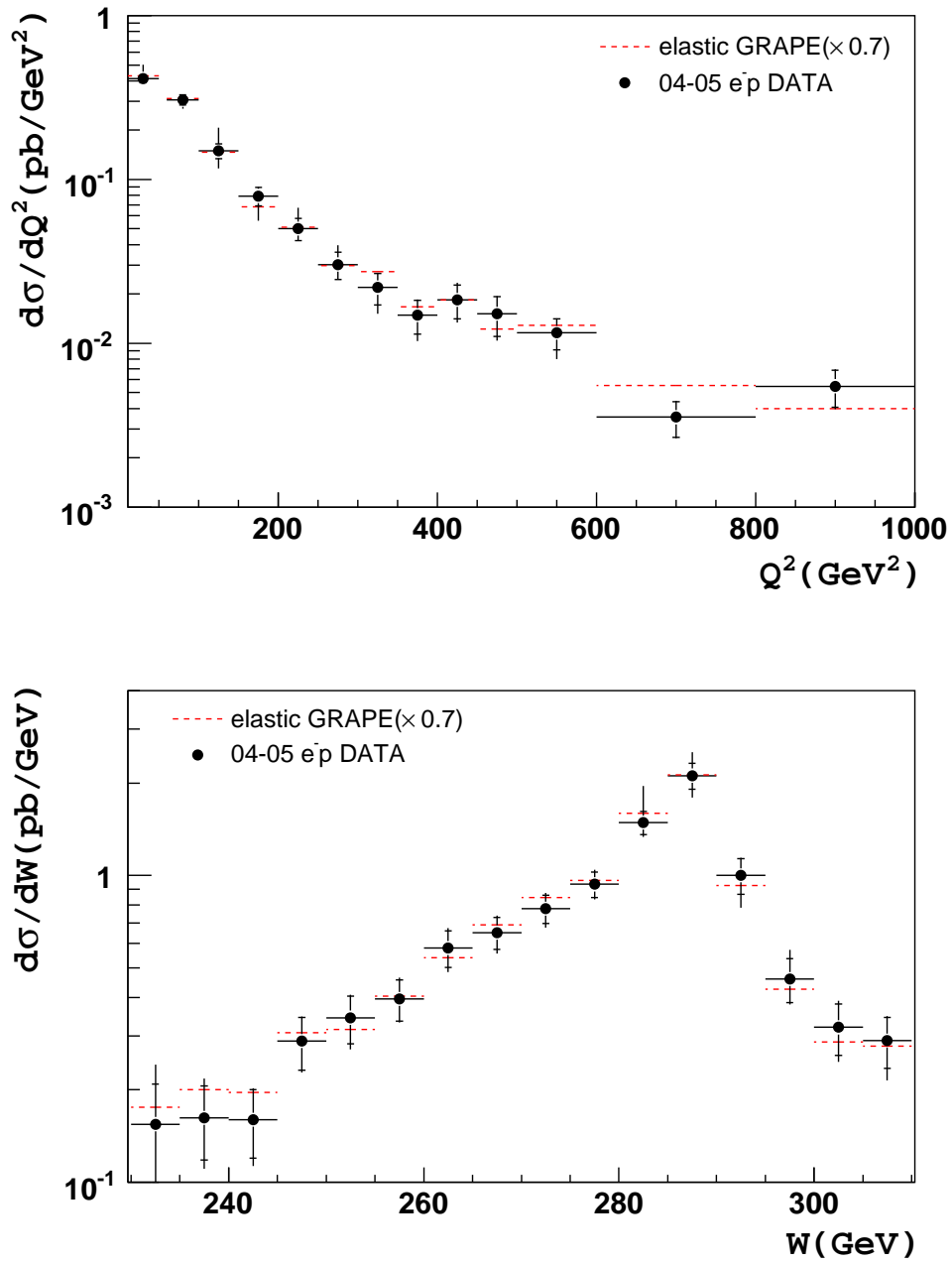
**Figure 8.4:** $d\sigma/dQ^2$ (top) and $d\sigma/dW$ (bottom) measured in this analysis. The error bars on the data point correspond to the statistical uncertainties (inner bars) and to the statistical and systematics uncertainties added in quadrature (outer bars).
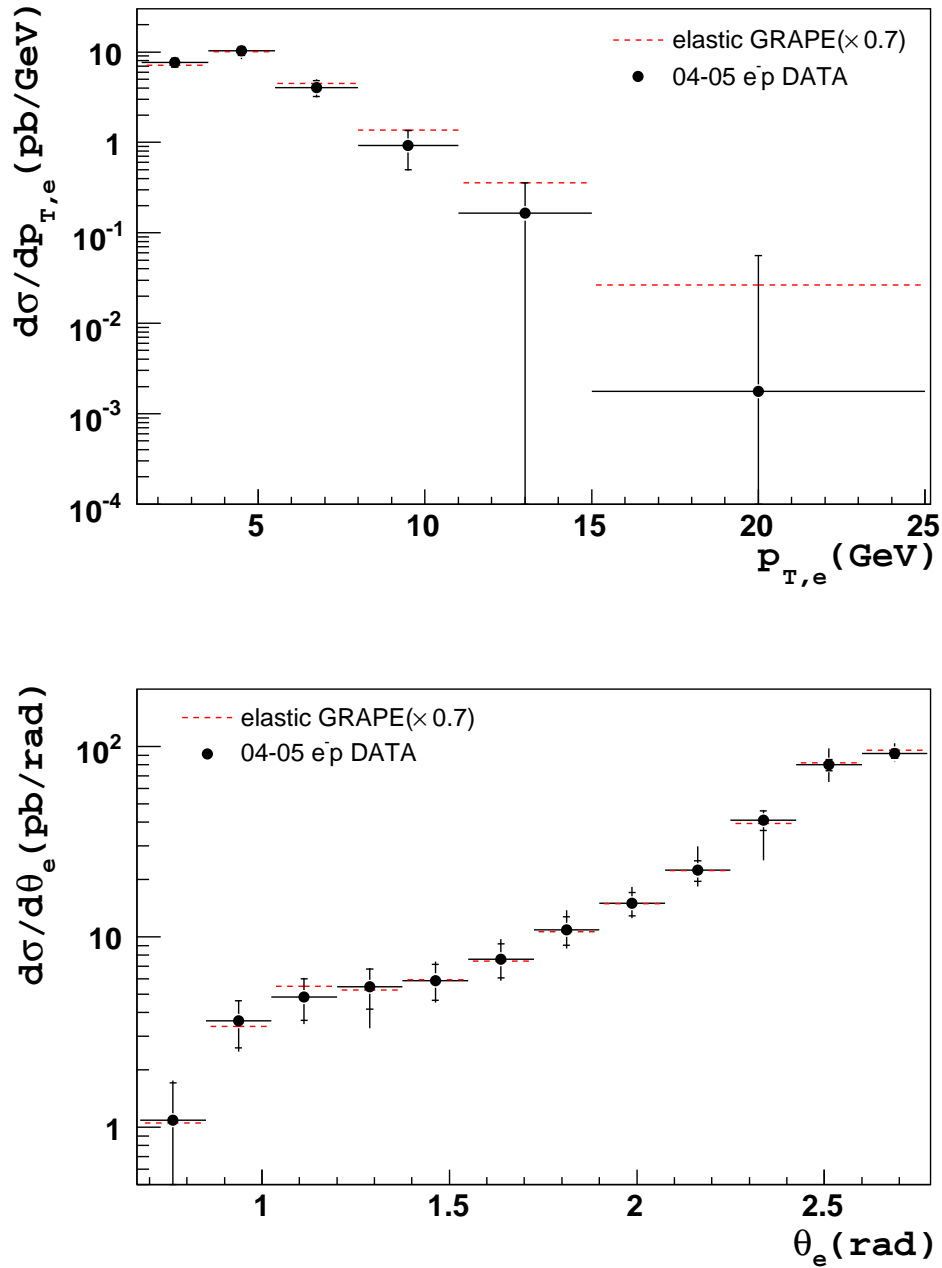
**Figure 8.5:** $d\sigma/dp_{T,e}$ (top) and $d\sigma/d\theta_e$ (bottom) measured in this analysis. The error bars on the data point correspond to the statistical uncertainties (inner bars) and to the statistical and systematics uncertainties added in quadrature (outer bars).

| $W$ bin (GeV) | $d\sigma/dW$ (pb/GeV) |
|:---:|:---:|
| 230-235 | $0.15 \pm 0.05^{+0.07}_{-0.02}$ |
| 235-240 | $0.16 \pm 0.04^{+0.03}_{-0.03}$ |
| 240-245 | $0.16 \pm 0.04^{+0.01}_{-0.02}$ |
| 245-250 | $0.29 \pm 0.06^{+0.01}_{-0.02}$ |
| 250-255 | $0.34 \pm 0.06^{+0.02}_{-0.04}$ |
| 255-260 | $0.40 \pm 0.06^{+0.03}_{-0.02}$ |
| 260-265 | $0.58 \pm 0.08^{+0.05}_{-0.05}$ |
| 265-270 | $0.65 \pm 0.07^{+0.04}_{-0.06}$ |
| 270-275 | $0.78 \pm 0.08^{+0.05}_{-0.06}$ |
| 275-280 | $0.93 \pm 0.09^{+0.05}_{-0.04}$ |
| 280-285 | $1.48 \pm 0.13^{+0.45}_{-0.10}$ |
| 285-290 | $2.11 \pm 0.20^{+0.35}_{-0.25}$ |
| 290-295 | $1.00 \pm 0.13^{+0.05}_{-0.17}$ |
| 295-300 | $0.46 \pm 0.07^{+0.08}_{-0.02}$ |
| 300-305 | $0.32 \pm 0.06^{+0.03}_{-0.04}$ |
| 305-310 | $0.29 \pm 0.05^{+0.02}_{-0.05}$ |

**Table 8.3:** Measured values of $d\sigma/dW$

| $p_{T,e}$ bin (GeV) | $d\sigma/dp_{T,e}$ (pb/GeV) |
|:---:|:---:|
| 1.5-3.5 | $7.65 \pm 0.85^{+1.30}_{-0.31}$ |
| 3.5-5.5 | $10.31 \pm 1.15^{+0.21}_{-1.65}$ |
| 5.5-8 | $4.02 \pm 0.80^{+0.53}_{-0.34}$ |
| 8-11 | $0.92 \pm 0.42^{+0.14}_{-0.11}$ |
| 11-15 | $0.16 \pm 0.19^{+0.04}_{-0.02}$ |
| 15-25 | $0.002 \pm 0.054^{+0.001}_{-0.001}$ |

**Table 8.4:** Measured values of $d\sigma/dp_{T,e}$

**127**

| $\theta_e$ bin (rad) | $d\sigma/d\theta_e$ (pb/rad) |
|:---:|:---:|
| 0.67-0.85 | $1.08 \pm 0.62^{+0.23}_{-0.28}$ |
| 0.85-1.02 | $3.61 \pm 1.00^{+0.20}_{-0.50}$ |
| 1.02-1.20 | $4.82 \pm 1.18^{+0.40}_{-0.65}$ |
| 1.20-1.37 | $5.46 \pm 1.30^{+0.44}_{-1.73}$ |
| 1.37-1.55 | $5.89 \pm 1.25^{+0.85}_{-0.59}$ |
| 1.55-1.72 | $7.62 \pm 1.53^{+1.39}_{-0.83}$ |
| 1.72-1.90 | $10.90 \pm 1.86^{+2.28}_{-1.10}$ |
| 1.90-2.07 | $15.00 \pm 2.12^{+2.45}_{-1.31}$ |
| 2.07-2.25 | $22.40 \pm 2.75^{+6.95}_{-2.82}$ |
| 2.25-2.42 | $40.95 \pm 4.85^{+2.19}_{-15.00}$ |
| 2.42-2.60 | $80.04 \pm 5.47^{+16.90}_{-13.83}$ |
| 2.60-2.77 | $91.61 \pm 5.10^{+11.35}_{-6.27}$ |

**Table 8.5:** Measured values of $d\sigma/d\theta_e$

# Summary and conclusions

The analysis in this thesis is a comprehensive study of Deeply Virtual Compton Scattering (DVCS) and Bethe-Heitler (BH) processes with the ZEUS detector using a HERA II data set. The data were taken between 2003-2005, corresponding to an integrated luminosity of 41 pb$^{-1}$ for $e^+p$ and 136 pb$^{-1}$ for $e^-p$ .

The analysis is based in the selection of events according to the topology expected for the final states of DVCS and BH at ZEUS: an electron and a photon candidate. An e-sample is defined by the electron scattered at smaller polar angles w.r.t the proton direction than the photon candidate and therefore with a reconstructed track. The main contribution to the e-sample is the Bethe-Heitler proccess. On the other hand, the $\gamma$-sample , which contains DVCS and BH contributions, is characterized by the photon located at lower polar angles and, in most of the cases, no reconstructed track associated to the electron candidate due to the acceptance limitation of the tracking detectors.

**Elastic Bethe-Heitler cross section**

The elastic BH cross sections are extracted for $e^-p$ data based on the e-sample in the kinematic region of 230 GeV < W < 310 GeV, 20 GeV$^2$ < Q$^2$ < 1000 GeV$^2$ and $|t|$ < 1 GeV$^2$. The control distributions and the measured cross sections are found to agree well in shape with the theoretical predictions as available in the GRAPE-Compton MC. The precision of the measurements is typically of the order 10-20%, with similar contribution of the statistical and correlated systematic errors.

The absolute normalization of the prediction is found to be too high by a factor $\sim$ 1.4. Possible reasons which could account for this discrepancy are a wrong normalization of the LO elastic predictions or the contribution of the proton dissociative process. The good agreement of the shapes of the distribution disfavors experimental effects as a possible explanation.

**DVCS analysis**

The $\gamma$-sample is compared with the prediction for the DVCS and BH processes. The number of data events and the absolute predictions from GenDVCS and GRAPE-Compton agree within $\sim$5%. Note that this only holds if the factor 1.4 observed in the BH measurement is not applied here.

The shapes of most of the kinematics distributions is in reasonable agreement with the predictions. This is also valid for the distribution in $\theta_\gamma$ for large $\theta_\gamma$. However, at small values of $\theta_\gamma$, the data overshoots the expectations significantly (by a factor of $\sim$1.25). In this region, the relative contribution of DVCS is largest and therefore would dominate a DVCS cross section determination.

A considerable number of studies have been done in order to understand the excess in low $\theta_\gamma$ region. The studies have tried to cover different hypothesis:

- Background processes: vector meson production $(\omega, \phi)$, proton dissociation contribution, prompt $\gamma$, $\pi^0$ , inclusive DIS and diffractive events, photoproduction contribution and beam induced background.

- Detector related effects: shower shape studies, possible bias in $\theta_\gamma$ calculation, DQM, preshowering particles and elasticity cut.

All the checks have given negative results to explain the excess. A study of a DVCS cross section determination is documented in appendix C. It is emphasized however, that because of the unexplained differences in the shapes of the distributions, it is not possible to determine the full systematic error of that measurement.

The results presented here have shown the difficulties of the measurements of DVCS at HERA II. The feasibility of future measurements on DVCS strongly depends on the further understanding of the effects observed in this analysis.

# Resolution plots

The resolutions have been calculated in all the bins used for the elastic Bethe-Heitler cross section measurements presented in chapter 8.

In figures A.1, A.2, A.3 and A.4, the resolutions, as measured from MC, are shown in the cross section bins for the single differential cross sections in $Q^2$, $W$, $p_{T,e}$ and $\theta_e$, respectively. The result of the fit performed on the distributions is also shown in each corresponding figure.
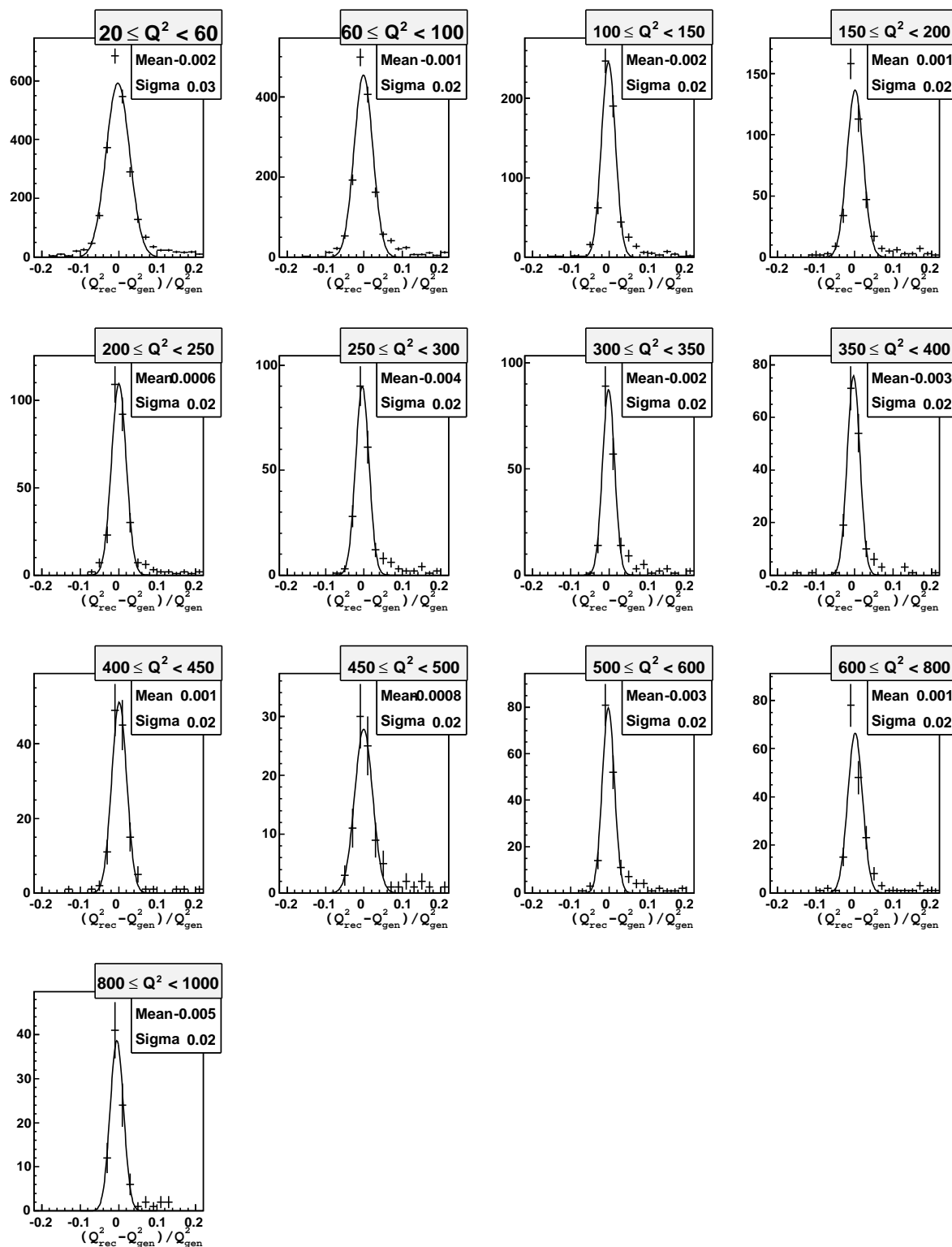
**Figure A.1:** The resolutions of the measured $Q^2$ in the bins used to extract the $d\sigma/dQ^2$. Curves represent a fit with a Gaussian distribution.
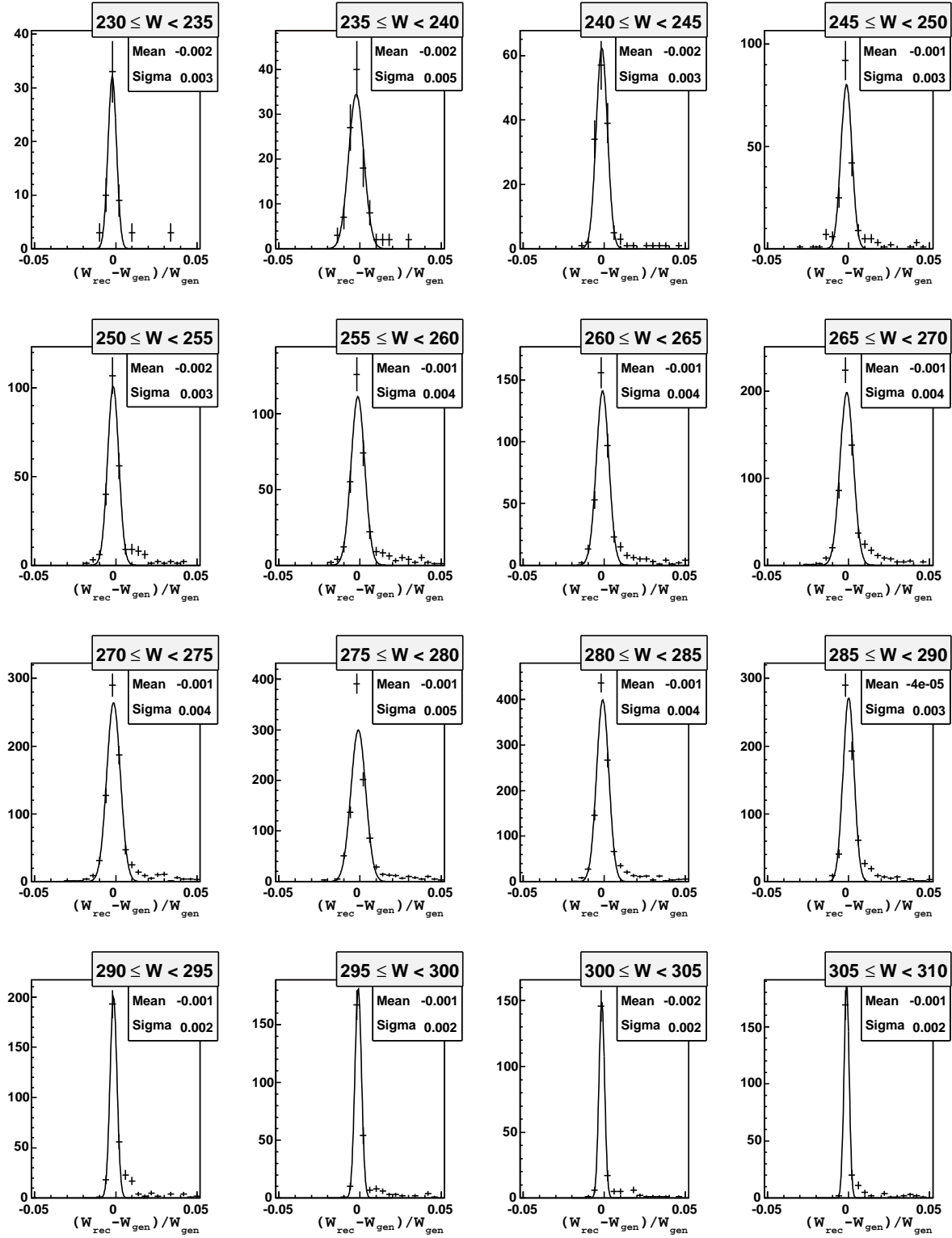
**Figure A.2:** The resolutions of the measured $W$ in the bins used to extract the $d\sigma/dW$. Curves represent a fit with a Gaussian distribution.

133
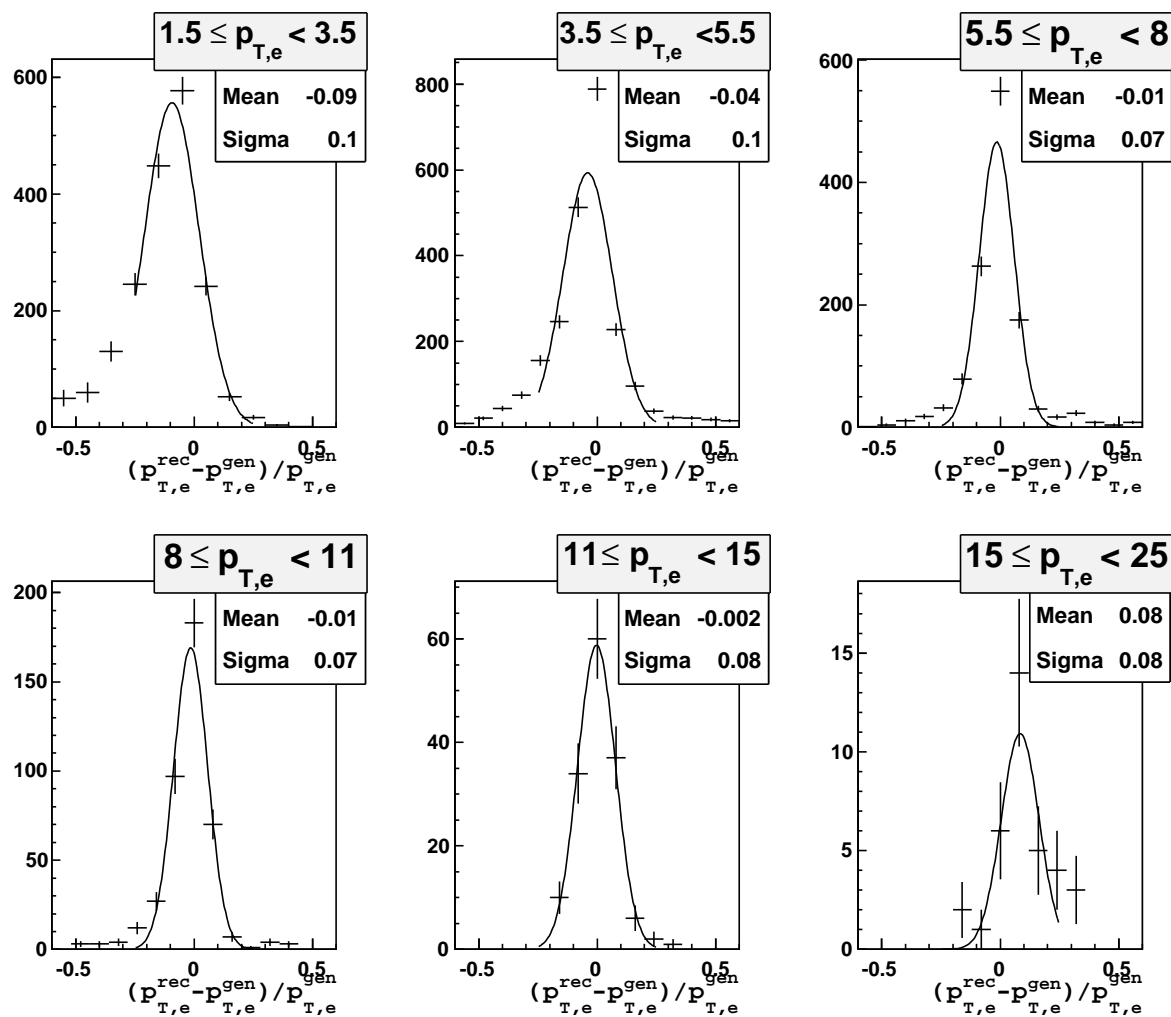
**Figure A.3:** The resolutions of the measured $p_{T,e}$ in the bins used to extract the $d\sigma/dp_{T,e}$. Curves represent a fit with a Gaussian distribution.
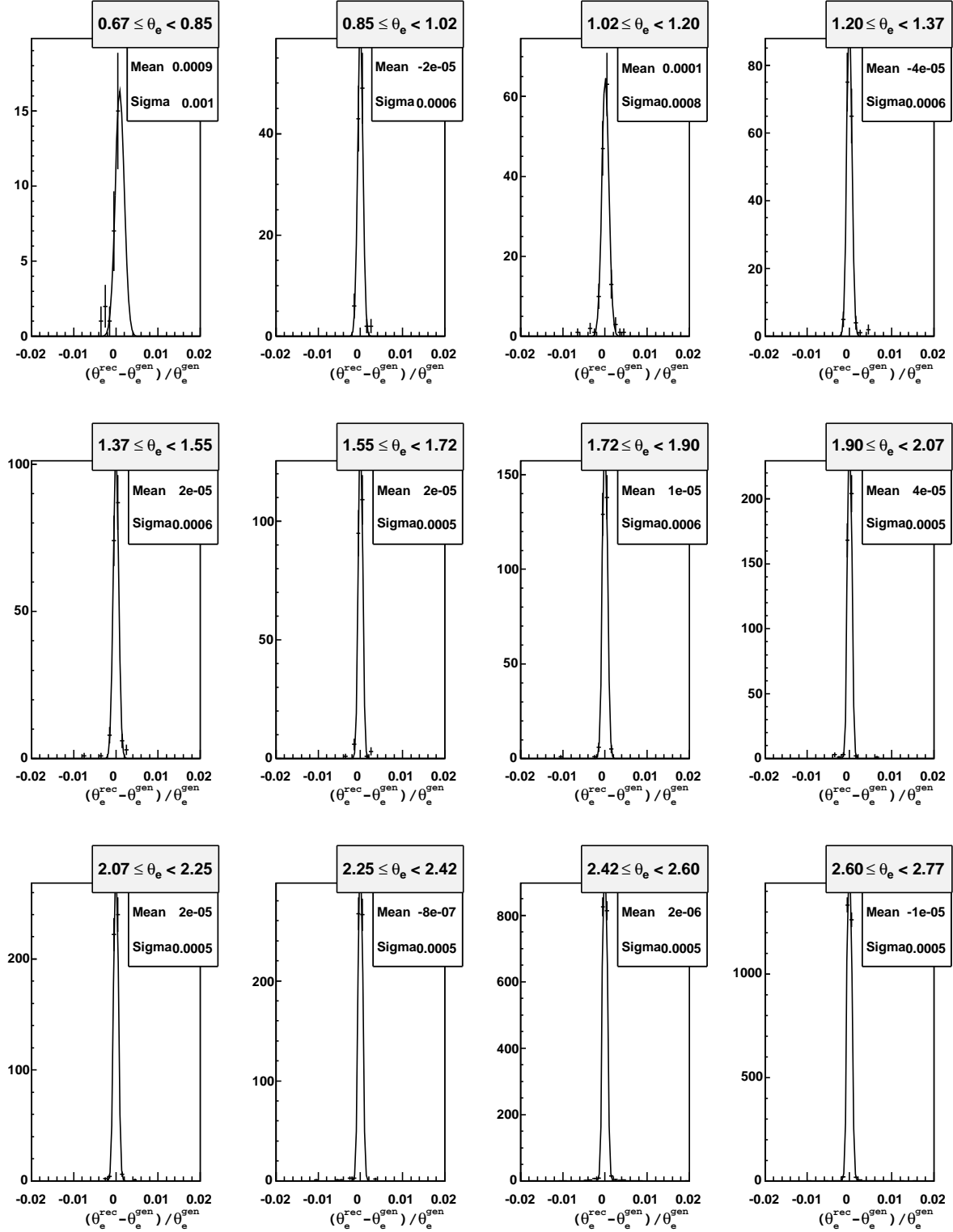
**Figure A.4:** The resolutions of the measured $\theta_e$ in the bins used to extract the $d\sigma/d\theta_e$. Curves represent a fit with a Gaussian distribution.

# Systematic uncertanties

This appendix contains the systematic uncertanties that enter in the elastic Bethe-Heitler cross section measurements. The systematic uncertanties are calculated according to section C.4.

In figures B.1, B.2, B.3 and B.4, the relative change in the cross section for each of the systematic uncertanties is shown separatly, and this is done for every cross section. The numbering in the X axis of figures corresponds to each of the systematic checks (see section C.4):

1. $E_e > 4$ GeV
2. $E_e > 6$ GeV
3. $38$ GeV $< E - p_z < 72$ GeV
4. $42$ GeV $< E - p_z < 68$ GeV
5. $p_{track} > 0.4$ GeV
6. $p_{track} > 0.6$ GeV
7. $p_{T,e} > 1.35$ GeV
8. $p_{T,e} > 1.65$ GeV
9. Elasticity cut $(+40$ MeV$)$
10. Elasticity cut $(-40$ MeV$)$
11. Energy scale candidate 2(+ variation)
12. Energy scale candidate 2(- variation)
13. Energy scale candidate 1(+ variation)
14. Energy scale candidate 1(- variation)
15. Position RCAL candidate (+5 mm)
16. Position RCAL candidate (−5 mm)
17. Inelastic contribution (high limit)
18. Inelastic contribution (low limit)
19. MC reweighting check
20. Dilepton contribution
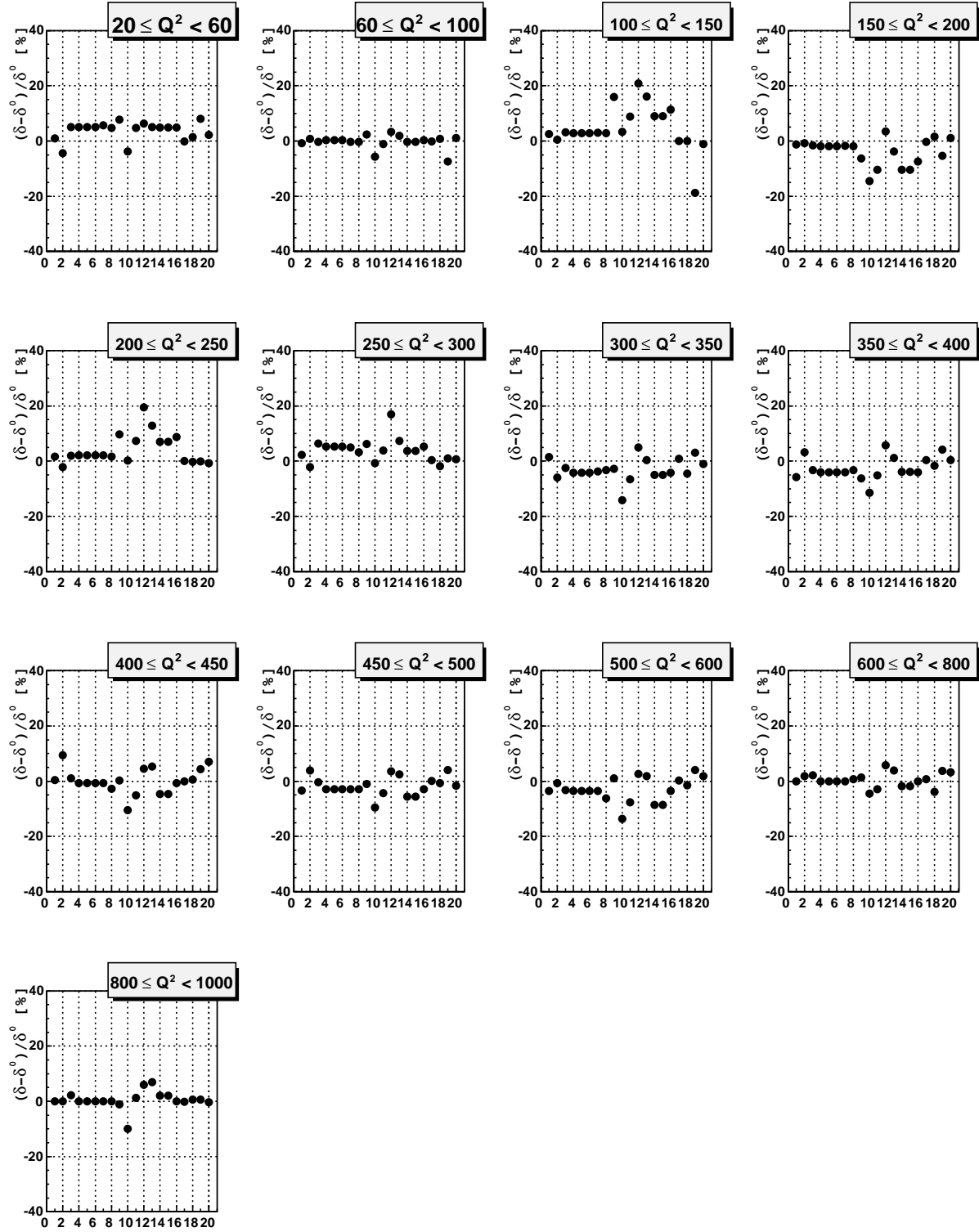
**Figure B.1:** Systematic uncertanties for the measurement of $d\sigma/dQ^2$.
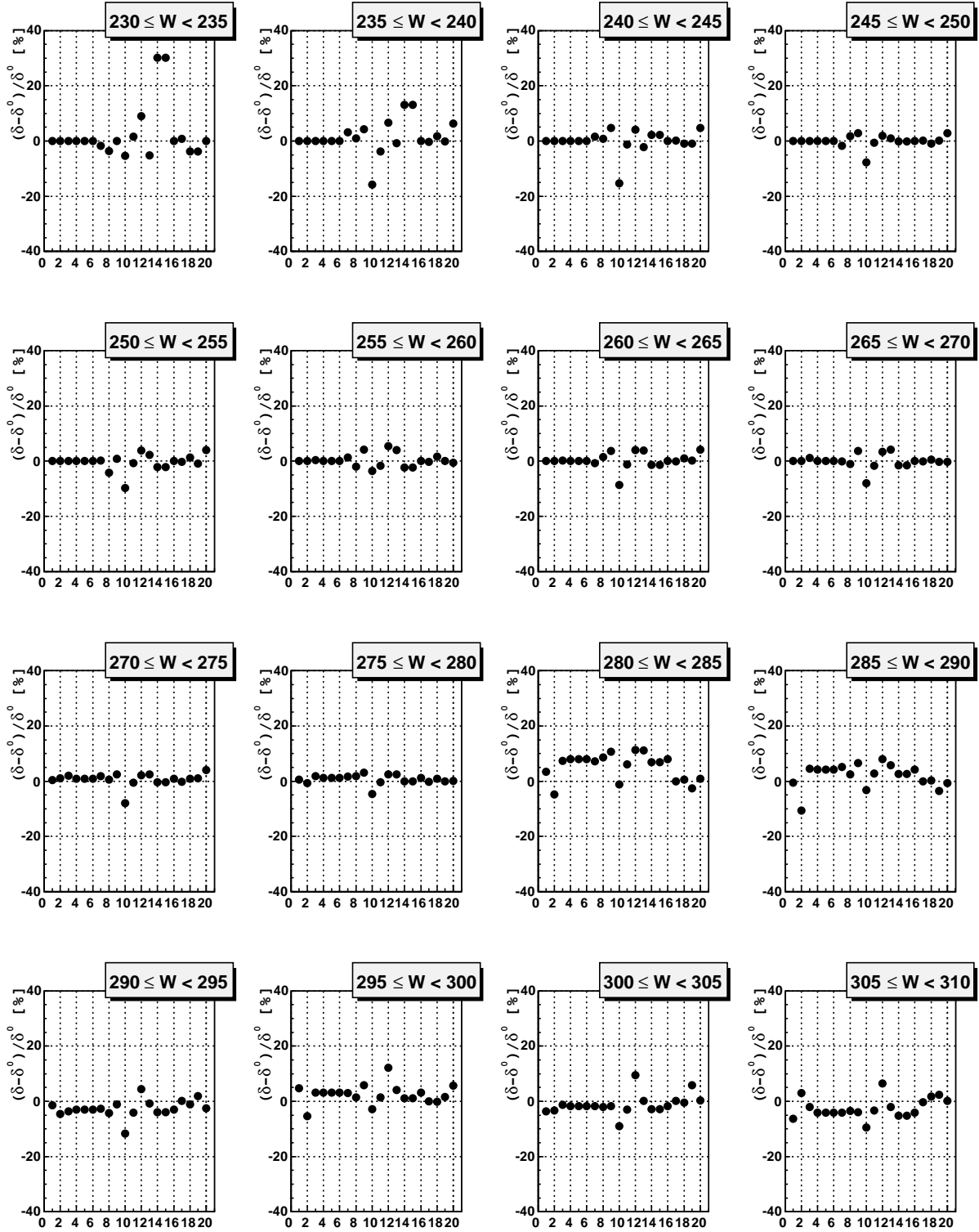
**Figure B.2:** Systematic uncertanties for the measurement of $d\sigma/dW$.
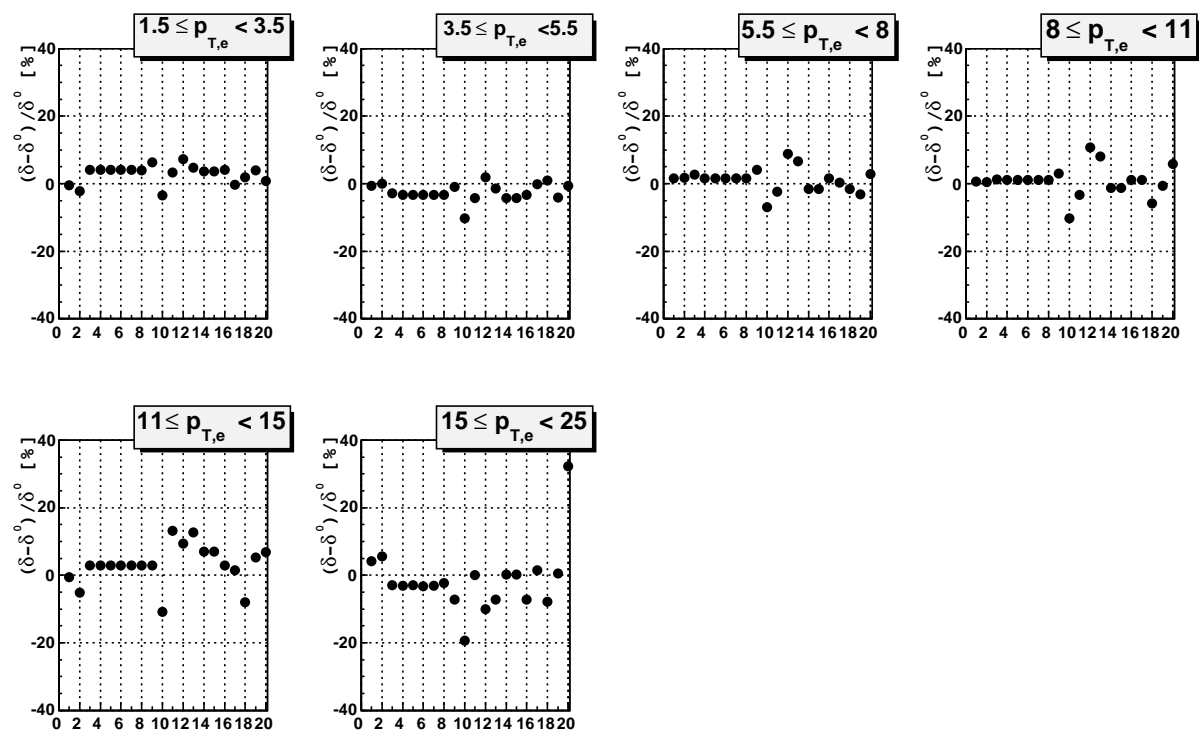
**Figure B.3:** Systematic uncertanties for the measurement of $d\sigma/dp_{T,e}$.
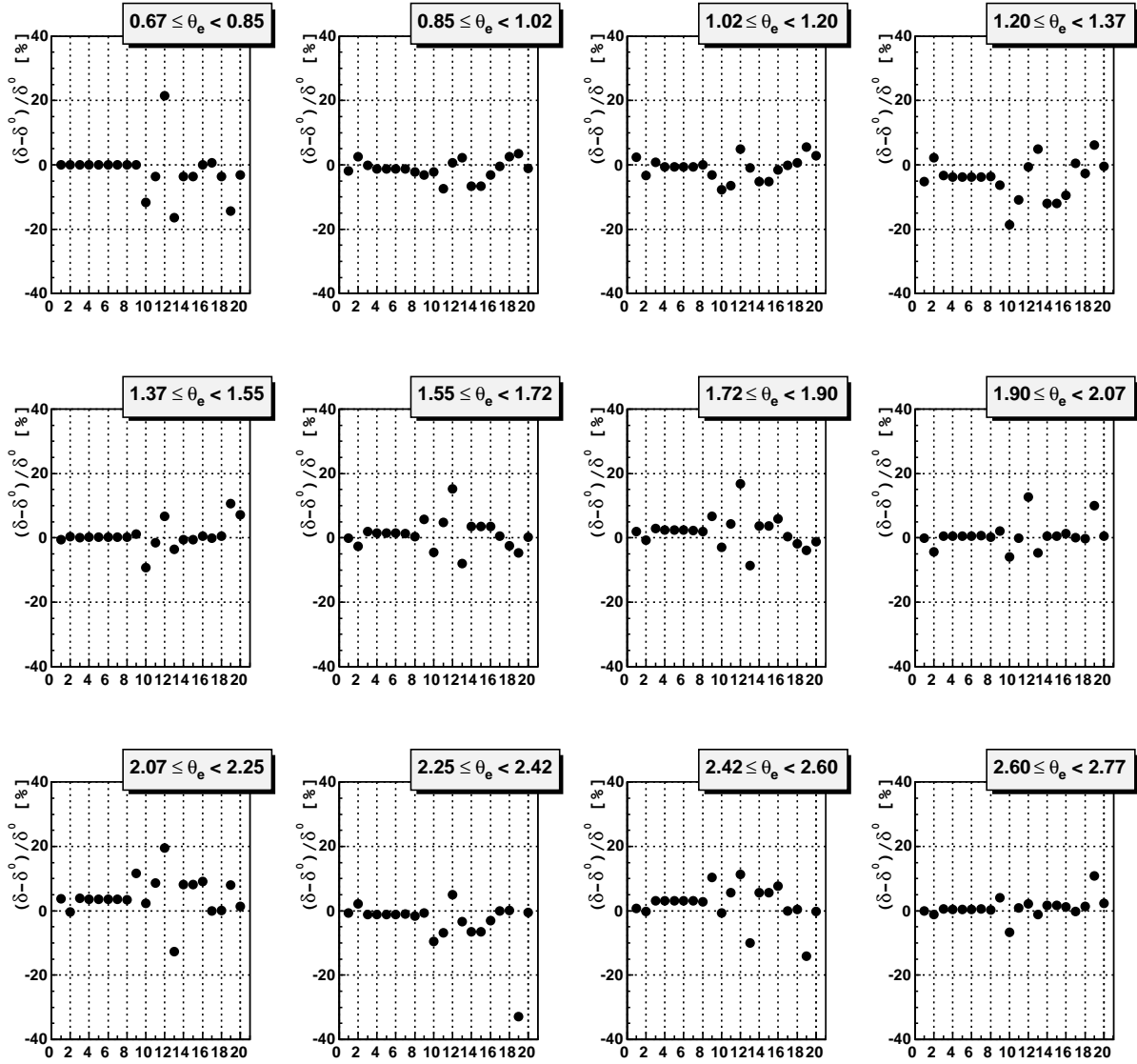
**Figure B.4:** Systematic uncertanties for the measurement of $d\sigma/d\theta_e$.

141

# DVCS cross section measurements

This chapter reports a measurements of the single differential $ep$ cross section as well as the $\gamma^{\star}p$ cross section for the DVCS process. Due to the discrepancies found in the description of data distribution by the MC, the full systematic error of the measurement is not determined.

In the kinematic region defined for the measurement: 40 GeV < W < 140 GeV, 5 GeV$^2$ < Q$^2$ < 100 GeV$^2$ and $|t|$ < 1 GeV$^2$ the interference term between DVCS and BH can be neglected [39] when the cross section is integrated over the angle $\phi$[1]. Therefore the subtraction of the BH contribution in the $\gamma$-sample lead to the DVCS cross section.

## C.1  Cross section definitions

### $ep$ differential cross section

The single differential $ep$ cross section as function of $W$ and $Q^2$ for the DVCS process has been extracted using the following formula:

$$\frac{d\sigma}{dX}(X_i) = \frac{(N_i^{data} - N_i^{BH})(1 - f)}{N_i^{DVCS}} \frac{d\sigma^{DVCS}}{dX}(X_i),\qquad\text{(C.1)}$$

where the subscript $i$ refers to a certain bin of generic variable $X(= W, Q^2)$ and

- $N_i^{data}$ is the total number of data events in the $\gamma$-sample .

- $N_i^{BH}$ is the number of BH events in the $\gamma$-sample determined by GRAPE MC normalized to the luminosity of the data.

---

[1]Azimuthal angle between the lepton and hadronic plane (see section 1.5.1).

- $N_i^{DVCS}$ denotes the number of DVCS events in the $\gamma$-sample determined by GenDVCS MC normalized to the luminosity of the data.

- $f$ is the fraction of inelastic DVCS events (see 6.3.1).

- $\frac{d\sigma^{DVCS}}{dX}(X_i)$ corresponds to the single $ep$ differential cross section computed from the FFS model (see equation 1.33).

### $\gamma^\star p$ differential cross section

The $\gamma^\star p$ cross sections for the DVCS process as a function of $W$ and $Q^2$ are evaluated using

$$\sigma^{\gamma^\star p}(W_i, Q_i^2) = \frac{(N_i^{data} - N_i^{BH})(1-f)}{N_i^{DVCS}} \sigma_{DVCS}^{\gamma^\star p}(W_i, Q_i^2), \qquad \text{(C.2)}$$

where all the terms are defined in the same way as for the $ep$ cross section and $\sigma_{DVCS}^{\gamma^\star p}$ corresponds to the $\gamma^\star p$ cross section computed according to the FFS model [40]. $W_i$ and $Q_i^2$ are the values at which the $\gamma^\star p$ cross section is evaluated.

### Bin selection, acceptance and purity

The size of the bins chosen to extract the cross sections has been done according with the statistics available and also taking into account the problems found with the data and MC comparison. The bin sizes defined for $Q^2$ and $W$ are shown in table C.2 and C.2, respectively.
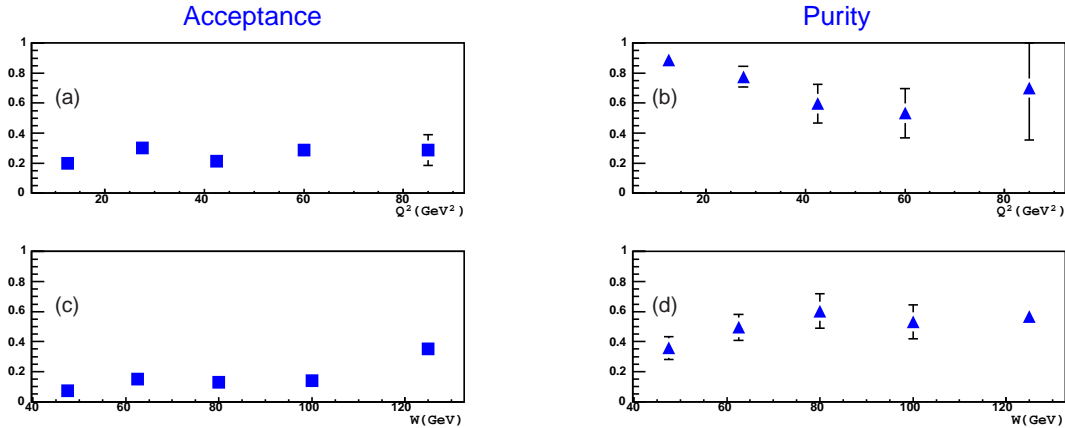


**Figure C.1:**  The acceptance of each $Q^2$ (a) and $W$ (c) bins. The plots on the right correspond to the purity for each $Q^2$ bins (b) and $W$ (d) bins.

The acceptances, $\mathcal{A}_i$, and purities, $\mathcal{P}_i$, for each of the bins were calculated using GenDVCS following the formulae given in section 8.1. The values of $\mathcal{A}_i$ and $\mathcal{P}_i$ as

a function of $Q^2$ and $W$ are depicted in figure C.1. The acceptance is almost flat in $Q^2$ and $W$ with a values between 10%-20%. Purity, which measures migration of events from adjacent bins, decreases until values $\sim$60% for high $Q^2$ bins while the values for $W$ bins are $\sim$50% on average.

## C.2    The *ep* cross sections

The single differential *ep* cross sections as a function of $Q^2$ and $W$ measured in this analysis are shown in figure C.2 (left) and (right), respectively. The cross sections have been calculated separately for $e^+p$ (open circles) and $e^-p$ (triangles) data. For both periods, due to the limited number of events, the cross sections are not measured in the last bins of $Q^2$. The inner error bars represent the statistical errors and the outer the statistical and systematics errors added in quadrature.
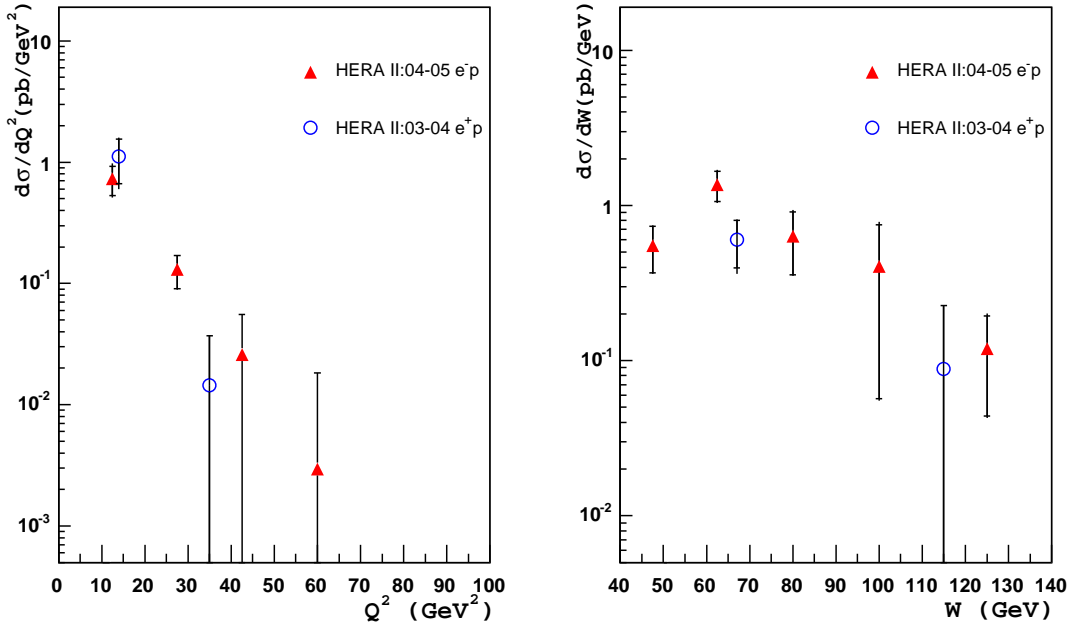


**Figure C.2:**    $d\sigma/dQ^2$ (right) and $d\sigma/dW$ (left) measured in this analysis for the $e^+p$ and $e^-p$ sample. The first $Q^2$ data point for $e^+p$ is displaced horizontally for an easy visualization.

The measured cross sections should have the same behavior for the $e^+p$ and the $e^-p$ data set under the assumption that the contribution of the interference between the DVCS and BH processes is negligible. Within the large uncertainties, the cross section for both data set are compatibles.

The values of the measured cross sections with their corresponding statistical and systematic uncertainties are listed in tables C.2 and C.2.

| $e^- p$ | |
|---|---|
| $Q^2$ bin (GeV$^2$) | $\frac{d\sigma}{dQ^2}$(pb/GeV$^2$) |
| 5 - 20 | $0.73 \pm 0.20^{+0.14}_{-0.08}$ |
| 20 - 35 | $0.13 \pm 0.04^{+0.02}_{-0.01}$ |
| 35 - 50 | $0.025 \pm 0.030^{+0.007}_{-0.002}$ |
| 50 - 70 | $0.0030 \pm 0.0153^{+0.0007}_{-0.0003}$ |
| 70 - 100 | - |

| $e^+ p$ | |
|---|---|
| $Q^2$ bin (GeV$^2$) | $\frac{d\sigma}{dQ^2}$(pb/GeV$^2$) |
| 5 - 20 | $1.11 \pm 0.44^{+0.25}_{-0.18}$ |
| 20 - 50 | $0.014 \pm 0.022^{+0.005}_{-0.001}$ |
| 50 - 100 | - |

**Table C.1:** Values of the single differential $ep$ cross sections for the DVCS process as a function of $Q^2$. Left (right) table corresponds to the $e^- p$ ($e^+ p$ ).

| $e^- p$ | |
|---|---|
| $W$ bin (GeV) | $\frac{d\sigma}{dW}$(pb/GeV) |
| 40 - 55 | $0.55 \pm 0.18^{+0.08}_{-0.05}$ |
| 55 - 70 | $1.36 \pm 0.30^{+0.14}_{-0.11}$ |
| 70 - 90 | $0.63 \pm 0.27^{+0.10}_{-0.06}$ |
| 90 - 110 | $0.40 \pm 0.34^{+0.14}_{-0.04}$ |
| 110 - 140 | $0.12 \pm 0.07^{+0.03}_{-0.01}$ |

| $e^+ p$ | |
|---|---|
| $W$ bin (GeV) | $\frac{d\sigma}{dW}$(pb/GeV) |
| 40 - 90 | $0.60 \pm 0.20^{+0.25}_{-0.18}$ |
| 90 - 140 | $0.090 \pm 0.138^{+0.005}_{-0.001}$ |

**Table C.2:** Values of the single differential $ep$ cross sections for the DVCS process as a function of $Q^2$. Left (right) table corresponds to the $e^- p$ ($e^+ p$ ) data.

# C.3   The $\gamma^\star p$ cross sections

The $\gamma^\star p$ DVCS cross sections were measured as a function of $Q^2$ for an average value of $W = 91.6$ GeV and as a function of $W$ for an average value of $Q^2 = 9.1$ GeV$^2$. The average values were obtained from GenDVCS. The cross sections are displayed in figure C.3 and the corresponding values are listed in tables C.3 and C.3.

The expected steep decrease of the $\gamma^\star p$ DVCS cross section with $Q^2$ is observed.

## Comparison with previous results

The results in this analysis were compared with previous measurement available from the H1 and ZEUS experiments. ZEUS [1] have measured the DVCS
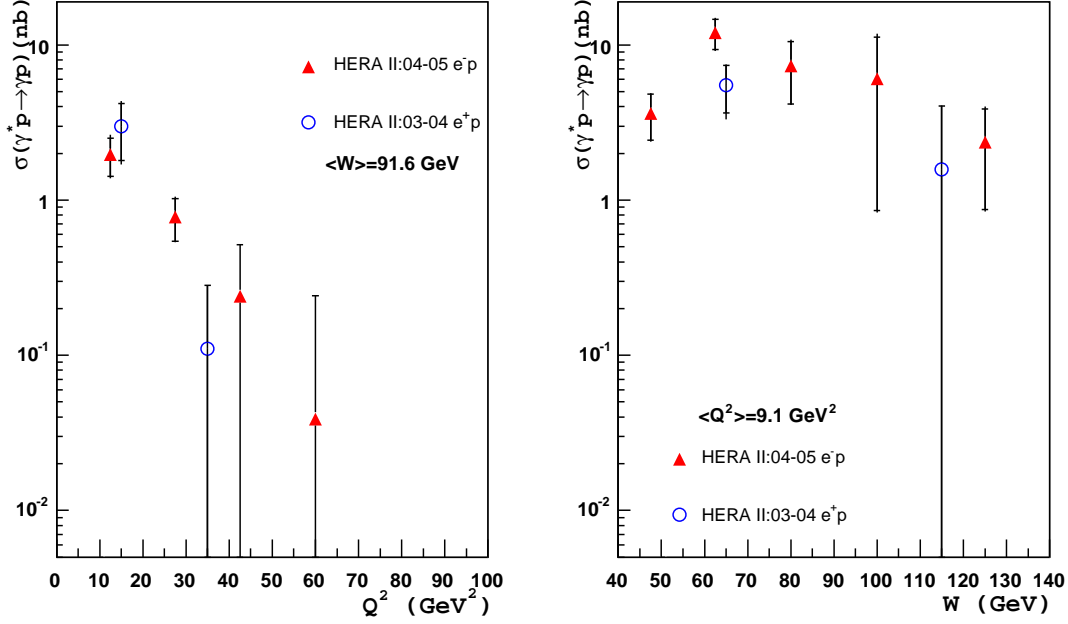
**Figure C.3:** Measured $\gamma^\star p$ DVCS cross sections as a function of $Q^2$ (right) for $< W >= 91.6$ GeV and as a function of $W$ (left) for $< Q^2 >= 9.1$ GeV$^2$. The cross sections have been calculated separately for the two data set used in the analysis. The inner and outer error bars represent the statistical and total uncertainties, respectively. The first $Q^2$ data point for $e^+p$ is displaced horizontally for an easy visualization.

| $e^-p$ | | | $e^+p$ | | |
|---|---|---|---|---|---|
| $Q^2$ bin (GeV$^2$) | $Q_0^2$ (GeV$^2$) | $\sigma^{\gamma^\star p}$(nb) | $Q^2$ bin (GeV$^2$) | $Q_0^2$ (GeV$^2$) | $\sigma^{\gamma^\star p}$(nb) |
| 5 - 20 | 12.5 | $1.96 \pm 0.54^{+0.40}_{-0.22}$ | 5 - 20 | 12.5 | $3.0 \pm 1.2^{+0.6}_{-0.5}$ |
| 20 - 35 | 27.5 | $0.78 \pm 0.24^{+0.13}_{-0.06}$ | 20 - 50 | 35 | $0.11 \pm 0.17^{+0.11}_{-0.06}$ |
| 35 - 50 | 42.5 | $0.24 \pm 0.27^{+0.06}_{-0.02}$ | 50 - 100 | - | - |
| 50 - 70 | 60 | $0.04 \pm 0.20^{+0.01}_{-0.01}$ | | | |
| 70 - 100 | - | - | | | |

**Table C.3:** Values of the $\gamma^\star p$ cross sections for the DVCS process as a function of $Q^2$. Values are evaluated at the center of each bin, $Q_0^2$, and for $< W >= 91.6$ GeV. Left (right) table corresponds to the $e^-p$ ($e^+p$ ) data.

cross section with the data collected in 96-00 (17 pb$^{-1}$ of $e^-p$ and 95 pb$^{-1}$ of $e^+p$ ). These measured cross sections were quoted for $< Q^2 >= 9.6$ GeV$^2$, $< W >= 89$ GeV and the slope $b$ of the $t$-dependence set to 4.9 GeV$^{-2}$. H1 [2] measurements have been performed in the kinematic range $2 < Q^2 < 80$ GeV$^2$,

| $e^-p$ | | |
|---|---|---|
| $W$ bin (GeV ) | $W_0$ (GeV ) | $\sigma^{\gamma^\star p}$(nb) |
| 40 - 55 | 47.5 | $3.63 \pm 1.20^{+0.52}_{-0.31}$ |
| 55 - 70 | 62.5 | $11.95 \pm 2.62^{+1.26}_{-0.97}$ |
| 70 - 90 | 80 | $7.34 \pm 3.20^{+1.20}_{-0.68}$ |
| 90 - 110 | 100 | $6.06 \pm 5.21^{+2.12}_{-0.60}$ |
| 110 - 140 | 125 | $2.36 \pm 1.50^{+1.31}_{-0.24}$ |

| $e^+p$ | | |
|---|---|---|
| $W$ bin (GeV ) | $W_0$ (GeV ) | $\sigma^{\gamma^\star p}$(nb) |
| 40 - 90 | 65 | $5.52 \pm 1.87^{+0.61}_{-1.15}$ |
| 90 - 140 | 115 | $1.58 \pm 2.45^{+0.43}_{-0.31}$ |

**Table C.4:** Values of the $\gamma^\star p$ cross sections for the DVCS process as a function of $W$. Values are evaluated at the center of each bin, $W_0$, and for $< Q^2 >= 9.1$ GeV$^2$. Left (right) table corresponds to the $e^-p$ ($e^+p$ ) data.

$30 < W < 140$ GeV and $|t| < 1$ GeV$^2$ and the values are quoted for $< Q^2 >=$ 8 GeV$^2$, $< W >= 82$ GeV and $b = 6$ GeV$^{-2}$. These two cross sections measurements were extrapolated to the values used in this analysis in order to compare the results. The comparison is shown in figure C.4.
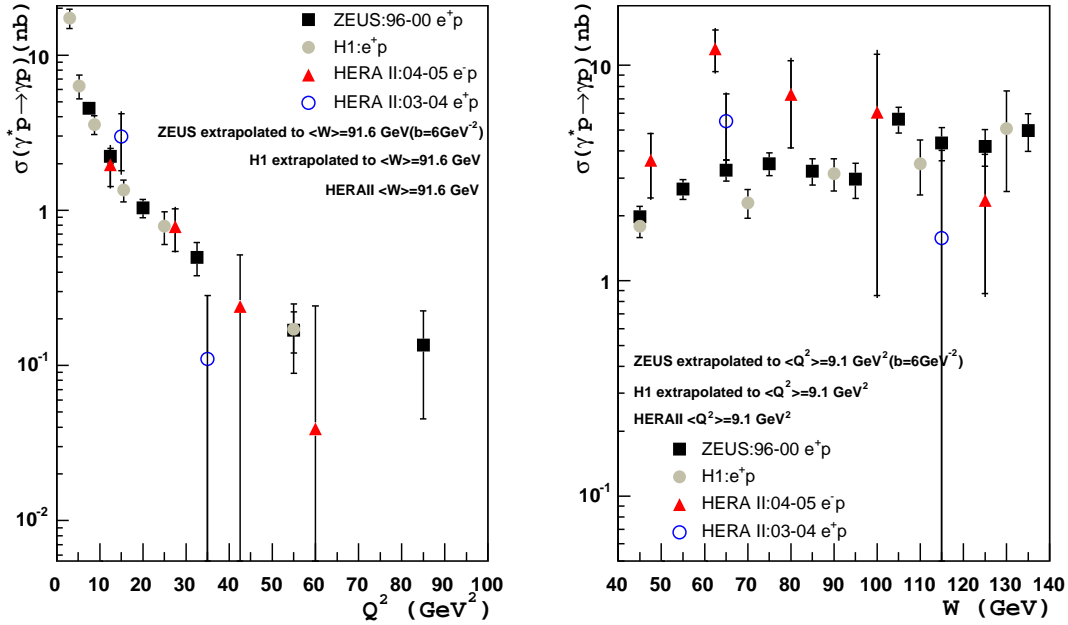


**Figure C.4:** The $\gamma^\star p$ DVCS cross sections measured in this analysis (labeled as HERA II) compared with the previous results from ZEUS [1] and H1 [2] which have been extrapolated to the values obtained in this analysis. The first $Q^2$ data point for HERA II $e^+p$ is displaced horizontally for an easy visualization. Only statistical errors are displayed for the H1 and previous ZEUS data.

As one would expect, a clear disagreement between the measurements of this thesis and the previous results is seen in the region of low $W$, $W < 90$ GeV, since this area correspond to the problematic, one as described in the previous chapter. For the $Q^2$ dependence, the results, within the large uncertainties, are in fairly agreement with the previous measurements.

## C.4   Systematic uncertainties

The systematics uncertainties on the DVCS cross section measurements were calculated varying the relevant measured quantities as well as elements followed in the analysis procedure and recalculated again the cross section. The following systematics have been take into account:

- The electromagnetic energy scale in MC was varied by $\pm 2\%$ for BCAL candidates and by $\pm 21\%$ for the RCAL candidates. The largest variation goes until $+18\%$ for the high $W$ bins.

- The cut in the momentum of the track was varied by $\pm 0.1$ GeV in data and MC resulting in an average change of the cross section of $\sim 4\%$ in $W$ and $Q^2$ .

- The position of the candidates found in the RCAL was changed by $\pm 5$ mm. Variations up to $\sim 7\%$ are found in the high-W bins.

- The parameter $b$ of GenDVCS was changed to 7 GeV$^{-2}$ (up to $+3\%$) and to 5 GeV$^{-2}$ (up to $-5\%$).

- The normalization of the total (elastic+inelastic) contribution of GRAPE was varied according with the values obtained for the high-W $\gamma$-sample (see 6.2.3).

- The fraction of the inelastic background subtracted was changed according with its uncertainty (see 6.3.1). This change results in overall normalization uncertainty of $(+4\%, -5\%)$.

The total systematic uncertainties were determined by adding in quadrature the above individual contributions. The dominant source arises from the uncertainty in the normalization of the BH contribution. In addition, an overall normalization uncertainty is expected due to the error in the luminosity measurements $(e^+ p : \pm 4.5\%, e^- p : \pm 2.7\%)$.

## C.5   Comparison with models

In figure C.5 the measured cross sections are compared with theoretical predictions. Two models have been considered: the GPD-based model of Frankfurt, Freund and Strickman and the color-dipole approach of Donnachie and Dosch (DD) (see 1.5.2).
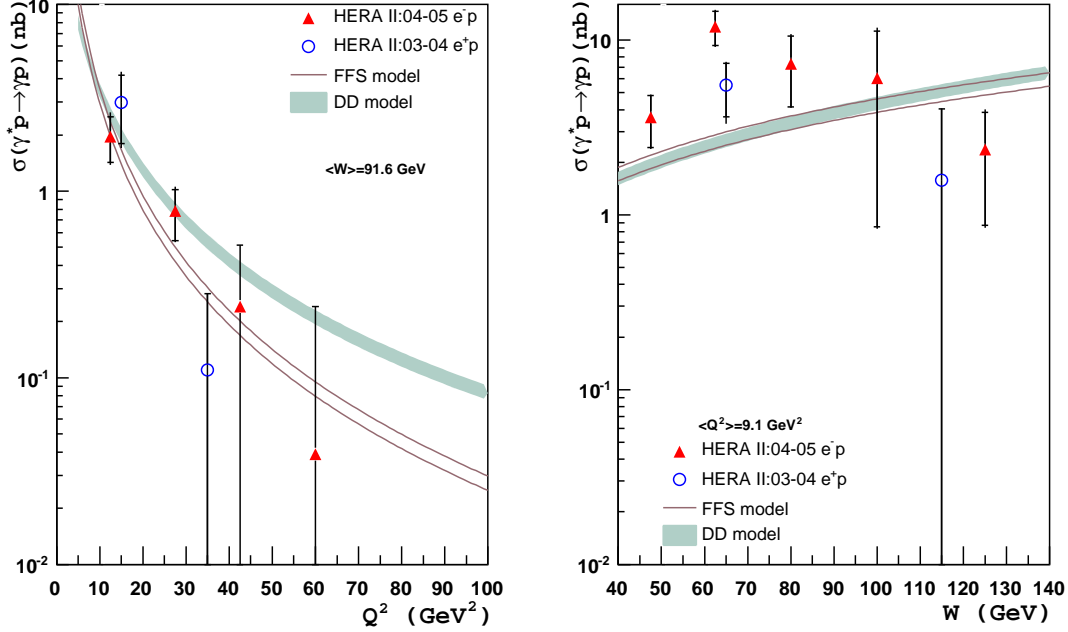


**Figure C.5:**   The measurements of $\gamma^\star p$ DVCS cross sections in the kinematic range 40 GeV < W < 140 GeV, 5 GeV$^2$ < Q$^2$ < 100 GeV$^2$ and $|t|$ < 1 GeV$^2$ in comparison with the theoretical predictions of the FFS GPD-based model [40] and the CDM of Donanchie and Dosch (DD) [45]. The band associated with each of the predictions correspond to an uncertainty on $b$-slope measured by H1 [2]. The first $Q^2$ data point for HERA II $e^+p$ is displaced horizontally for an easy visualization.

The absence predictions for the slope $b$ of the $t$-dependence leave an overall normalization uncertainty which have been constrained with the recent measurements of this dependence by H1 [2] , giving $b = 6.02 \pm 0.35 \pm 0.39$ GeV$^{-2}$. The error bands associated to the predictions, which are shown in figure C.5, correspond to the uncertainty on this measurement.

# Bibliography

[1] ZEUS Collaboration, S. Chekanov *et al.*, Phys. Lett. B **573**, 46 (2003) [arXiv:hep-ex/0305028].

[2] H1 Collaboration, A. Aktas *et al.*, Eur. Phys. J. C **44**, 1 (2005) [arXiv:hep-ex/0505061].

[3] CLAS Collaboration, S. Stepanyan *et al.*, Phys. Rev. Lett. **87**, 182002 (2001) [arXiv:hep-ex/0107043].

[4] HERMES Collaboration, F. Ellinghaus, R. Shanidze and J. Volmer, AIP Conf. Proc. **675**, 303 (2003) [arXiv:hep-ex/0212019].

[5] F. Hanzel and A.D. Martin, *Quarks and Leptons: An Introductory Course in Modern Particles Physics.* John Wiley & Sons,Inc.,1984;
D. Griffiths, *Introductions to elementary par.* John Wiley & Sons,Inc.,1987.

[6] S. L. Glashow, Nucl. Phys. **22**, 579 (1961);
S. Weinberg, Phys. Rev. Lett **19**, 1264 (1967);
A. Salam, *Elementary Particle Physics*, Nobel Symp. N.8, Ed. N. Svartholm, Almquist & Wiksells, Stockholm (1968).

[7] J. D. Bjorken, Phys. Rev. **163**, 1767 (1967).

[8] E. D. Bloom *et al.*, Phys. Rev. Lett **23**, 930 (1969);
M. Breidenbach *et al.*, Phys. Rev. Lett **23**, 935 (1969).

[9] J. C. Collins, D. E. Soper and G. Sterman, Nucl. Phys. B **261**, 104 (1985).

[10] G. Altarelli and G. Parisi, Nucl. Phys. B **126**, 298 (1977);
V. N. Gribov and L. N. Lipatov, Sov. J. Nucl. Phys. **15**, 438 (1972).

[11] I. I. Balitsky and L. N. Lipatov, Sov. J. Nucl. Phys. **28**, 822 (1978);
E. A. Kuraev, L. N. Lipatov and V. S. Fadin, Sov. Phys. JETP **44**, 443 (1976).

[12] M. Ciafaloni, Nucl. Phys. B **296**, 49 (1988);
S. Catani, F. Fiorani and G. Marchesini, Nucl. Phys. B **336**, 18 (1990).

[13] A. Courau and P. Kessler, Phys. Rev. D **46**, 117 (1992).

[14] P. D. B. Collins, *An Inroduction to Regge Theory and High-Energy Physics.*
Cambrigde University Press, Cambrigde, 1977.

[15] V. N. Gribov, Sov. Phys. JETP **14**, 478 (1962).

[16] ZEUS Collaboration, M. Derrick *et al.*, Phys. Lett. B **315**, 481 (1993);
H1 Collaboration, T. Ahmed *et al.*, Nucl. Phys. B **429**, 477 (1994).

[17] G. Ingelman and P. E. Schlein, Phys. Lett. B **152**, 256 (1985).

[18] J. C. Collins, Phys. Rev. D **57**, 3051 (1998) [Erratum-ibid. D **61**, 019902 (2000)] [arXiv:hep-ph/9709499].

[19] A. Berera and D. E. Soper,Phys. Rev. D **53**, 6162 (1996) [arXiv:hep-ph/9509239];
CDF Collaboration, A. A. Affolder *et al.*, Phys. Rev. Lett. **84**, 5043 (2000).

[20] H1 Collaboration. Abstract 6-0175, Internacional Conference on High Energy Physics, ICHEP04, Beijing, August 16, 2004.

[21] Plots available on **http://www-zeus.desy.de/publications.php3**

[22] K. Goeke, M. V. Polyakov and M. Vanderhaeghen, Prog. Part. Nucl. Phys. **47**, 401 (2001) [arXiv:hep-ph/0106012];
M. Diehl, Phys. Rept. **388**, 41 (2003) [arXiv:hep-ph/0307382];
A. V. Belitsky and A. V. Radyushkin, Phys. Rept. **418**, 1 (2005) [arXiv:hep-ph/0504030].

[23] D. Mueller, D. Robaschik, B. Geyer, F. M. Dittes and J. Horejsi, Fortsch. Phys. **42**, 101 (1994) [arXiv:hep-ph/9812448].

[24] A. V. Radyushkin, Phys. Rev. D **56**, 5524 (1997) [arXiv:hep-ph/9704207].

[25] X. D. Ji, Phys. Rev. D **55**, 7114 (1997) [arXiv:hep-ph/9609381].

[26] J. Blumlein, B. Geyer and D. Robaschik, Nucl. Phys. B **560**, 283 (1999) [arXiv:hep-ph/9903520].

[27] A. V. Belitsky and D. Mueller, Nucl. Phys. B **537**, 397 (1999) [arXiv:hep-ph/9804379];
A. V. Belitsky, A. Freund and D. Mueller, Nucl. Phys. B **574**, 347 (2000) [arXiv:hep-ph/9912379];
A. V. Belitsky and D. Mueller, Phys. Lett. B **486**, 369 (2000) [arXiv:hep-ph/0005028].

[28] HERMES Collaboration, C. Hadjidakis, D. Hasch and E. Thomas, Int. J. Mod. Phys. A **20**, 593 (2005) [arXiv:hep-ex/0405078].

[29] X. D. Ji, Phys. Rev. Lett. **78**, 610 (1997) [arXiv:hep-ph/9603249].

[30] E. R. Berger, M. Diehl and B. Pire, Eur. Phys. J. C **23**, 675 (2002) [arXiv:hep-ph/0110062].

[31] P. Amore, C. Coriano and M. Guzzi,JHEP **0502**, 038 (2005) [arXiv:hep-ph/0404121];
A. Psaker, [arXiv:hep-ph/0412321].

[32] J. C. Collins, L. Frankfurt and M. Strikman, Phys. Rev. D **56**, 2982 (1997) [arXiv:hep-ph/9611433].

[33] A. V. Belitsky and D. Mueller, Phys. Lett. B **417**, 129 (1998) [arXiv:hep-ph/9709379].

[34] X. D. Ji and J. Osborne, Phys. Rev. D **58**, 094018 (1998) [arXiv:hep-ph/9801260].

[35] L. Mankiewicz, G. Piller, E. Stein, M. Vanttinen and T. Weigl, Phys. Lett. B **425**, 186 (1998) [arXiv:hep-ph/9712251].

[36] R. L. Jaffe,[arXiv:hep-ph/9602236].

[37] I. V. Anikin, B. Pire and O. V. Teryaev, Phys. Rev. D **62**, 071501 (2000) [arXiv:hep-ph/0003203].

[38] A. V. Radyushkin and C. Weiss, Phys. Rev. D **63**, 114012 (2001) [arXiv:hep-ph/0010296].

[39] A. V. Belitsky, D. Mueller and A. Kirchner, Nucl. Phys. B **629**, 323 (2002) [arXiv:hep-ph/0112108].

[40] L. L. Frankfurt, A. Freund and M. Strikman, Phys. Rev. D **58**, 114001 (1998) [Erratum-ibid. D **59**, 119901 (1999)] [arXiv:hep-ph/9710356]

[41] J. D. Bjorken and J. B. Kogut, Phys. Rev. D **8**, 1341 (1973).

[42] A. Freund, M. McDermott and M. Strikman, Phys. Rev. D **67**, 036001 (2003) [arXiv:hep-ph/0208160].

[43] A. Freund and M. McDermott, Eur. Phys. J. C **23**, 651 (2002) [arXiv:hep-ph/0111472].

[44] N. N. Nikolaev and B. G. Zakharov, Z. Phys. C **49**, 607 (1991),
N. Nikolaev and B. G. Zakharov, Z. Phys. C **53**, 331 (1992),
A. H. Mueller, Nucl. Phys. B **415**, 373 (1994),
A. H. Mueller and B. Patel, Nucl. Phys. B **425**, 471 (1994) [arXiv:hep-ph/9403256].

[45] A. Donnachie and H. G. Dosch, Phys. Lett. B **502**, 74 (2001) [arXiv:hep-ph/0010227].

[46] J. R. Forshaw, G. Kerley and G. Shaw, Phys. Rev. D **60**, 074012 (1999) [arXiv:hep-ph/9903341],

[47] M. McDermott, R. Sandapen and G. Shaw, Eur. Phys. J. C **22**, 655 (2002) [arXiv:hep-ph/0107224].

[48] H. G. Dosch, T. Gousset, G. Kulzinger and H. J. Pirner, Phys. Rev. D **55**, 2602 (1997) [arXiv:hep-ph/9608203].

[49] M. McDermott, L. Frankfurt, V. Guzey and M. Strikman, Eur. Phys. J. C **16**, 641 (2000) [arXiv:hep-ph/9912547].

[50] L. Favart and M. V. T. Machado, Eur. Phys. J. C **29**, 365 (2003) [arXiv:hep-ph/0302079],
L. Favart and M. V. T. Machado, Eur. Phys. J. C **34**, 429 (2004) [arXiv:hep-ph/0402018].

[51] K. Golec-Biernat and M. Wusthoff, Phys. Rev. D **59**, 014017 (1999) [arXiv:hep-ph/9807513].

[52] A. V. Belitsky, D. Mueller, L. Niedermeier and A. Schafer, Nucl. Phys. B **593**, 289 (2001) [arXiv:hep-ph/0004059].

[53] ZEUS Collaboration, S. Chekanov *et al.*, Eur. Phys. J. C **24**, 345 (2002) [arXiv:hep-ex/0201043].

[54] L. Favart, Eur. Phys. J. C **33**, S509 (2004) [arXiv:hep-ex/0312013].

[55] HERMES Collaboration, A. Airapetian *et al.*, Phys. Rev. Lett. **87**, 182001 (2001) [arXiv:hep-ex/0106068].

[56] HERMES Collaboration, [arXiv:hep-ex/0605108].

[57] A. V. Radyushkin, Phys. Lett. B **380**, 417 (1996) [arXiv:hep-ph/9604317]; M. V. Polyakov and C. Weiss, Phys. Rev. D **60**, 114017 (1999) [arXiv:hep-ph/9902451].

[58] W. D. Nowak, [arXiv:hep-ex/0503010].

[59] *HERA: A Proposal for a large electron-proton colliding beam facility at DESY*, DESY-HERA-81/10, Hamburg (1981).

[60] *The HERA Luminosity Upgrade*, DESY-HERA-98/05, Ed. U. Schneekloth (1998).

[61] U. Klein, **http://www-zeus.desy.de/physics/lumi/**.

[62] A. A. Sokolov and I. M. Ternov, Sov. Phys. Dokl. **8**, 1203 (1964).

[63] D. P. Barber *et al.*, Nucl. Instr. and Meth. **A329**, 77 (1993).

[64] M. Beckmann *et al.*, Nucl. Instr. and Meth. **A479**, 334 (2002).

[65] ZEUS Collaboration, S. Chekanov *et al.*, Phys. Lett. B **637**, 210 (2006) [arXiv:hep-ex/0602026].

[66] ZEUS Collaboration, *The ZEUS detector, Status Report 1993*; U. Holm ed. (1993).

[67] A. Andresen *et al.* (ZEUS calorimeter group), Nucl. Instr. and Meth. **A 309**, 101 (1991).

[68] M. Derrick *et al.*, Nucl. Instr. and Meth. **A309**, 77 (1991).

[69] A. Caldwell *et al.*, Nucl. Instr. and Meth. **A321**, 356 (1992).

[70] A. Bernstein *et al.*, Nucl. Instr. and Meth. **A336**, 23 (1993).

[71] A. Bamberger *et al.*, Nucl. Instr. and Meth. **A401**, 63-80 (1997).

[72] A. Dwurazny *et al.*, Nucl. Instr. and Meth. **A277**, 176 (1989).

[73] B. Foster *et al.*, Nucl. Instr. and Meth. **A338**, 254 (1994).

[74] R. Hall-Wilton *et al.*, Internal ZEUS-Note 99-024 (1999).

[75] E. Maddox, *Study of heavy quark production at HERA using the ZEUS microvertex detector*, Ph.D thesis, NIKEF (2004).

[76] ZEUS Collaboration, *A Microvertex Detector for ZEUS*, Tech. Report DESY-PRC 97/01 (1997)

[77] A. Garfagnini, Nucl. Instr. and Meth. **A435**, 34 (1999);
C. Coldewey, Nucl. Instr. and Meth. **A453**, 149 (2000);
E. N. Koffeman, Nucl. Instr. and Meth. **A453**, 89 (2000);
U. Koetz, Nucl. Instr. and Meth. **A461**, 210 (2001);
E. N. Koffeman, Nucl. Instr. and Meth. **A473**, 26 (2001);
V. Chiochia, Nucl. Instr. and Meth. **A501**, 60 (2003);
D. Dannheim *et al.*, Nucl. Instr. and Meth. **A505**, 663 (2003).

[78] J. Andruszkow *et al.*, Acta Phys. Polon.**B32**, 2025 (2001)

[79] M. Helbich *et al.*, Internal ZEUS-Note 06-002 (2006).

[80] W. H. Smith, K. Tokushuku and L. Wiggers. *Proc. Computing in High-Energy Physics(CHEP), Annency, France, 1992*, C. Verkeck and W. Wojcik(eds.), p.222.CERN, Geneva, Switzerland (1992). Also in pre-print DESY-92-150B.

[81] R. Brun *et al.*, CERN DD/EE/84-1 (1987).

[82] P. R. B. Saull, *A Monte Carlo Generator for Deeply Virtual Compton Scattering*, available on **http://www-zeus.desy.de/physics/diff/pub/MC**, (1999).

[83] H. Abramowicz and A. Levy, [arXiv:hep-ph/9712415].

[84] H. Spierberger, *HERACLES: An Event Generator for ep Interactions at HERA Including Radiative Processes*, available on **http://www.desy.de/~hspiesb/heracles.html**, (1996).

[85] T. Abe, Comput. Phys. Commun. **136**, 126 (2001) [arXiv:hep-ph/0012029].

[86] F. W. Brasse *et al.*, Nucl. Phys. B **110**, 413 (1976).

[87] A. Mucke *et al.* Comput. Phys. Commun. **124**, 290 (2000) [arXiv:astro-ph/9903478].

[88] H. Plothow-Besch, Comput. Phys. Commun. **75**, 396 (1993).

[89] T. Sjostrand, Comput. Phys. Commun. **82**, 74 (1994);
T. Sjostrand, L. Lonnblad and S. Mrenna, [arXiv:hep-ph/0108264].

[90] T. Abe, *Measurement of Exclusive J//psi electroproduction in High-Energy ep Collisions at HERA*, Ph.D thesis, KEK Report 2001-13;
K. Muchorowski, *Analysis of exclusive $\rho^0$ production in deep inelastic ep scattering at 300 GeV center-of-mass energy*, Ph.D thesis, Warsaw University, 1998.

[91] K. Schilling and G. Wolf, in inelastic lepton scattering," Nucl. Phys. B **61**, 381 (1973).

[92] J. Repond, Internal ZEUS-Note 96-133 (1996).

[93] G. F. Hartner *et al.*, Internal ZEUS-Note 97-064 (1997); /newlineG. F. Hartner, Internal ZEUS-Note 98-058 (1998).

[94] K. Nagano, *Minimum Bias Vertex Measurement* (unpublished), ZEUS Collaboration meeting, Hamburg (Germany), 4 March 2004.

[95] R. Sinkus, *Measurement of the Proton Structure Function $F_2$ from the 1994 HERA Data using a Neural Network for the Identification of the Scattered Lepton* Ph.D thesis, Hamburg University (1994),
H. Abramowicz, A. Caldwell and R. Sinkus, Nucl. Instrum. Meth. A **365**, 508 (1995) [arXiv:hep-ex/9505004],
R. Sinkus and T. Voss, Nucl. Instrum. Meth. A **391**, 360 (1997).

[96] A. Lopez and S. Schlenstedt, Internal ZEUS-Note 99-077 (1999).

[97] C. Catteral, *Mozart Report* (unpublished), ZEUS Collaboration meeting, Padova (Italy), 18 October 2004.

[98] U. Klein, *Methods for the RCAL energy correction determination* (unpublished), February 2005.

[99] A.P. Rinaldi and A. Brunni, *A study of electron energy correction in DIS events with the ZEUS detector at HERA II* (unpublished), ZEUS Collaboration meeting, Amsterdam (Holland), 8 October 2005.

[100] S. Bentvelsen, J. Engelen and P. Kooijman, HERA Workshop 1991, Vol.1, 23 (1991).

[101] F. Jaquet and A. Blondel. *Proc. of the study of an ep facility for Europe*, ed. U. Amaldi, DESY 79-48, 393 (1979).

[102] T. Haas and U. Kötz. Private communication.

[103] ZEUS Collaboration, M. Derrick *et al.*, Z. Phys. C **73**, 73 (1996) [arXiv:hep-ex/9608010].

[104] I. Grabowska-Bold,*Measurement of Deeply Virtual Compton Scattering Using the ZEUS Detector at HERA*, Ph.D thesis, University of Science and Technology, Cracow, 2004.

[105] ZEUS Collaboration, M. Derrick *et al.*, Phys. Lett. B **377**, 259 (1996) [arXiv:hep-ex/9601009];
ZEUS Collaboration, M. Derrick *et al.*, Phys. Lett. B **380**, 220 (1996) arXiv:hep-ex/9604008].

[106] ZEUS Collaboration, S. Chekanov *et al.*, Eur. Phys. J. C **24**, 345 (2002) [arXiv:hep-ex/0201043].

[107] *The ZEUS Forward Plug Calorimeter with Lead-Scintillator Plates and WLS Fiber Readout*, DESY Report 99-194 (1999).

[108] Alexander Proskuryakov. Private communication.

[109] Joanna Hamiltom McKenzie, *Prompt Photons in Photoproduction Using the ZEUS Detector at HERA*, Ph.D thesis, University of Glasgow, 2005.

[110] C. Ewerz, [arXiv:hep-ph/0511196].

[111] K. Nagano. Private communication.

[112] J. Grebenyuk. Private communication.

[113] H. Spiesberger, *HERACLES and DJANGOH: Event Generation for ep Interactions at HERA Including Radiative Processes*, available on **http://www.desy.de/~hspiesb/djangoh.html**, 1998.

[114] H. Jung, Comput. Phys. Commun. **86**, 147 (1995).

[115] J. Breitweg *et al.* [ZEUS Collaboration], Eur. Phys. J. C **6**, 603 (1999) [arXiv:hep-ex/9808020].

# List of Figures

# List of Tables

# Acknowledgements

I would like to thank Prof. Peter Schleper for his support during the last period of my work. Thanks also to the referees of my thesis and defense Prof. Robert Klanner and Prof. Caren Hagner.

I owe a special thank to Wolfram Zeuner who trust on me when I first arrived at DESY and gave me the opportunity to work on my PhD within the ZEUS Collaboration. Thanks also to my supervisor Uta Klein for all her guidance and support during the last years.

It was great experience to work with the Trigger Group. I learned a lot working with Yuji Yamazaki, Nicola Coppola and John Loizides.

I thank to all the coordinators of the Diffractive group Alessia Bruni, Kerstin Borras, Jo Cole, Marpa Ruspa, Michele Arneodo, Mara Soares and Aharon Levy for all the discussion about my work. Thanks specially to Marta and Michele for the invaluable help and encouragement. Thanks also Marta for reading my thesis.

This work would has not been possible without the great knowledge of many people in ZEUS. Thanks to Krzysztof Wrona, Alessandro Polini, Alex Tapper, Heuijim Lim, Enrico Tassi, Marcella Capua and Stefan Schlenstedt. Thanks to James Ferrando for his help with the manuscript of the thesis and with the analysis.

Many thanks to the Hamburg-students, during these years we have shared lunch, coffee, tee, day and night-time fun, stupid and intelligent questions....Thanks to Chi-Nhan Nguyen, Volker Adler, Liz Nuncio, Julia Grebenyuk, Alessio Bonato, Ingo Bloch, Benjamin Kahle, Oliver Gutsche, Damir Lelas and Dominick Danmhein and Amita Raval, I hope to continue arguing with her for many years ;).

Thanks also to other DESY and non-DESY people that have made my life in Hamburg much easier: Anabel Ortega, Matilde Balbastro, Jolie, Jenny Ferrando, Tobias Toll, Lluis Marti, Wakiko, Matt Forrest, Silvia Migloranzi, Manolo Zambrana, Marcos Jimenez, my lovely neighbors and many others.

Finally, everything what I have achieved until now would have not been possible without my family. Thanks to my parents for being always there. Thanks to my brother, Ru, my particular "man", you cannot imagine how proud I am of you. Thanks to my grandma for calling me almost every night for the last 4 years. This is going to be the last line of my thesis and is dedicated to Álvaro, you always told me that I will see myself writing this last line, I love you.